UNIVERSITY OF SOUTHAMPTON

FACULTY OF PHYSICAL AND APPLIED SCIENCES

Optoelectronics Research Centre

Laser processing of amorphous silicon for photonic applications

by

Gregorio Martinez-Jimenez

Thesis for the degree of Doctor of Philosophy

October 2017

UNIVERSITY OF SOUTHAMPTON

ABSTRACT

FACULTY OF PHYSICAL AND APPLIED SCIENCES
Optoelectronics Research Centre

Doctor of Philosophy

LASER PROCESSING OF AMORPHOUS SILICON FOR PHOTONIC APPLICATIONS

by Gregorio Martinez-Jimenez

The topic of the research that is presented in this thesis is the development of a laser-based method for the crystallization of amorphous silicon (a-Si) films, deposited on various planar substrates for the fabrication of photonic structures. The emphasis is on lithium niobate which has many useful properties for photonic applications. This research stems from experimental evidence suggesting that it is possible to produce large Si crystallites by irradiating a-Si with continuous wave laser beams at visible wavelengths. This method has been particularly successful in semiconductor core optical fibres. Here this laser-crystallization method is being extended to planar geometries staring with glass substrates and extending to crystalline lithium niobate. The aim is to produce hybrid optoelectronic devices that will benefit from the properties of the constituents (Si and lithium niobate). These devices will target photonic applications in the area of optical telecommunications and sensing.

Contents

List of Figures

List of Tables

Declaration of Authorship

I, Gregorio Martinez-Jimenez , declare that the thesis entitled *Laser processing of amorphous silicon for photonic applications* and the work presented in the thesis are both my own, and have been generated by me as the result of my own original research. I confirm that:

- this work was done wholly or mainly while in candidature for a research degree at this University;
- where any part of this thesis has previously been submitted for a degree or any other qualification at this University or any other institution, this has been clearly stated;
- where I have consulted the published work of others, this is always clearly attributed;
- where I have quoted from the work of others, the source is always given. With the exception of such quotations, this thesis is entirely my own work;
- I have acknowledged all main sources of help;
- where the thesis is based on work done by myself jointly with others, I have made clear exactly what was done by others and what I have contributed myself;
- none of this work has been published before submission

Signed:.....

Date:.....

Acknowledgements

This research and my entire life as PhD student would not be possible or enjoyable as it was without the help and support of many individuals, it will be impossible to mention all the people that some how cheer me up during the process but have in mind i will remember you all.

I would like to thank mainly:

To my supervisor Dr Sakellaris Mailis, for his entire disposition since the beginning and his tireless help with everything from my personal life to my research, as well to my co-supervisor Dr Anna Peacock for her support and wise advise also to Dr Noel Healy for all his shared knowledge in the lab and in the data process.

To my colleges: Gregoris Zissis, Rob Topley, Yohann Franz, Antoin Runge, whom have became close friends after sharing with me their time and ideas, always there present to help and support. To all the ORC staff at the University of Southampton for the time and instruction in all the equipment i required to do all the work. In the same manner to the Diamond Light Source staff, specially to Dr. Konstantin Ignatyev in beam I18 whom was always kind and helpful, giving me advices and practical suggestions.

To CONACYT for funding me during my PhD. studies. To all my Family and Friends whom guided me and comfort me always during bad days and celebrate with me during the good ones.

And specially to you Alma: En la sombra y en la luz; tú me llamarás auxocromo, el que capta el color. Tu cromóforo, la que da el color. Tú eres todas las combinaciones de números. La vida. Mi deseo es entender la línea, la forma, el movimiento. Tú llenas y yo recibo. Tu palabra recorre todo el espacio y llega a mis células que son mis astros y va a las tuyas que son mi luz.

Thank you everybody, for everything and for so much.

Nomenclature

Si	Silicon
$a-Si$	Amorphous Silicon
$poly-Si$	Polycrystalline Silicon
$c-Si$	Crystal Silicon
SiO_2	Silicon dioxide
LN	Lithium Niobate
Ge	Germanium
CW	continuous wave
$a-Si/SG$	amorphous Silicon deposited on Silica Glass
$a-Si/Sc-Si$	amorphous Silicon deposited on Silica on Silicon
$a-Si/LN$	amorphous Silicon deposited on Lithium Niobate
XRD	X Ray Diffraction
$c-LN$	Crystal Lithium Niobate
CVD	Chemical Vapour Deposition
$HWCVD$	Hot Wire Chemical Vapour Deposition
$PECVD$	Plasma Enhanced Chemical Vapour Deposition
λ	wavelength
RIE	Reactive Ion Etching
$FWHM$	Full Width at Half Maximum
SEM	Scanning Electron Microscope
IR	Infra Red
$CMOS$	Complementary metal oxide semiconductor
$a-LN/c-Si$	Amorphous Lithium Niobate on Crystal Silicon

Chapter 1

Introduction and Background

1.1 Introduction

Today the combination of electronics and photonics is very important for the development of new technologies. Optoelectronic devices are now used regularly in everyday life as biological sensors, chemical sensors, barcodes readers, and telecommunication circuits to name a few. The constant demand for higher performance optoelectronic makes necessary the development of new ways to produce more complex optoelectronic circuits and to fabricate them faster and with a lower cost.

Silicon (Si) is an extremely versatile material with applications ranging from microelectronic devices, solar cells etc [1, 2]. It is also commonly used as the semiconductor platform in electronics for the fabrication of devices such as transistors, printed circuit boards and integrated circuits [3] . In the recent past there has been some interest in using Si for photonics applications. Recently optical fibres with cores made of amorphous Silicon (a-Si) have been developed as a means for low cost substitute to crystalline Si. However the poor optical transmission of a-Si lied to the development of methods for crystallization of the amorphous core, one of this methods is laser induced crystallization [4]. Due to the simplicity of achieving the conditions for efficient crystallization using a continuous wave lasers at visible wavelength, the process was applied here to planar structures.

During this work, the attention will focus on extending and improving the method used by Peacock et all, into making planar Si ridge waveguides

on different substrates such as SiO_2 and Lithium Niobate (LN), in order to develop a new platform for the large scale production of hybrid devices in the case of LN substrates, taking the advantage of the combined properties of the constituent materials.

On the other hand LN is an artificial crystal with many useful physical properties, it has a large pyroelectric, piezoelectric, acusto-optic, nonlinear and electro-optic coefficient and is one of the key materials for the fabrication of photonic circuits. LN has a broad range of applications ranging from acoustic-wave transducers and filters in mobile telephones, to optical modulators and wavelength converters in fibre telecommunication systems, to name just a few. All that make LN an important material in the area of integrated optics.

The objective in this thesis is the research and develop of a new method for the fabrication of hybrid integrated optical circuits using continuous wave (CW) visible laser writing on amorphous silicon deposited on silica (a-Si/G) at low temperature (lower than 500 °C) and on lithium niobate (a-Si/LN). These devices will target photonic applications in the area of optical telecommunications, sensing and will include resonant photonic structures such as whispering gallery mode and ring or disc waveguide resonators, as well as a supporting network of optical waveguide circuitry including signal processing and nonlinear components such as Mach-Zehnder interferometers, couplers, wavelength converters and acousto-optic transducers, all combined on a single substrate. This new method promises to reduce the actual cost and the complicated methods of production of optical circuits by using more affordable initial materials and less production steps compared with the existent processes.

In the next sections of this chapter. I will introduce the key points to follow this research. In the second, third, and forth chapters the experiment methodology and the results of the crystallization process and the waveguide development for a-Si/G as well as a-Si/LN are shown, as well the analytical methods: Raman spectra and X Ray Diffraction (XRD) that provide a qualitative analysis of the crystallization achieved by this process. In the fifth chapter a collection of intermediate experiments and results related with laser crystallization will be presented. Finally in the last chapter the conclusions and the future work on this research will be discussed.

1.2 Key Points

To understand the experiments shown in the next chapters of this thesis, a brief review on the next points will be useful:

- Physical properties of Silicon.
- Physical properties of Lithium Niobate.
- General description of the composite material used in this research (a-Si/Silica, a-Si/LN).
- General description of Analytical Methods (Raman Spectroscopy and X-Ray Diffraction).
- General description of optical waveguides.

1.3 Silicon

Si is a solid at room temperature and with atomic number of 14. It has a greater density in a liquid state than in solid state, similar to how water is more dense than ice. Si is a semiconductor widely used in electronics: devices such as transistors, printed circuit boards and integrated circuits make use of silicon's properties, that is why a great part of modern technology depends on it.

Two of the most common allotropic forms of Silicon are crystal Silicon and amorphous Silicon, a sketch of the structure that they form is shown in Figure 1.1. Polycrystalline silicon (poly-Si) is another common and very used form of Si especially in the photovoltaic and electronics industry. The mainly difference between crystalline silicon and poly-Si is that crystalline silicon is form of one single, continuous and unbroken crystal without grain boundaries, and poly-Si is formed by a number of smaller silicon crystals named crystallites with different sizes varying from a few nanometres to several millimetres and with random orientation.

Crystal Silicon (c-Si) consists of arranged silicon atoms in which the crystal lattice of the entire solid is regularly and continuous. It is the base material for electronic chips used in virtually every electronic device. c-Si

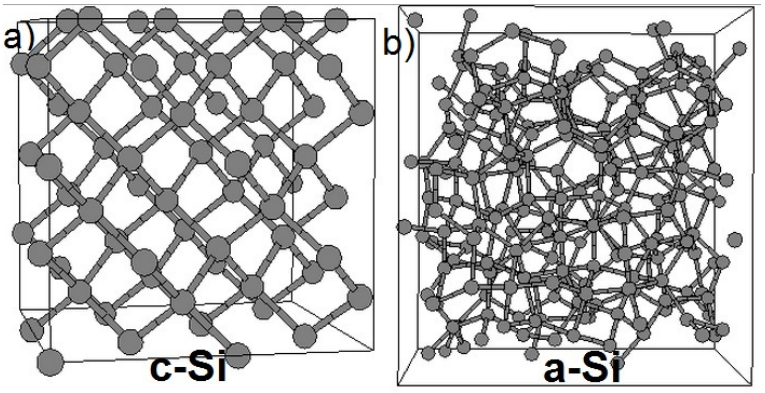

Figure 1.1: Sketch of allotropic forms of Silicon, (a) crystalline Silicon, (b) amorhpous Silicon.

also serves as photovoltaic, light-absorbing material for manufacturing solar cells. More recently it has received interest by several research groups for its potential role in the area of photonics principally for its transparency window ranging from $1100nm$ to $7000nm$ [5], which agreed perfectly with the optical communications band ($1460nm$ to $1675nm$) [6, 7, 8]. Although c-Si has a great potential in photonics, it has some disadvantages. It is expensive to grow, requiring lengthy processes and expensive equipment, as in the case of the Czochralski process. c-Si has high melting and boiling points of 1687 K and 3538 K, respectively [9]. These disadvantages make c-Si a difficult and costly material for integration with other materials and mass production.

Czochralski process

The Czochralski method is a process for growing single crystal silicon ingots for use manly in manufacturing semiconductor devices [10]. The finished crystals are called boules. The boules are later sliced into thin circular wafers, and then diced into silicon pieces from which silicon semiconductor chips are made out of.

The Czochralski method begins with highly pure silicon powder. This pure silicon powder is placed in a large container made of fused quartz to resist high temperatures. The container is placed inside a vacuum chamber and then filled with inert gas, usually argon. This chamber is then heated up to 1500 °C, to melt the silicon. When the silicon is melted, a small seed crystal mounted on the end of a rotating shaft is slowly lowered until it just dips below the surface of the red hot silicon melt. The shaft and the container

with the melted silicon rotates in opposite directions. Now, the rotating rod is drawn upwards very slowly, allowing a roughly cylindrical boule to form.In this process boules of to two metres long and $300mm$ wide can be produced. The electrical characteristics of the silicon are controlled by adding different dopant materials like phosphorus or boron to the silicon while the boule is grown.

As was mentioned the Czochralski process is a costly and difficult method, it has the advantage to produce high quality crystals but makes a bad choice to combine it with other substrates or to deposit thin layers for the manufacturing of photonic devices.

Starting from a less pure material and with a variety of non aggressive process to merge with others could be a more viable option. Amorphous silicon has these properties and make a good precursor material for the developing of optical waveguides.

Amorphous silicon

Amorphous silicon (a-Si) is a non-crystalline structural form of silicon. In crystalline silicon (c-Si) the tetrahedral structure continues over a long range, thus forming a well-ordered crystal lattice, in a-Si this long range order is not present. Rather, the atoms form a continuous random network. That is why a-Si presents poor electronic performance compared to c-Si, although it is much more flexible in its applications. For example, a-Si layers can be made thinner than c-Si, which may produce savings on silicon material cost [11]. Thin films of a-Si can be deposited at low temperatures, about $450°C$ [12] into a variety of substrates [9]. This allows for deposition on temperature sensitive materials such as plastic [13]. Once deposited, a-Si can be doped in a fashion similar to c-Si, to form p-type or n-type layers, and ultimately use it in electronic devices [14].

Another advantage is that a-Si can be deposited over large areas by methods such as sputtering, hot wire chemical vapour deposition (HWCVD) and plasma enhanced chemical vapour deposition (PECVD). PECVD is a process used to deposit thin films from a gas state (vapour) to a solid state on a substrate by electrical discharging. Also, HWCVD was used to deposit a-Si on the substrates. More details of these processes used to deposit a-Si in this research will be covered in the next sections.

The a-Si can be crystallized by different processes after been deposited on to a substrate gaining the excellent electrical properties of c-Si. Crystallization of a-Si has been achieved by femtosecond laser annealing at a wavelength of 800nm [15], also using CW argon laser with ($\lambda = 514.5nm$) [16] and by UV pulsed excimer laser [17].

Since laser crystallization depends of the optical absorption of the material, it is important to know the range of wavelengths where a-Si absorbs. In Figure 1.2 different wavelengths are plotted versus optical absorption, which corresponds to the imaginary part of the refractive index (k). In the graphic on Figure 1.2 is shown that as the wavelength approaches to the ultra violet region the absorption in a-Si increases. In this same plot we could notice the absorption at $488nm$ where a-Si is capable to absorb the radiation. An other useful parameter of a-Si is its refractive index $n = 3.48$ for a wavelength of $1550nm$, which is in the center of the telecommunications band [18].

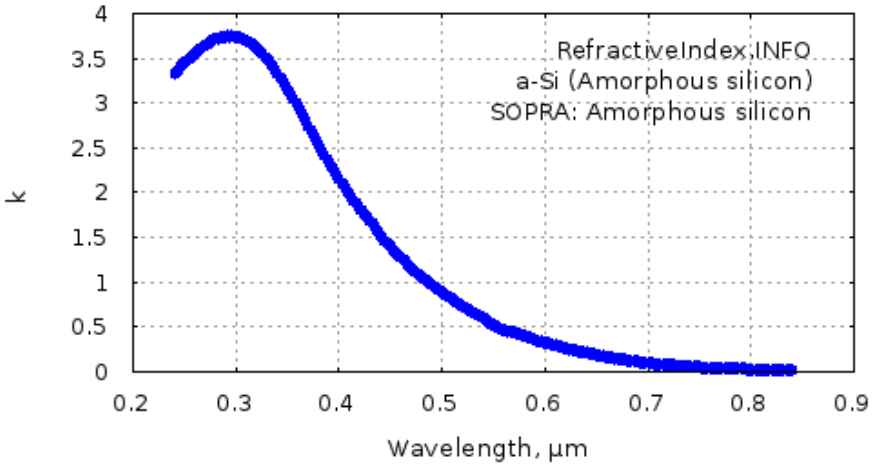

Figure 1.2: absoprtion of a-Si in the visible to UV region.

One of the goals in this research is to investigate a new technique to crystallise a-Si by CW laser writing. As a result, different methods to recognize c-Si from a-Si are needed. The two methods used in this work are Raman spectroscopy and X-Ray diffraction (XRD). Raman Spectroscopy is a spectroscopic technique used to observe vibrational, rotational, and other low-frequency modes in a system. In solid-state physics, spontaneous Raman spectroscopy is used, among other things, to identify materials, measure temperature, and find the degree of crystallization of the sample. XRD is a tool used to identify the atomic and molecular structure of a crystal, in which the atoms cause a beam of incident X-rays to diffract into specific directions.

By measuring the angles and intensities of these diffracted beams the mean positions of the atoms in the crystal can be determined. A more detailed description, along with the results and discussion of these two methods will be show later.

1.4 Lithium Niobate (LN)

Lithium Niobate (LN) is a solid. It has a trigonal crystal system, a representation of this crystal is shown in Figure 1.3. It was first grown artificially in 1928 [19] and its chemical formula is $LiNbO_3$. Its melting point is about $1550K$ [20], which is higher but close to the melting temperature of amorphous silicon. LN is a dielectric material widely used in photonics with numerous properties such as electro optic, piezoelectric, acousto-optic, photorefractive, pyroelectric, photovoltaic, ferroelectric, optical nonlinear [21].

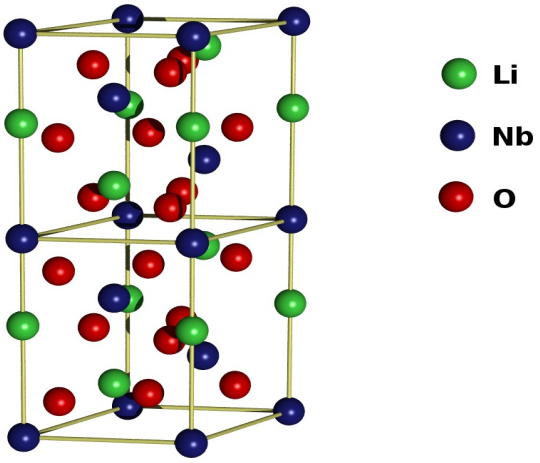

Figure 1.3: Schematic representation of LN crystall unit cell.

LN is a ferroelectric material which has a spontaneous electric polarization along the z-axis. The direction of the polarization can be inverted, for example by the application of an external electric field. Due to this electro-optic effect, a refractive index difference between anti parallel domains can be induced and controlled by the application of an external voltage.

LN is pyroelectric at room temperature. In pyroelectric crystals the change in temperature modifies the positions of the atoms slightly within the crystal structure, such that the electric polarization of the material changes and provokes a change in the index of refraction, this phenomena has been

studied and described in detail within [22]. In Figure 1.4 the temperature dependence of the refractive indices ordinary n_o and extraordinary n_e of LN for a wavelength of $\lambda = 546nm$ is shown. Here it is observed that as the temperature increases, both indices increase and also the birefringence decreases.

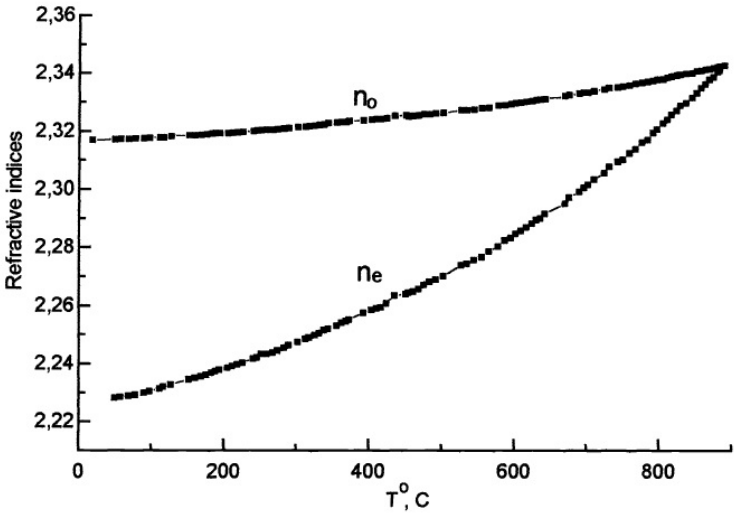

Figure 1.4: Temperature dependence of the ordinary and extraordinary refractive indices of pure LN crystals for a wavelength of $546nm$.

LN has a wide transparency window over the visible part of the spectrum, which makes it a very useful optical material. The transparency region starts in the ultraviolet at $320nm$ and reaches the infra-red (IR) at $6\mu m$. The absorption curve (Figure 1.5) is relatively flat over this wavelength range [23]. For the propose of this research, it should be noted that the absorption of LN at blue-green wavelengths (used here for laser crystallization of a-Si) is low compared to the absorption for the same wavelengths in silicon.

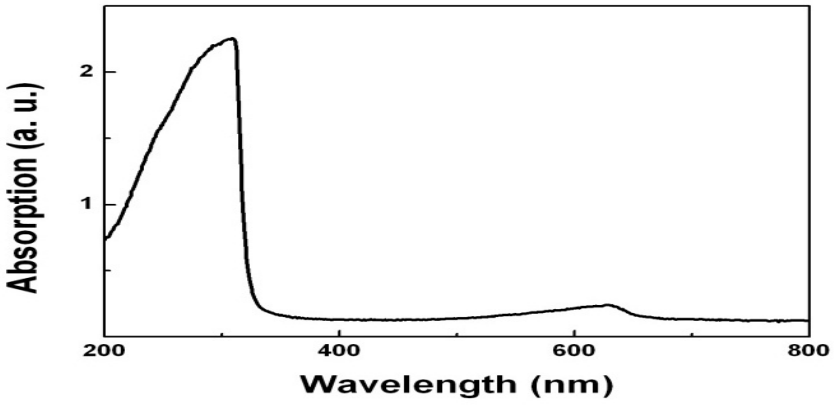

Figure 1.5: Absorption curve of LN taken from [23].

It has been shown that illumination of LN with CW UV lasers at $244nm$ can direct write waveguide structures that can be adjusted by varying parameters such as incident laser power and spot size [24]. In 2002 it was observed that irradiation of LiNbO3 with a UV laser ($\lambda = 244nm, 248nm, 308nm$) had the effect of creating a differential etch rate between illuminated and unilluminated regions when etched in hydroflouric acid [24]. This effect is due to a lasting reversal of the polarization of the crystal induced by the UV irradiation. Local heating caused by UV irradiation also produces optical waveguides in LN [25].

This research would potentially contribute in the branch of silicon photonics by developing a new technique to fabricate silicon waveguides which has the possibility to merge with different substrates that could increase their functions. Then a brief review in silicon photonics will be presented in the next section.

1.5 Introduction to Silicon photonics

Silicon photonics emerged as a viable option to the limitations of actual electronics and as a solution to the needing of faster, better and cheaper global communication systems, detectors, sensors, etc [26]. In a simple explanation silicon photonics is the combination of silicon integrated circuits and semiconductor lasers in which data is transferred among computer chips by optical rays at the IR spectral range [27]. It enables faster data transfer over longer distances with less energy consumption compared to traditional electronics [8].

Consequently, silicon photonics is being actively researched by many electronics manufacturers like IBM and Intel, as well as by academic research groups including the Optoelectronics Research Centre at the University of Southampton [28].

State of the art

Silicon photonic devices can be produced using existing fabrication techniques used in CMOS manufacturing. These well developed techniques could be used to create hybrid devices by merging silicon with other materials

in which their optical and electronic properties are integrated onto a single microchip. For example, combining Si with other materials as LN could add functionality for many different devices [29].

A large library of components for silicon photonics have been manufactured with excellent results: the range of devices fabricated cover from waveguides, couplers, filters, modulators, detectors etc. Recent advances for these structures have been compiled here [5]; a short summary with the must important results will be covered next.

Si waveguides are the most basic devices in photonics, through which optical signals can be transferred from one point to another: the latest reported results have achieve losses in the range of 0.1 using the Cr hardmask process with the smoothest side wall [30] to $0.3dB/cm$ using the low loss etchles technique suggested in [31] both at wavelength of $1550nm$.

Coupling light from optical fibres to silicon waveguides has been solve in different manners, finding the best results using surface grating couplers where the coupling efficiency has been demonstrated to be around 65.6% at $1550nm$ [32, 33].

Optical filters used for wavelength multiplexing and demultiplexing have found the best results in the shape of optical microrings and microdisks cavities due to their potential for high-density integration[34, 35], in these devices light travels through a waveguide in close proximity to a ring, so that the evanescent fields of the optical modes overlap, and the optical energy can transfer to the ring, filtering the desired wavelength by modifying the ring diameter.

Modulators are devices which can vary fundamental characteristics of the input light beam using an external source carrying the information signal that modifies the output propagating either in free space or in an optical waveguide. They can be categorized as amplitude, phase, or polarisation modulators. Modulators can be also classified into two operational categories: electrorefractive and electroabsorptive [36] .

The primary electric field effects that are traditionally useful in semiconductor materials, to cause either electroabsorption or electrorefraction are the Pockels effect, the Kerr effect, and the Franz-Keldysh effect. However, it

has been shown that these effects are weak in pure silicon at the communications wavelengths of 1.3 m and 1.55 m [37]. The most common modulation method used in silicon devices to date is the plasma dispersion effect, in which the concentration of free charges in silicon changes the real and imaginary part of the refractive index [28]. Electrical manipulation of the charge density interacting with the propagating light is achievable through mechanisms such as carrier injection, accumulation or depletion . From these schemes carrier depletion is the fastest silicon modulator reported to date. Demonstrating data transmission at $40Gb/s$ with an extinction ratio of 3 dB [38, 39]. Such devices operate by interaction of the propagating light with the junction region of a pn diode which is operated with a reverse bias.

Combining Si with LN that possess strong second-order nonlinear electro-optical effects, such as Pokels effect, and has a low transmision loss in the telecom band, makes it an excellent candidate to form hybrid devices for modulation applications. Experimentally have been demonstrated that these modulators can operate at $40Gb/s$ and a wide bandwidth of $30GHz$ [40]

Photodetectors are components that convert the received optical signal into electrical signal for further processing. Since Si has a transparency window operating in the IR range, it is not a suitable option for this application, then again hybrid devices have been produced to enlarge the capabilities of Si devices, in this case Germanium (Ge) has been merged into silicon since it exhibits strong absorption at communication wavelenths. Ge also exhibits excellent optoelectronic properties, including high responsivity in near-IR wavelength, high bandwidth, and compatibility with CMOS technology. Ge/Si photodetectors have been produced with good results with bandwidth as high as $42GHz$ and responsivity at $1A/W$ operating at $1550nm$ [41] .

All these results inspire to find better fabrication methods which allow the merging of different materials with silicon, multiplying its capabilities and uses to produce more variety of photonic devices in a faster and affordable manner. The combination of Si with different substrates will benefit from the properties of the constituents (Si and lithium niobate in the case of this research). Different substrates were combined with silicon using various deposition methods; we will review the preparation of these composite systems in the next section.

1.6 Composite system (a-Si on Silica and a-Si on LN)

One of the key attractions of Si is that it benefits from the mature processing technology that has been developed for the microelectronics industry. However, in terms of its optical properties it has several deficiencies mainly associated with the lack of electro-optic and second order nonlinear optical capability. LN on the other hand, complements the deficiencies of silicon since it is a material with excellent electro-optic and non linear properties [42], that has made it widely used in the photonics industry for optical switching and nonlinear wave mixing applications. Combining these very important technological materials could produce composite systems that will benefit from the complimentary properties of the constituents. In this research these two materials were combined by depositing a thin layer of a-Si on silica and LN by PECVD and HWCVD. This methods were chosen because both have a mature to deposited a-Si in different substrates. In both methods the temperature needed is lower than 400°C, making them suitable to deposited a-Si in different substrates.Also both methods yield some of the fastest deposition rates while maintaining good film quality, such as low roughness and defects, as compared with other deposition methods. These two techniques can be collected under the chemical vapour depositions (CVD), in which the film is produced via thermal-chemical reactions. In the case of amorphous silicon, silane is used as the chemical precursor. The deposition process are named by the different kinds of energy used to dissociate silane. For example if the silane is dissociated by plasma we have PECVD, on the other hand, if the thermal activation is produced by a hot filament, then is named HWCVD.

Plasma enhanced chemical vapour deposition (PECVD)

Plasma deposition is often used in semiconductor manufacturing to deposit films conformally (covering sidewalls), and onto wafers containing metal layers or other temperature-sensitive structures [43]. In the PECVD technique, energy is directly imparted to the chemical system by the collision of energetic electrons with the heavy particles of the precursor. In particular, in a plasma produced at low pressures, the free electrons can gain sufficient kinetic energy

to activate processes of excitation, ionization, and dissociation, while maintaining low gas temperature [44]. Since in this process there is need of precursors with hydrogen, the final a-Si deposited often contains some hydrogen [45].

Hot wire chemical vapour deposition (HWCVD)

Another method for the deposition of a-Si treated during this research was HWCVD. This method of deposition is different from PECVD. In this deposition method precursor gases, silane or silane/hydrogen in the case of thin film silicon deposition, are catalytically dissociated at resistively heated tungsten filaments [46]. This deposition method has been used many times for the deposition of a-Si on many different substrates [47] and for many different studies from solar films [48] to optical waveguides [49]. For this deposition method the hydrogen content could be controlled in a better manner than for PECVD. The samples used during this research had the lowest possible hydrogen content in order to not produce other effects during the laser annealing.

Here will be presented a composite system of a-Si thin film deposited on to silica and ferroelectric LN single crystal substrate. The LN crystal substrates used in these experiments were diced out of a congruently melted z-cut wafer with a thickness of $500\mu m$. The composite samples were first produced by deposition of a-Si using PECVD and later by HWCVD deposition as in the case of silica, onto the polar (z) faces of the substrates. Two different thicknesses of the deposited a-Si films were investigated: in both cases (a-Si/G and a-Si/LN) were of order of $200 - 250nm$ and $400 - 450nm$ uniform across the surface of the sample, see Figure 1.6.

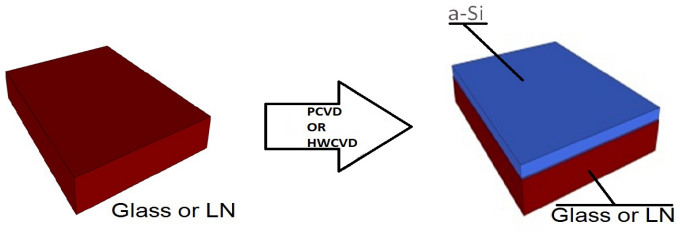

Figure 1.6: PECVD deposition of a-Si on silica and LN

Thin films were laser irradiated to crystallize the irradiated surface of a-Si. Different analytical methods were used to confirm the quality of the crystallization; in the following section the methods will be briefly described.

1.7 Analytical Methods

Raman Spectroscopy Analysis

Raman Spectroscopy is a powerful tool for the investigation of molecular vibrations that can be used for sample identification, as each substance has a unique Raman spectral structure [50]. It relies on inelastic scattering, or Raman scattering from a monochromatic source of light (laser). The samples are illuminated with a laser beam in this case at $532nm$. The electromagnetic radiation from the illuminated spot is collected with a lens and sent through a monochromator. The Rayleigh (elastic) scattering is filtered out while the rest of the collected light is dispersed onto a detector by a grating. We can plot the intensity of this filtered light as a function of its energy difference or wavenumber: this plot is called a Raman Spectrum, and is unique for each individual material. In the graph at Figure 1.7, we present different Raman spectra corresponding to different materials used in this work.

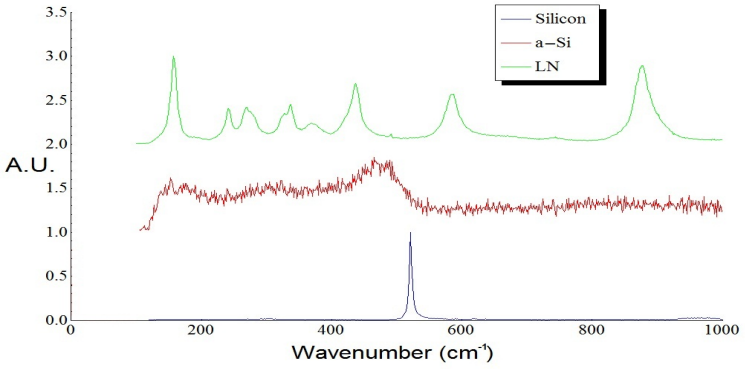

Figure 1.7: Graph of different Raman Spectra (The spectra have been shifted with a baseline for the different materials.), Blue: Cristalline Silicon Reference; Red: Amorphous Silicon (a-Si); Green: Z+ cut of Lithium Niobate Reference.

We can observe that c-Si and LN have well defined peaks at certain positions due to their crystal nature. We can notice c-Si having only one peak meanwhile LN has many. This is because the laser light interacts with more molecular vibrations, resulting in the energy of the laser photons being shifted up or down. The shift in energy gives information about the vibrational modes in the system. Then LN has more vibrational modes in its molecules due to its structure.

In the case of LN different crystal cuts produce a different Raman spectra, for this case as it was mention a Z cut was used , the peaks positions corresponded to those for this cut according to the literature [51].

Besides a-Si has a wider distribution along all the wavenumbers. We would expect a change in this Raman spectra after laser annealing where the broad a-Si will become more like the narrow c-Si peak.

XRD Analysis

X-ray Diffraction (XRD) is used to identify the atomic and molecular structure of a crystal, in which the crystal planes of the material under investigation act as a grating causing a beam of incident X-rays to diffract into specific directions. In Figure 1.8 the schematic of the X-Ray diffraction set up that was used in this research is shown. The X-Ray beam used had spot diameter of $3\mu m$. The beam gets diffracted by passing through the sample and projecting concentric rings into a CCD, these rings are called Debye rings and are associated to the different crystal planes. The diffraction patterns for all the samples will be collected within viewing quadrant using a special camera, as indicated in Figure 1.8.

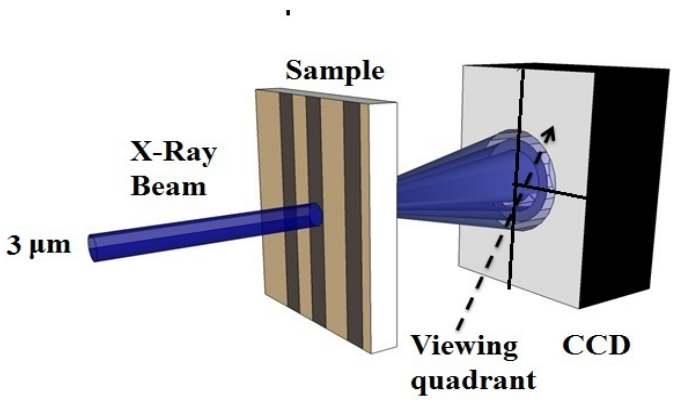

Figure 1.8: X-Ray Diffraction arrangement at I18 beamline (Diamond light source).

By measuring the angles and spacing on the diffracted patterns produced by the samples, the distance between crystal planes can be determined, as well as their chemical bonds and their disorder [52].

A reference sample of silicon powder was introduced to the XRD setup. The diffraction pattern generated from this test sample shows all the possibles crystal planes for silicon [53]. Depending on the Debye ring radius and their different position on the ring, each point along the concentric rings corresponds to an individual crystal. In Figure 1.9 the diffraction pattern of this silicon powder is shown with the crystal planes using the Miller's notation ($\langle hkl \rangle$), associated with each one. In the case of lithium niobate powder the number of rings examined corresponding to crystal planes was 61, as found in [54].

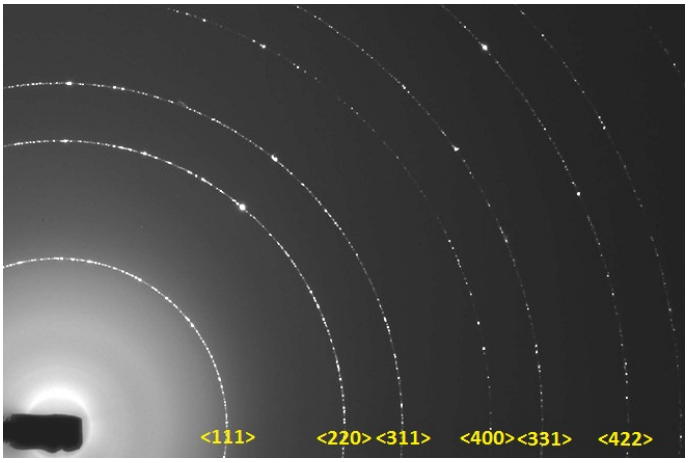

Figure 1.9: Diffraction pattern from silicon powder (reference sample) with crystal planes as $\langle hkl \rangle$ in yellow.

In the case of an individual crystal, just one bright spot in one of the concentric Debye rings will show up, the position of which will depend on the orientation of the crystal and the crystal plane. In the case when there is a shift between the position from any of the reference ring to a particular diffracted spot, this will provide information about deformation by an applied force in the crystal plane. For example; In the case when the spot is at a closer but smaller radius ring compared to one of the reference rings we identify this as tensile strain. On the other hand when the spot is in a ring with a slightly larger radius than the reference we found compressive strain. This difference will be called distance shift. Also, if it is possible to scan the x-ray beam along the sample and observe for how long the spot in the different diffraction patterns keeps in the same position, in this way the size of an individual crystal can be determined.

1.8 Optical Waveguides

Optical waveguides are photonic structures where light is confined and can propagate exclusively on a plane or along a channel. Optical waveguides confine light by total internal reflection, due to the difference in the index of refraction between the two media. A medium of refractive index n_1, embedded in a medium of lower refractive index $n_2 < n_1$, acts as a light trap within which optical rays remain confined by multiple total internal reflections at the boundaries. The change of refractive index is obtained by modifying the crystal in a sub-surface layer using different methods such as poling diffusion , ion implantation, doping, laser writing, etc [55]. The common types of optical waveguides are optical fibres and planar or channel waveguides. With the aim to make integrated photonic circuits, we are more interested in the research of planar and channel waveguides.

1.8.1 Planar waveguides

Planar waveguides are optical waveguides where light is confined in just one dimension and can propagate freely on a plane. They have planar geometry (see Figure 1.10) and are fabricated in the form of a thin transparent film with increased refractive index on a substrate, or possibly embedded between two substrate layers. When a thin layer with a slightly increased refractive index is fabricated or deposited on top of some crystal or silica, it functions as a planar waveguide.

Figure 1.10: Schematic of a planar waveguide.

1.8.2 Channel waveguides

In photonics, a channel waveguide has a structure in the form of a stripe of material, with higher refractive index with respect to the surrounding

medium; confining light in 2 directions. In such a waveguides light propagates only along a specific track. This may be a ridge on top of the cladding structure or an embedded channel inside a substrate. There exist useful geometries for channel waveguides including the strip, the embedded-strip, the rib or ridge, and the strip-loaded (see Figure 1.11). Each one of these geometries has some pros and cons [56], that will be briefly reviewed.

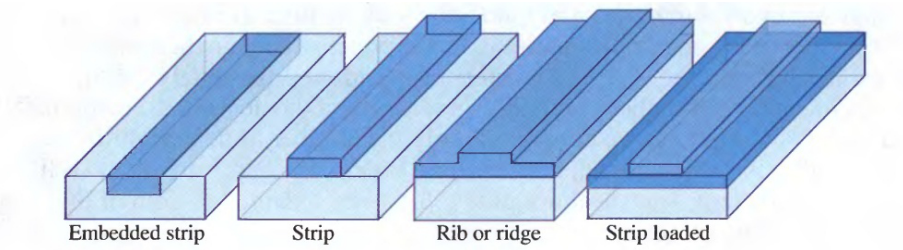

Figure 1.11: Different types of channel waveguides.

Strip waveguide

A strip waveguide is a step-index structure. In the strip waveguide a ridge with higher index of refraction with respect to the substrate is deposited on the top of a planar substrate. This structure produces strong optical confinement within the strip because it is surrounded on three sides by air ($n \approx 1$). This is an important advantage; for example, bend tracks can be much tighter in stripe guide systems than in the other types of waveguides [56].

Ridge waveguide

The ridge or rib and the strip loaded waveguides follow almost the same configuration. There are waveguides in which the guiding layer basically consists of the slab with a strip (or several strips) superimposed onto it. In Figure 1.11 , a three-layer structure has been used, which has a substrate, a planar layer, and then a ridge. The planar layer is arranged as a guide. However, the addition of a further high-index overlay is sufficient to induce guiding in a localised region near the ridge. Confinement of the optical field in the y-direction is obtained because the refractive index, when averaged in the x-direction, is higher in the region of the ridge [56]. The additional ridge overlay may have the same refractive index to that of the planar guide, then we called this kind rib or ridge waveguide, or a different refractive index, in which

case we call it a strip loaded waveguide. The optical losses are lower for rib waveguides than for strip ones. The mode intensity of the rib waveguides are lower in the vicinity of the surface compared to that for the strip waveguides as was demonstrated in [57].

Embedded-strip waveguide

The embedded-strip or buried channel waveguide (see Figure 1.11) is made by modifying the properties of the substrate material so that a higher refractive index is obtained locally. Most fabrication processes result in a weak, graded-index guide buried just below the surface. Although waveguides of this type normally have one axis of symmetry, they usually lack a well defined cross sectional shape. However this structure is often used when its important to keep the properties of the surrounding material.

1.8.3 Fabrication strip for channel waveguides

There exist different methods for the fabrication of channel waveguides. Since this research is focused on the exploration of a novel method to fabricate optical waveguides, a brief review of the most common fabrication methods of channel optical waveguides (strip, ridge and buried) in Si, as well as in LN, will be covered.

Fabrication methods for channel waveguides in Si

The most popular method to make strip optical waveguides in Si [58, 59, 60], consists of three steps. First the substrate materials have to be deposited with a film of Si. CVD processes, Molecular Beam Epitaxy MBE and sputtering are the common deposition techniques. The second step is the patterning process, where the Si surface is covered with a photo-resist polymer layer. The pattern defining process usually includes photolithography, deep-UV lithography, E-beam lithography, or Nano Imprint Lithography (NIL), the patterns are created in this polymer layer on top the sample with the use of a mask, each device requires a specific and unique mask to be imprinted in the sample. Then a developing method is needed where just the selected pattern

remains. The last step is the etching process. This also can be conducted via different methods such as wet etching using etchant liquids as HF, or dry etching like reactive ion etching (RIE), or inductive coupled plasma etching (ICP). These three steps might also be repeated for more complicated structures. Alignment marks need to be created during the first iteration and the subsequent patterns will refer to them. Sample surfaces may need to be polished. Thermal oxidation and annealing might be required in some cases, and so on [60].

Fabrication methods of channel waveguides in LN

There exist different methods to fabricate channel waveguides in LN, in this section we will present the most popular ones. Diffusion is often used to fabricate embedded waveguides in LN [61]. For example, titanium metal can be diffused into lithium niobate or lithium tantalate substrates, by first depositing the metal in patterned strips and then carrying out an in-diffusion at a high temperature about $1000K$ for several hours (3 to 9). This is known as the $TiLiNbO_3$ process [62]. The additional impurities cause a change in refractive index that is approximately proportional to their concentration, with a typical maximum value of $\Delta n \approx 0.01$. Alternatively, material can be exchanged with the substrate. For example, protons (Hydrogen positive ions) can be exchanged with Lithium positive ions in $LiNbO_3$. This is done by first covering the substrate with a masking layer. The crystal is then placed in a suitable hot melt (in this case, benzoic acid, heated to approx 200C), and exchange of material takes place through the crystal surface in regions exposed by the mask openings. Proton exchange yields an index change of $\Delta n \approx +0.12$ for one polarization mode (the TM mode), but the index change is actually negative for the other one [63].

An other way to produce embedded strip waveguides in LN has a 3 steps fabrication [24]. The first step utilizes a CW UV laser direct writing procedure that provides the definition of the strip pattern. Direct writing (DW) of waveguides in congruent LN has been demonstrated using CW UV laser light with writing wavelengths within the range of $244nm - 305nm$, which are below the UV absorption edge of the material. The second step incorporates electric field polling (EFP) to transform the UV written pattern into the corresponding domain pattern via polling inhibition. The stripe structures are finally

produced in the last fabrication step which is wet etching in HF acid. The formation of the stripe structures results from the differential etching between the two opposite polar surfaces of LN in HF acid.

An other technique to produce embedded waveguides in LN [61] is ion implantation, where ions can be implanted in the crystal using an accelerator. This is a large, expensive item of vacuum equipment, which can be used to select a particular species of ions and then accelerate the desired ions electrostatically, so that they strike the substrate surface at high speed and penetrate some distance. Because this process is ballistic, it causes damage to the lattice as well as a change in refractive index. Ion implantation is therefore normally followed by an annealing step, which shakes out the lattice damage. This allows properties that rely on a regular, undamaged crystal lattice (e.g., electro-optic behaviour) to be preserved, and greatly reduces waveguide propagation losses. Following annealing, He+ implantation has been found to be reasonably successful in $LiNbO_3$ [64].

1.8.4 Photonic components

Planar photonic devices are fabricated in different configurations depending on the application. Most of the photonic devices are embedded waveguides with different geometries depending on its use (see Figure 1.12). The most used configurations of embedded-strip photonic devices are: the S bends, which are used to offset the propagation axis; the Y branch, which plays the role of a beam splitter or combiner, the two Y branches, that are used to make Mach Zehnder interferometers, and the two wave-guides in close proximity, used as directional couplers [55].

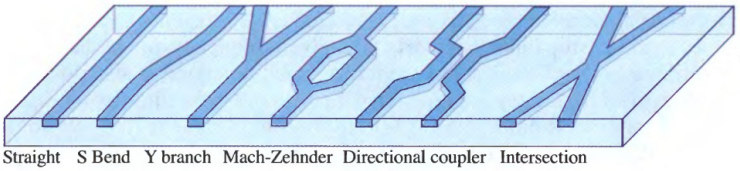

Figure 1.12: Different photonic devices made by embedded waveguide components.

Waveguide propagation Loss

There exist many different methods for determining the propagation loss in optical waveguides. In this research the cutback technique was used. This technique consists of measuring the input and output power of the waveguide for a certain length, then reducing the length of the sample measured cutting few mm and repeating the process, gathering the out put power for each one of those lengths. These results can be expressed in dB and then plotted against the distance removed: a linear fitting is required to estimate the loss per unit length through the waveguides.

In the following chapters, crystallization studies of a-Si by laser irradiation as well as a new method to fabricate silicon ridge waveguides that does not need global heating or any patterning method or aggressive etching will be presented. Also it will be shown another method to manufacture embedded strip waveguides in LN making a permanent change in the index of refraction without the use of poling , diffusion or ion implantation. These methods use a-Si to absorb radiation at visible wavelengths; the absorbed radiation is transformed into heat locally crystallizing a-Si in the case of ridge waveguides or inducing thermal diffusion on the interface with lithium niobate for the case of the LN embedded waveguides.

In summary in this chapter we reviewed briefly the background needed to follow this thesis. All the experiments performed, the analysis and the conclusions will be presented in the next chapters. The first experiment to be covered is the laser crystallization of a-Si on a silica substrate.

References

[1] M. A. Green, "Solar cells: operating principles, technology, and system applications," 1982.

[2] J. T. Clemens, "Silicon microelectronics technology," *Bell Labs Technical Journal*, vol. 2, no. 4, pp. 76–102, 1997.

[3] S. M. Sze and K. K. Ng, *Physics of semiconductor devices*. John wiley & sons, 2006.

[4] N. Healy, S. Mailis, N. M. Bulgakova, P. J. Sazio, T. D. Day, J. R. Sparks, H. Y. Cheng, J. V. Badding, and A. C. Peacock, "Extreme electronic bandgap modification in laser-crystallized silicon optical fibres," *Nature materials*, vol. 13, no. 12, pp. 1122–1127, 2014.

[5] Z. Fang and C. Z. Zhao, "Recent progress in silicon photonics: a review," *ISRN Optics*, vol. 2012, 2012.

[6] G. T. Reed, "Device physics: The optical age of silicon," *Nature*, vol. 46, no. 427, pp. 595–596, 2004.

[7] M. J. R. Heck, J. F. Bauters, and M. L. Davenport, "Hybrid silicon photonic integraed circuit technology," *JSTQE*, vol. 04, pp. 111–113, 2012.

[8] B. Jalali and S. Fathpour, "Silicon Photonics," *Journal of Lightwave Techonlogy*, vol. 24, pp. 4600–4615, 2006.

[9] N. Greenwood and A. Earnshaw, *Chemistry of Elements*. Oxford.

[10] W. Zulehner, "Czochralski growth of silicon," *Journal of Crystal Growth*, vol. 65, no. 1, pp. 189 – 213, 1983.

[11] A. Shah, J. Meier, A. Buechel, U. Kroll, J. Steinhauser, F. Meillaud, and H. Schade, "Towards very low-cost mass production of thin-film photovoltaic (pv) solar modules on glass," *Thin Solid Films*, vol. 502, no. 1, p. 292 299, 2006.

[12] P. Brogueira and J. Conde, "Low filament temperature deposition of a-Si:H by hot-wire chemical vapor deposition," *Journal of Applied Physics*, vol. 78, no. 1, pp. 3776–3783, 1995.

[13] C. K.Long, A.Z.Kattamis and H.Gleskova, "Stability of Amorphous-Siicon TFTs Deposited on Clear Plastic Substrates," *IEEE Electron Device Letters*, vol. 27, pp. 111–113, 2006.

[14] A. Hara, M. Takei, F. Takeuchi, K. Suga, K. Yoshino, M. Chida, T. Kakehi, Y. Ebiko, Y. Sano, and N. Sasaki, "High performance low temperature polycrystalline silicon thin film transistors on non-alkaline glass produced using diode pumped solid state continuous wave laser lateral crystallization," *Japanese Journal of Applied Physics*, vol. 43, pp. 1269–1276, Apr. 2004.

[15] J.-M. Shieh, Z.-H. Chen, B.-T. Dai, Y.-C. Wang, A. Zaitsev, and C.-L. Pan, "Near-infrared femtosecond laser-induced crystallization of amorphous silicon," *Applied Physics Letters*, vol. 85, no. 7, p. 1232, 2004.

[16] J. Michaud, R.Rogel, T. Mohammed-Brahim, and M. Sarret, "Cw argon laser crystallization of silicon films: Structural properties," *Journal of non-cystalline solids*, vol. 352, pp. 998–1002, apr 2006.

[17] R. Nuclaires and L. Phase, "A Thermal description of the melting of c and a-Silicon under pulsed excimer lasers," vol. 36, no. 1959, pp. 1–11, 1988.

[18] E. Fogarassy, *Energy Beam Solid Interactions and Transient Thermal Processing*. Les Editions de Physique, 1st ed., 1985.

[19] W. Zachariasen, *Investigation on the crystallizations of ABO compounds*, vol. 4. Skr Norske Vid-Akad, 1st ed., 1928.

[20] A. Prokhorov and Y. S. Kuzminov, *Physics and chemestry of crystalline lithium niobate*. IOP PUblishing Ltd.

[21] D. Georgiev, R. Baird, I. Avrutsky, and G. Auner, "A systematic study of the formation of nono-tips on silicon think films by excimer laser irradiation," *Mater. Res.Soc.Symp.Proc*, vol. 872, 2005.

[22] I. T. Bodnar and V. P. Yarunichev, "Temperature dependece of refracrtive indices of linbo3,litao3 and (ba,na)nbo3 relative crystals: similarity and difference," *SPIE*, vol. 4467, no. –, pp. 357–367, 2001.

[23] K. Z. Ahiqing Lu and X. Li, *Ferroelectrics - Physical Effects*, vol. 1. InTech, 1st ed., 2011.

[24] S. Mailis, C. Riziotis, I. T. Wellington, P. S. C. Gawith, and R. W. Eason, "Direct ultraviolet writing of channel waveguides in congruent lithium niobate single crystals," *Opt.Lett*, vol. 28, pp. 1433–1435, Apr. 2003.

[25] K. Peithmann, M.-R. Zamani-Meymian, M. Haaks, K. Maier, B. Andreas, K. Buse, and H. Modrow, "Fabrication of embedded waveguides in lithium-niobate crystals by radiation damage," *Applied Physics B*, vol. 82, no. 3, pp. 419–422, 2006.

[26] P. Cheben, R. Soref, D. Lockwood, and G. Reed, "Silicon photonics," *Advances in Optical Technologies*, 2008.

[27] S. Fathpour, "Emerging heterogeneous integrated photonic platforms on silicon," *Nanophotonics*, vol. 4, no. 1, pp. 143–164, 2015.

[28] G. Reed, G. Mashanovich, F. Gardes, D. Thomson, Y. Hu, J. Soler-Penades, M. Nedeljkovic, A. Khokhar, P. Thomas, C. Littlejohns, *et al.*, "Recent results in silicon photonics at the university of southampton," in *SPIE OPTO*, pp. 89890D–89890D, International Society for Optics and Photonics, 2014.

[29] M. Lipson, "Guiding, modulating, and emitting light on silicon-challenges and opportunities," *Journal of Lightwave Technology*, vol. 23, pp. 4222–4238, Dec 2005.

[30] K. P. Yap, A. Delage, J. Lapointe, B. Lamontagne, J. H. Schmid, P. Waldron, B. A. Syrett, and S. Janz, "Correlation of scattering loss, sidewall roughness and waveguide width in silicon-on-insulator (soi) ridge waveguides," *Journal of Lightwave Technology*, vol. 27, pp. 3999–4008, Sept 2009.

[31] J. Cardenas, C. B. Poitras, J. T. Robinson, K. Preston, L. Chen, and M. Lipson, "Low loss etchless silicon photonic waveguides," *Optics express*, vol. 17, no. 6, pp. 4752–4757, 2009.

[32] D. Vermeulen, S. Selvaraja, P. Verheyen, G. Lepage, W. Bogaerts, P. Absil, D. Van Thourhout, and G. Roelkens, "High-efficiency fiber-to-chip grating couplers realized using an advanced cmos-compatible silicon-on-insulator platform," *Optics express*, vol. 18, no. 17, pp. 18278–18283, 2010.

[33] C. Alonso-Ramos, A. Ortega-Moñux, I. Molina-Fernández, P. Cheben, L. Zavargo-Peche, and R. Halir, "Efficient fiber-to-chip grating coupler for micrometric soi rib waveguides," *Optics Express*, vol. 18, no. 14, pp. 15189–15200, 2010.

[34] T. Tsuchizawa, K. Yamada, H. Fukuda, T. Watanabe, J.-i. Takahashi, M. Takahashi, T. Shoji, E. Tamechika, S.-i. Itabashi, and H. Morita, "Microphotonics devices based on silicon microfabrication technology," *IEEE Journal of selected topics in quantum electronics*, vol. 11, no. 1, pp. 232–240, 2005.

[35] P. Koonath, T. Indukuri, and B. Jalali, "Add-drop filters utilizing vertically coupled microdisk resonators in silicon," *Applied Physics Letters*, vol. 86, no. 9, p. 091102, 2005.

[36] G. T. Reed, G. Mashanovich, F. Gardes, and D. Thomson, "Silicon optical modulators," *Nature photonics*, vol. 4, no. 8, pp. 518–526, 2010.

[37] R. Soref and B. Bennett, "Electrooptical effects in silicon," *IEEE journal of quantum electronics*, vol. 23, no. 1, pp. 123–129, 1987.

[38] L. Liao, A. Liu, D. Rubin, J. Basak, Y. Chetrit, H. Nguyen, R. Cohen, N. Izhaky, and M. Paniccia, "40 gbit/s silicon optical modulator for high-speed applications," *Electronics letters*, vol. 43, no. 22, pp. 1196–1197, 2007.

[39] F. Y. Gardes, D. J. Thomson, N. G. Emerson, and G. T. Reed, "40 gb/s silicon photonics modulator for te and tm polarisations," *Opt. Express*, vol. 19, pp. 11804–11814, Jun 2011.

[40] E. L. Wooten, K. M. Kissa, A. Yi-Yan, E. J. Murphy, D. A. Lafaw, P. F. Hallemeier, D. Maack, D. V. Attanasio, D. J. Fritz, G. J. McBrien, *et al.*, "A review of lithium niobate modulators for fiber-optic communications systems," *IEEE Journal of selected topics in Quantum Electronics*, vol. 6, no. 1, pp. 69–82, 2000.

[41] L. Vivien, J. Osmond, J.-M. Fedeli, D. Marris-Morini, P. Crozat, J.-F. Damlencourt, E. Cassan, Y. Lecunff, and S. Laval, "42 ghz pin germanium photodetector integrated in a silicon-on-insulator waveguide," *Optics express*, vol. 17, no. 8, pp. 6252–6257, 2009.

[42] M. J. Heck, J. F.Bauters, L.Devenport, and J. E. Bowers, "Lithium niobate: Summary of physical properties and crystal structure," *Appl. Phys. A, Solids Surf*, vol. 37, pp. 191–203, 1985.

[43] F. Ay and A. Aydinli, "Comparative investigation of hydrogen bonding in silicon based pecvd grown dielectrics for optical waveguides," *Optical Materials*, vol. 26, pp. 33–46, Apr. 2004.

[44] P. Capezzuto and A. Madan, *Plasma deposition of amorphous silicon-based materials*. Academic Press, 1995.

[45] M. Moravej, S. E. Babayan, G. R. Nowling, X. Yang, and R. F. Hicks, "Plasma enhanced chemical vapour deposition of hydrogenated amorphous silicon at atmospheric pressure," *Plasma Sources Science and Technology*, vol. 13, no. 1, p. 8, 2004.

[46] R. Schropp, "Industrialization of hot wire chemical vapor deposition for thin film applications," *Thin Solid Films*, vol. 595, Part B, pp. 272 – 283, 2015. 8th International conference on hot-wire {CVD} (Cat-CVD) processes (HWCVD 8).

[47] S. Filonovich, P. Alpuim, L. Rebouta, J.-E. Boure, and Y. Soro, "Hydrogenated amorphous and nanocrystalline silicon solar cells deposited by {HWCVD} and rf-pecvd on plastic substrates at 150 c," *Journal of Non Crystalline Solids*, vol. 354, no. 1925, p. 2376 2380, 2008.

[48] A. Mahan, Y. Xu, E. Iwaniczko, D. Williamson, B. Nelson, and Q. Wang, "Amorphous silicon films and solar cells deposited by {HWCVD} at ultra-high deposition rates," *Journal of Non-Crystalline Solids*, vol. 299 302, Part 1, p. 2 8, 2002. 19th International Conference on Amorphous and Microcrystalline Semiconductors.

[49] T. M. B. Masaud, A. Tarazona, E. Jaberansary, X. Chen, G. T. Reed, G. Z. Mashanovich, and H. M. H. Chong, "Hot-wire polysilicon waveguides with low deposition temperature," *Opt. Lett.*, vol. 38, pp. 4030–4032, Oct 2013.

[50] D. A. Long and D. Long, *Raman spectroscopy*. McGraw-Hill New York, 1977.

[51] Y. Repelin, E. Husson, F. Bennani, and C. Proust, "Raman spectroscopy of lithium niobate and lithium tantalate. force field calculations," *Journal of Physics and Chemistry of Solids*, vol. 60, no. 6, pp. 819 – 825, 1999.

[52] B. Warren, *X Ray Diffraction*. Dover Publications.

[53] C. R. Hubbard, H. t. Swanson, and F. Mauer, "A silicon powder diffraction standard reference material," *Journal of Applied Crystallography*, vol. 8, no. 1, pp. 45–48, 1975.

[54] H. E. Swanson, E. Tatge, and R. K. Fuyat, *Standard X-ray diffraction powder patterns*. US Government Printing Office, 1953.

[55] B. Saleh and M. Teich, *Fundamentals of Photonics*. John Wiley and Sons.

[56] R. Syms and J. Cozens, *Optical Guided Waves and Devices*. McGrawn-Hill Education Europe.

[57] L. Vivien, F. Grillot, E. Cassan, D. Pascal, S. Lardenois, A. Lupu, M. S. Laval, Heitzmann, and J. Fedeli, "Comparison between strip and rib SOI microwaveguides for intra-chip light distribution," *Optical Materials*, vol. 27, pp. 756–752, 2005.

[58] M. J.R., Heck, J. F.Bauters, L.Devenport, and J. E. Bowers, "Hybrid silicon photonic integrated circuit technology," *JSTQE*, vol. 42, pp. 1–17, 2012.

[59] J.aeger and C. Richard, *Lithography, Introduction to Microelectonic Fabrication*, vol. 1. Upper Saddle River: Prentice Hall, 2nd ed., 2002.

[60] Z. Zhang, *Silicon-based Photonic Devices: Design, Fabrication and Characterization*. Royal Institure of Technology (KTH).

[61] M. Armenise, "Fabrication techniques of lithium niobate waveguides," *IEE Proceedings*, vol. 135, no. 2, pp. 85–91, 1988.

[62] L. Tsonev, I. Savatinova, and P. Simova, "Ti:linbo3 optical waveguides," *Applied physics*, vol. 24, no. 3, pp. 205–209, 1981.

[63] M. L. Bortz and M. M. Fejer, "Annealed proton-exchanged linbo3 waveguides," *Opt. Lett.*, vol. 16, pp. 1844–1846, Dec 1991.

[64] G. Reed and B. Weiss, "Low loss optical stripe waveguides in linbo3 formed by he+ implantation," *Elect. Lett.*, vol. 23, pp. 792–794, july 1987.

Chapter 2

Laser crystallization of a-Si on Silica (SiO_2)

2.1 Introduction

Today silicon is on the edge of becoming the material of choice for the photonics industry due to its compatibility with the telecommunications [1] and the mature processing portfolio due to its use in the electronics fabrication for decades. Recently many favourable researches have pushed and stimulated the investments by private sectors, making silicon photonics one of the most active branch in the field of integrated optics [2]. There still exist many challenges that must be solved before its mass production and commercialization, such as the integration with other materials to gain a wider range of applications, and its cost of fabrication and manufacturing. If those obstacles could be solved the impact of silicon will boost up photonics technology, by increasing transmission speed for data and lowering its energy consumption [3, 4]. The motivation of this research is to give practical solutions for those difficulties. Here a suggestion to reduce the cost of manufacturing silicon devices is presented, by starting with a low cost material such as a-Si and then transform it to poly-Si, which is more suitable for photonics and electronics applications [5, 6]. The transformation is accomplished by laser annealing. The full fabrication method will be presented and analysed throughout this thesis. This chapter starts with a short description of the prior art in laser crystallization of a-Si. Then there is an introduction to the method and the experimental set up used to perform

the laser annealing. Finally the results for the experiments on laser annealing of a-Si on silica glass will be shown and discussed.

2.2 Crystallization of a-Si prior art

Optical waveguides made by crystal Si have been fabricated with low optical losses to be used at the IR spectral region [7]. However the process of manufacturing this waveguides have the limitation of a very high temperature or the need for highly controlled environment [8, 9]. This makes c-Si a material with good properties but with many difficulties for big scale fabrication. On the other hand a-Si is a state of silicon which does not require high temperatures to deposit, is more compatible with different substrates and it could be manufactured with an easy process. This is why it has been of interest to use a-Si as a precursor material and look for ways to crystallize it in the pursuit of the useful properties of its crystalline form. Poly-Si has been manufactured with large grain size and low surface roughness with many different process using a-Si as initial material. Common techniques for crystallization of a-Si are thermal and laser-based crystallization. Both have a number of capabilities and limitations.

Films of a-Si can be crystallized by thermal annealing for electronic applications. It has been demonstrated that a-Si deposited on silica substrates were crystallized by rapid thermal annealing: this process consists in placing the samples inside a furnace which reaches a temperature of $> 500°C$ for $4min$ seeding crystallization in the surface with grain sizes of $500nm$ [10, 11]. This crystallization method have been used in the electronics fabrication with good results. In the case of photonics devices have been produced by crystallization of a-Si using thermal annealing [6]: in this process amorphous silicon ridges were patterned using photolitography, followed by a dry etching method and then heated to $1100°C$. This temperature maximizes the crystallized fraction and removes defects from the crystalline regions [12]: these ridge poly-Si waveguides have achieved an optical loss of $9dB/cm$ [13]. The high temperature and the thermal annealing inside a furnace however limits the compatibility with other substrates. So another way to transform a-Si into polycrystalline silicon keeping the optical losses at a low level would be of great interest for photonics applications. This research is focused in the behaviour of a-Si after laser irradiation.

2.2.1 Laser crystallization of a-Si

A thin layer of a-Si can be crystallized by different processes after deposition to recover the excellent electrical properties of c-Si. Crystallization of a-Si has been achieved by femtosecond laser irradiation at a wavelength of $800nm$ [14] and by UV pulsed excimer laser [15]. However pulsed lasers produce small crystals, compared to CW lasers, in the order of tens of nanometers [16]: for this reason these techniques have been used for the fabrication of solar cells [17] and electronics [18] but not for optical circuits.

Another method using CW argon laser with $\lambda = 514.5nm$ has been proposed in [19], where amorphous silicon films were deposited by low pressure chemical vapour deposition at $90Pa$, $550°C$ onto a $300nm$ thick SiO_2 coated corning 1737 glass substrate [20]. In that same research the laser beam was focussed to a diameter of $\backsim 170\mu m$, since their interest was to to produce large area single polycrystalline regions getting single crystals up to a size of $25\mu m$ [21, 22]. High performance transistors were fabricated following this methodology [23], but it has never been used to produce photonic devices.

Some of the limitations presented through this section were spotted and overcome in this project; as the use of a low temperature process to make a compatible material with many substrates especially CMOS materials, also the local annealing of a-Si using smaller beam spot sizes, and the production of pohotonic circuits with large grain size.

From this point I present the experiments, results and analysis of this research work which shows signs of success in the production of photonic devices.

2.3 Experiment Description

A CW visible laser of wavelengths at $488nm$ and $514.5nm$ is focused using an microscope objective, onto a thin layer of amorphous silicon deposited on different substrates. These substrates were: silica glass of $600\mu m$ thickness, crystal silicon of $600\mu m$ with a layer of silica of $4.6\mu m$,to provide optical isolation between the a-Si film and the silicon substrate, and z cut congruent lithium niobate of $500\mu m$ thick. For all these substrates a film of 250 or $400nm$

thick a-Si was deposited regularly on the surface using the HWCVD deposition method at a temperature of 240°C, in the case of LN a-Si deposition with the same thickness by PECVD at 350° was also used. Laser crystallization of a-Si at these wavelengths has been proved to give excellent results in confined geometries as in optical fibres [24]. These samples were mounted upon a two axis computer-controlled stage system to irradiate linear tracks. The power, the speed and the focusing were varied during the experimental process in order to identify the conditions for best crystallization of the a-Si film. Crystallization of the tracks was then analysed using Raman spectroscopy and X-Ray diffraction. In the case of a-Si/SG a wet selective etching was needed to develop the optical waveguides: this part will be cover in the next chapters.

2.3.1 Experimental Set up

The experimental set up used for this research consisted of a CW visible multi-line Argon ion Laser with two main wavelengths at $488nm$ and $514.5nm$ with a Gaussian intensity distribution as the beam source. A refractive microscope objective (L) was used to focus the beam onto the surface of the sample. This microscope objective was mounted onto a linear translation stage in order to control the focusing of the beam. Different magnification objectives were tested (10x,20x,50x). The results presented during this thesis are those obtained with the 20x magnification objective. Even when 50x produced tighter waveguides, the conditions of writing were more difficult to achieve due to the small field of view while laser writing. The samples were mounted upon a two axis computer-controlled translation stage system (Aerotech ABL-1500), were we could set the x and y distance and speeds parameters. The software used to move the stage was g-code. Therefore there exists compatibility with other existing software used already in industries. This makes all the process very compatible with mature manufacturing techniques. The laser power was controlled by an attenuation system. This system uses a combination of a quarter waveplate and a polarizer, in this manner the polarization of the laser was fixed, and the power could be adjusted by rotating the waveplate. A pellicle beam splitter (BS) was used to monitor a portion of the back reflected light using a CCD camera. The CCD camera was used to assist the position of the samples and to visualize the writing process. A schematic of this system can be seen in Figure 2.1.

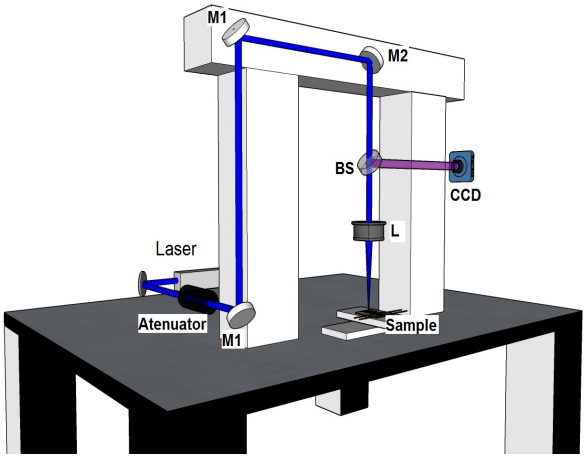

Figure 2.1: System used for laser crystallisation. The sample is mounted on a two axis computer-controlled stage. A beam splitter (BS) was used for CCD visualization of the sample during writing. A microscope objective lens (L) was used to focus the beam on the samples surface.

2.4 Laser crystallization of a-Si on substrate of Silica and on Silica on c-Si

Planar a-Si films were prepared by HWCVD, with two different thickness ($250nm$ and $400nm$) on a SiO_2 substrate with a thickness of $600\mu m$. The samples were scanned in front of the focussed laser beam, using the high precision stages to produce linear irradiated tracks of $\sim 15mm$ length and separated by $100\mu m$. For tracks made by different powers in the samples the speed was fixed to $10mm/min$ and the power of irradiation was varied and measured at the surface of the sample. The laser power to produce damage on the a-Si film of $250nm$ and $400nm$ thick, was identified, corresponding to intensities greater than $3 \pm .05MW/cm^2$ and $3.11 \pm .05MW/cm^2$ respectively. At these intensities the film was completely ablated. Then the laser intensity and the speed of irradiation was varied to identify the best conditions for laser-crystallization. Since the final objective of this experiment would be to produce optical waveguides, obtained on the film of $400nm$ were more interesting. The results for this thickness will be presented.

An overview of a set of irradiated tracks is shown in Figure 2.2. Here a group of $15mm$ long tracks produced using different laser power at constant speed is shown. The first track on the left corresponds to the highest power. For the subsequent tracks the power was decreased by $10mW$ starting at $110mW$

and finishing at $60mW$, in the case of lower powers no significant change of the surface was observed. Using the equation for Gaussian beams through a lens, the beam spot size (ω_0) at the focus position was calculated to be $\sim 1.5\mu m$. However, measuring the width of the damage tracks in the microscope images showed that the affected surface due to the heating propagation was about $6\mu m$. As the focussing was the same for all the annealed tracks the laser powers correspond to intensities of $3.11MW/cm^2$ to $1.69MW/cm^2$. From now on, the laser power will be mentioned instead of the intensity. A change in the colour between each track and the non irradiated part of the sample is observed. This change in colour is attributed to the change in index of refraction due to the crystallization that is taking place in the irradiated part of the sample.

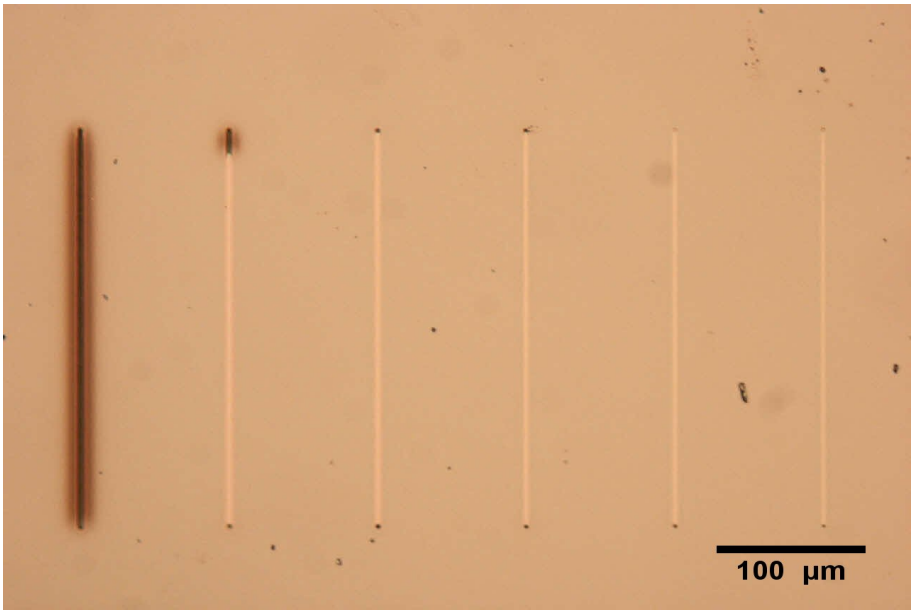

Figure 2.2: Laser irradiated tracks on a-Si/SG corresponding to different laser intensities at a speed of $10mm/min$.The track on the left was irradiated using $110mW$; The power was reduced by $10mW$ for each subsequent track through to $60mW$.

In Figure 2.2 we notice that for the power $110mW$ and $100mW$ there is a darker surface, this colour is associated with ablation of a-Si. In order to make a good quality ridge waveguides this hot spots should be avoided. Then we can conclude that powers lower than $100mW$ are better for this use.

In the case of the thinner ($200nm$) deposition of a-Si the behaviour was very similar, with the only difference of a lower power needed to crystallize. This was expected since a thinner layer of a-Si would need less laser power to have the same conditions. In this case the power that corresponds to a similar behaviour to the $100mW$ for the thinner sample, was $90mW$.

After a-Si/SG was characterized a sample of amorphous silicon of $400nm$ with a substrate of silica on c-Si (a-Si/Sc-Si) was produced. This substrate was chosen because it is known to be compatible with CMOS technology [25, 26, 27], so this compound of materials have captured the attention of many research groups because it blends electronics with photonics [28].

The substrate on this sample has two layers due to the fabrication process. The process begins with a $600\mu m$ c-Si wafer, thermal oxidation produce a layer of $4.6\mu m$ of SiO_2 on the surface of the sample, over this layer the a-Si was deposited by HWCVD. This sample was also characterized for laser annealing. This to demonstrate the different substrates that could be used by this same method. It was found that the intensity required to ablate the material was different: this was expected because the c-Si substrate has a different heat transfer than silica. In this case the range of intensities tried were from $4.24MW/cm^2$ to $2.54MW/cm^2$, corresponding to the powers from $150mW$ to $90mW$. A picture of this is shown in in Figure 2.3.

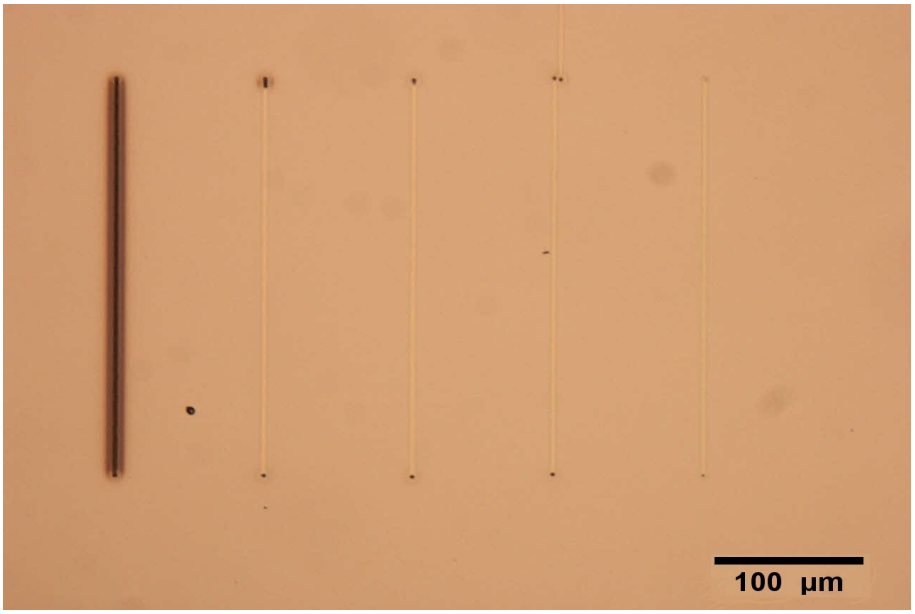

Figure 2.3: Laser annealed tracks on a-Si/Sc-Si corresponding to different laser intensities at a speed of $10mm/min$.The first track was written using $130mW$; changing the power by $10mW$ for each subsequent track through to $90mW$.

For the different substrates we can notice a similar behaviour on the a-Si surface after laser annealing. If the laser power is high the surface becomes darker, this is associated with damage of the a-Si layer. As the power is reduced there is a region where sections of the tracks are damaged. This is due to particles in the surface that cause local absorption hot spots during the laser

writing. Below this power range we found the best conditions where the tracks are continuous without damage. As the power is reduced more the colour of the surface becomes dim until the laser power is not enough to produce any visible effect on the a-Si layer about $25mW$.

2.4.1 Laser annealing of curved structures

Different shapes could be produced by this method, some photonic devices were annealed to check the capability of the stages to produced curves tracks and more complicated patterns. Here there are some pictures of devices annealed that are easy to be implemented. In Figure 2.4 some photonic devices produced by laser annealing in a-Si with a thickness of $400nm$ on glass are shown. In all the curved structures we notice a continuous colour through all the laser annealed surface, this is a good indication of crystallization on a-Si and the smooth movement of the translation stages.

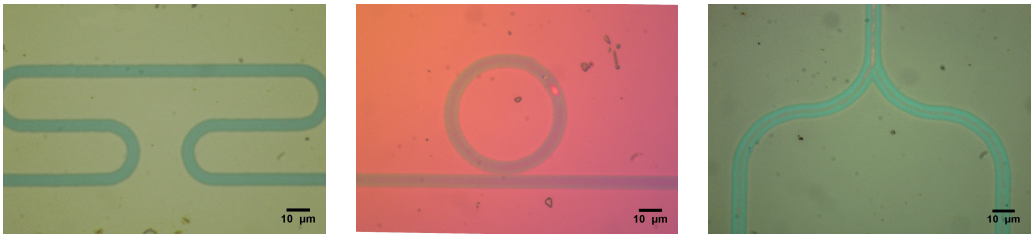

(a) (b) (c)

Figure 2.4: Optical microscope pictures of different devices made by laser annealing of $250nm$ layer of a-Si/Glass. (a)Delay line, (b) ring resonator (c) Y junction.

The use of a popular programming language in industry (g-code) makes easy to develop more complex different shapes and figures that could be laser exposed using this transition stages. The logo of the Optoelectronics Research Center(ORC) at Southampton, was imprinted in a-Si/LN of $400nm$ thickness. An optical microscopy image of the laser crystallized Light logo is shown in 2.5.

In the following part of this experiment the speed for the stage was varied from $1mm/min$ to $20mm/min$. And the Raman spectra for the combination of powers and speeds were acquired and processed.

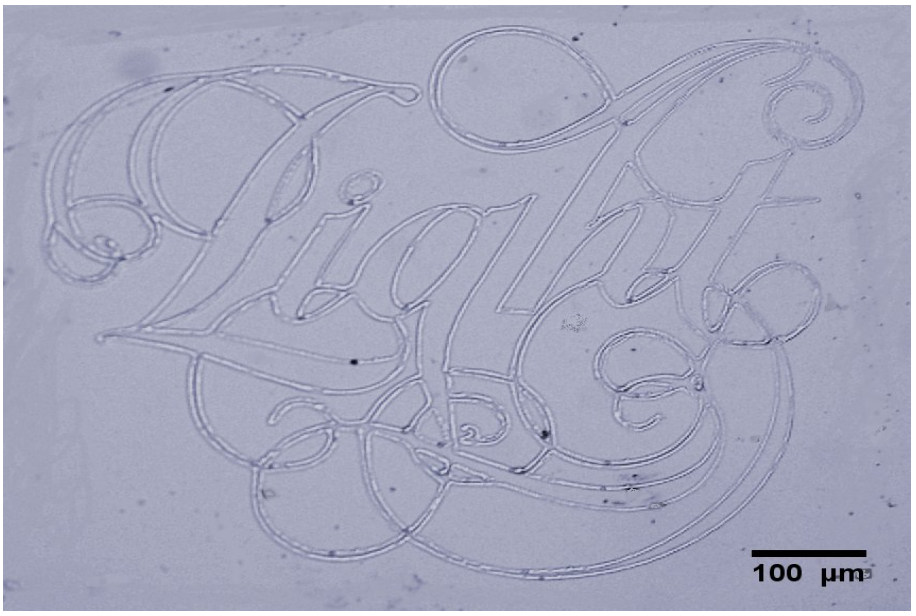

Figure 2.5: Light logo laser-crystallised on a layer of $400nm$ thick a-Si/SG.

2.4.2 Raman Spectroscopy on a-Si/G and a-Si/Sc-Si

As discussed in Chapter 1 Raman Spectroscopy is a good analytical tool to assess the quality of the crystallization process[29]. Raman spectra were obtained from laser written tracks corresponding to different laser powers and to a c-Si reference. In Figure 2.6, we observe that the spectra obtained from the track that corresponds to power condition of $90mW$ in a-Si/SG has the narrowest peak, resembling more the reference spectrum obtained on a c-Si sample than the others powers. It is expected that this particular irradiation condition achieves the best crystallization quality.

To have a quantitative comparison between the reference and the samples it is needed to measure the Full Width at Half Maximum (FWHM) of each spectra and compare them to the reference. All the Raman peaks were fitted using a program coded in Matlab with a Voigt function , which is a convolution of a Gaussian and a Lorentzian profile [30]. The Gaussian contribution is caused by the Raman Spectrometer and the Lorentzian function is attributed to the laser source.

As is shown in the graph at Figure 2.7 each Raman spectra was fitted using a Voigt function, this function has contribution from a Lorentzian and Gaussian distributions. The code used the reference file obtained from a single c-Si wafer and force the Lorentzian FWHM part to be $2.7cm^{-1}$ [31],

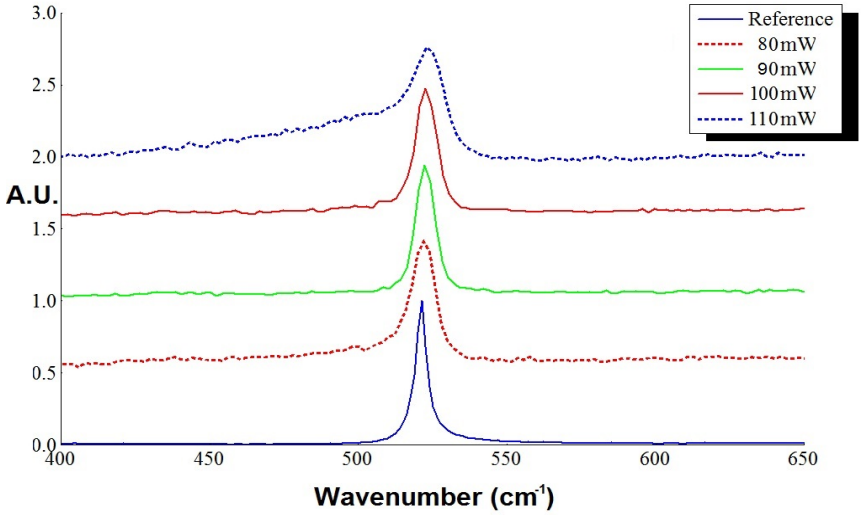

Figure 2.6: Raman spectra corresponding to irradiated tracks obtained with different writing powers and a fixed speed of $10mm/min$

in this manner the Gaussian contribution is found, in this case the Gaussian FWHM contribution was of $2.09cm^{-1}$. The error from the Raman spectrometer was estimated taking the spectra of the c-Si reference 10 times, then fitting using the Matlab code and calculating the average in this measurements. In this way the Lorentzian FWHM of the single c-Si wafer was estimated to be $2.7 \pm .02cm^{-1}$. Another aspect found by this method was the peak position of the Voigt function for this case was centred at $519.77cm^{-1}$ which also gives an indication of the crystallization quality [31].

Finally the FWHM of the Lorentzian part associated with the Voigt function, using the constant Gaussian contribution is calculated for each spectrum. An example of this could be seen in the graph at Figure 2.8. This spectra corresponds to a laser annealed track made by the conditions of $90mW$ and $10mm/min$. In this image the Gaussian contribution was kept constant with the same value as the one found for the reference . The FWHM of the Lorentzian was estimated and found to be of $3.14cm^{-1}$. In the same Figure we can notice the position of the c-Si reference in the black vertical line and the new position of the Voigt fitted (red vertical line) for this particular case was of $517.51cm^{-1}$. A similar shift between the reference and all the measurements was found; this displacement of the peak from that of single crystal silicon implies the existence of defects and amorphous material, that surround the crystal grains, which are associated with vibrations at frequencies in the

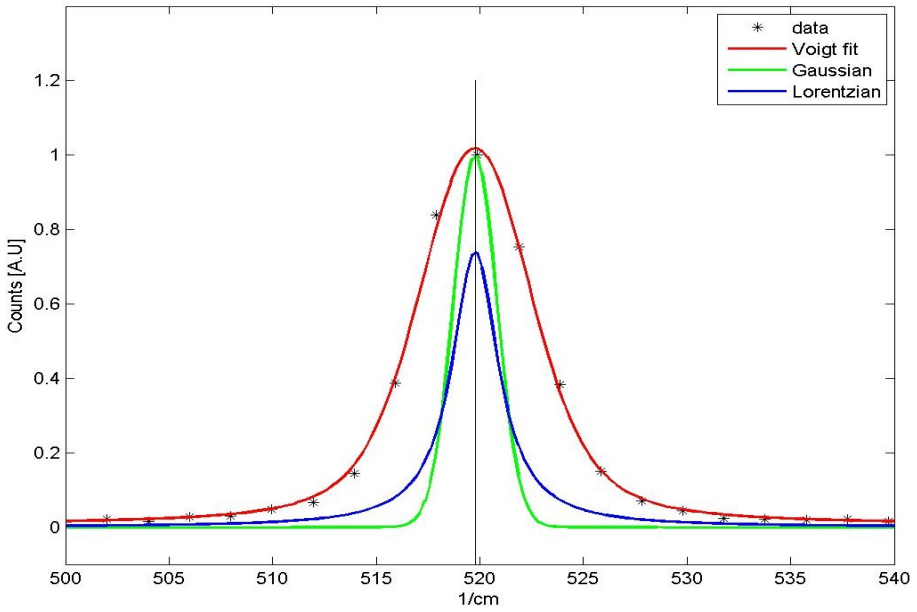

Figure 2.7: Raman spectra from a c-Si wafer, in red the voigt fitted curve, in Blue the Lorentzian contribution with a FWHM of $2.7cm^{-1}$ caused by the laser source and in green the Gaussian contribution which is caused by the instrument. Vertical line points the Voigt peak position.

range 500 to $517cm^{-1}$ [32]. For this reason we can correlate a polycrystalline structure in the irradiated areas of a-Si.

We could attribute a better crystallization of the tracks when their value of the estimated Lorentzian FWHM is closer to $2.7cm^{-1}$ [33]. From here on FWHM will refer to the Lorentzian FWHM to compare each one of the laser crystallisation conditions and samples, used in the experiments, with the c-Si reference. The collected Raman data for different conditions are presented below.

Table 2.1: Table of the Raman peak FWHM for different speeds/Powers for laser-crystallised a-Si on silica substrate (*experimental error, NR not recorded.)

	FWHM in cm^{-1} for different speeds				
Power (mW)	5mm/min	7mm/min	10mm/min	20mm/min	60mm/min
110	20.13	13.31	12.30	12.42	25.12
100	4.57	4.53	4.18	4.39	15.23
90	3.08	3.02	3.14	3.21	14.24
80	3.17	3.26	8.84	12.18*	NR
70	4.65	4.41	4.51	4.51	15.48

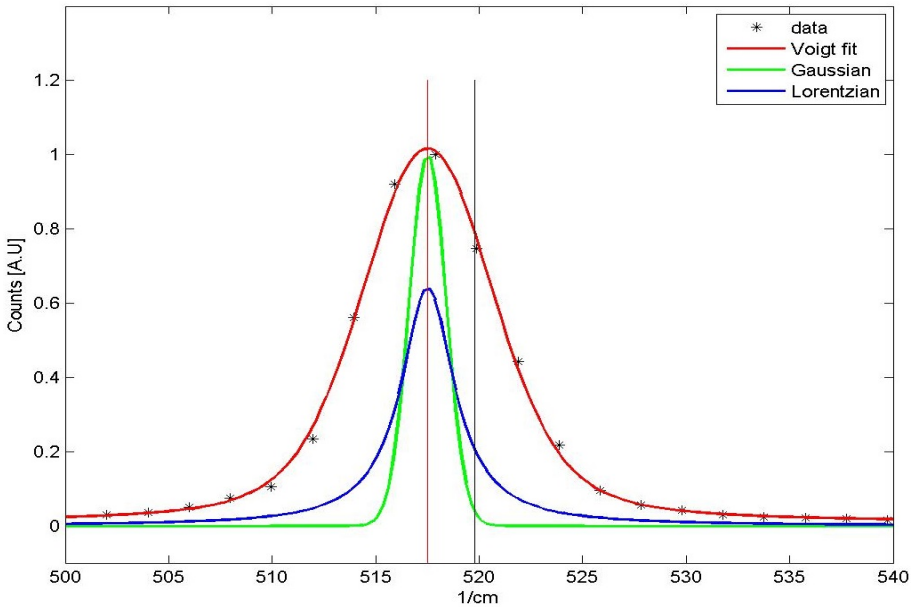

Figure 2.8: Raman spectra from a laser-crystallized track produced by $90mW$ and $10mm/min$. In red the voigt fitted curve is plotted, in Blue the Lorentzian contribution with a FWHM of $3.14cm^{-1}$ and in green the constant Gaussian contribution of $2.09cm^{-1}$. The vertical black line points the Voigt peak position of the c-Si reference the red one the Voigt peak for this fitting.

From table 2.1 we found that the best crystallization according to the Raman spectra was obtained for power $90mw$ for speeds between $5 - 20mm/min$. The lowest value for FWHM however corresponds to a speed of $7mm/min$ which implies the best crystallization achievable, after this speed in all the samples the FWHM increases. Faster speeds where tried too, as an example of those in the same table some Raman data for $60mm/min$ are shown. During the experiments it was notice that speeds larger than $20mm/min$ produced lower crystallization values than lower speeds. Then for the next experiments the maximun speed presented was this one, since we focus in the best crystallization conditions.

For the case of a-Si/Sc-Si the results of the FWHM for the different conditions are presented in the next table.

From table 2.2 we found that the best crystallization according to the Raman spectra was obtained for power $120mw$ for all the speeds. For $7mm/min$ however again we obtained the narrowest FWHM. Both results show that at speed of $7mm/min$ in both cases (a-Si/G and a-Si/Sc-Si) produces the best crystallization results.

Table 2.2: Table of the Power and the FWHM for different speeds on Silica on c-Si substrate

	FWHM in cm^{-1} for different speeds			
Power (mW)	5mm/min	7mm/min	10mm/min	20mm/min
120	3.30	3.04	3.12	3.14
110	3.15	3.06	3.17	3.33
100	3.37	3.08	3.14	3.25

All the Raman results indicate that Si crystals are forming after the laser irradiation. Polycrystalline material was found in the tracks after been illuminated by the laser source getting the best results (closer to the c-Si reference $2.7cm^{-1}$) with the conditions for a-Si/G at $90mW$ or $2.54MW/cm^2$ with $7mm/min$ and for the sample of a-Si/Sc-Si at $120mW$ or $3.39MW/cm^2$ with $7mm/min$.

The quality of the laser-processed material has also been investigated using x-ray diffraction, the results of which are presented in the next section.

2.4.3 XRD Analysis Results on a-Si/G

Laser-crystallization results were also corroborated using X-ray diffraction. This investigation was performed at the Diamond Light Source synchrotron located at the Harwell Science and Innovation Campus, Oxfordshire. Using the same set up showed in Figure 1.8. The beam used in the experiment had an energy of $16.8keV$ and a spot diameter of $3\mu m$. However, the beam size could be modified to cover a larger area.

All the diffracted spectra were acquired and analyzed , each diffracted spectra corresponds to the interaction of the track and the area covered by the beam. The analysis as was explained in the previous chapter, consisted in comparing the diffraction spots to the Debye rings associated with the different crystal planes, then the distance shift was measured to find the deformation of the crystal. Scanning along and across the tracks were performed to investigate the length of the crystals on the tracks.

One example of the XRD diffraction spectrum is shown in Figure 2.9.

The position of the diffraction spots obtained from laser annealed samples was compared to the reference pattern shown in Figure 1.9. The

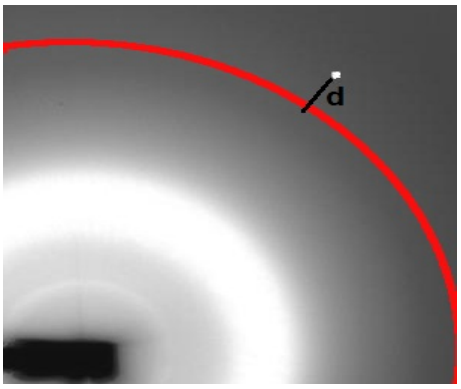

Figure 2.9: XRD pattern showing a single diffraction spot obtained from a laser annealed track. The red circle corresponds to the closest crystal plane obtained from the Si powder reference sample.

distance shift d in Figure 2.9, between the point from the diffraction patterns to the closer circular crystal reference, was measured.

In Figure 2.10, each symbol represents a different crystal plane or one of the three first Debye rings in the diffraction pattern reference: in the x axis the power used to make different tracks is shown and the y axis represents the distance shift from the closest crystal plane to the correspondent spot for the diffraction pattern of each track.

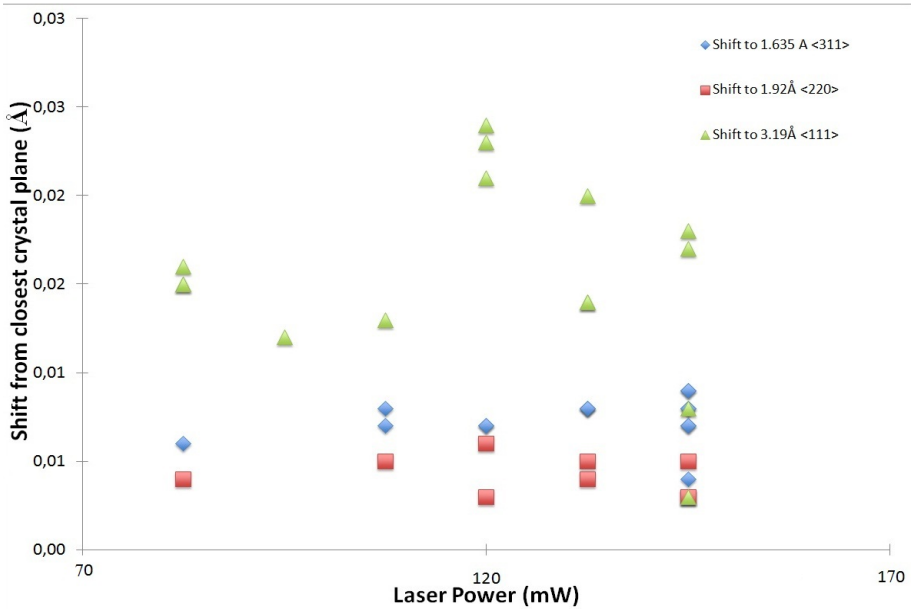

Figure 2.10: Graph of distance Shift from the closest crystal plane vs Power. Data acquired from X-Ray diffraction patterns

From the results can be concluded that the a-Si becomes crystallized and also that tensile strain exists in the crystal since the distance shift was

positive. This tensile strain was due to the fast cooling following the laser irradiation.

Investigation of the crystallized surface along and across the sample were performed to analyze the quality of crystallization and length of crystals that were formed along the tracks. The scanning of the sample across the tracks in a perpendicular manner will indicate any difference in crystal behavior of the laser annealing across the tacks. The scanning along the tracks will indicate the length of the crystals that was achieved. The experiments were performed by scanning the x-ray beam along and across different annealed tracks and acquiring the diffracted pattern for each position during the scanning. Then by monitoring individual diffraction spots for each diffraction spectra the intensity surface was integrated and plotted against the track position. In this type of graphs a higher intensity corresponds to a better overlap between the x-ray beam and the crystal analysed. The track corresponding to the best conditions according to Raman spectroscopy ($90mW$ at $7mm/min$) was scanned across for a distance larger than the cross section of the track, to cover parts corresponding to a-Si.

In Figure 2.11 a graph of the integrated intensity on each diffracted spot against a $12\mu m$ scanning length with $1\mu m$ step is shown. Here we observe that the non-crystallized a-Si corresponds to an intensity of 3 or lower. We also notice a top in this graph with a constant intensity through $4\mu m$, this part belongs to the central ridge of the track, then the intensity drops corresponding to a lower crystallization quality until the a-Si is reached from both sides. The crystallization difference across the track width is due to the fact that the laser beam has a Gaussian intensity profile.

The scanning along the same track was performed for a length of $50\mu m$ with a $4\mu m$ step. The scanning were not possible to place them precisely in the center of the track. Due to the wide of the track, then a small angle between the scanning and the track was needed, so the presented scanning was taken from one side of the track to the other, in a line almost parallel to the track. In this manner we found crystals as large as $32\mu m$ in the best case. In graph 2.12 the position at $0\mu m$ and the position $50\mu m$ are extremes of the same track. This scanning shows the largest crystal found. Here the same spot for each diffraction pattern for each step position over the track was monitored. Finding a higher intensity than the one corresponding for a-Si (3) trough a distance of $32\mu m$.

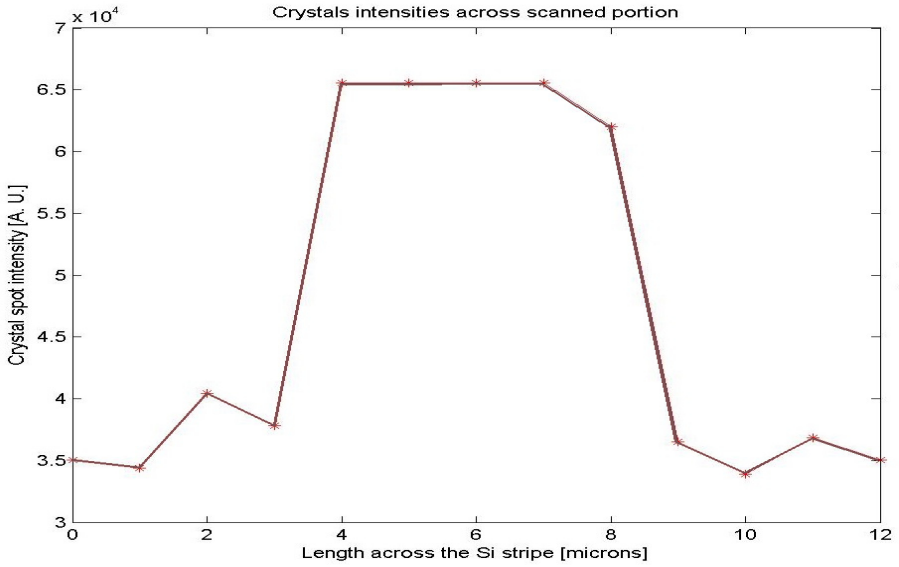

Figure 2.11: In this graph the crystal spot intensity through a scanning length of $12\mu m$ across the laser-crystallized track is presented. We notice that the intensity is higher across a distance of $4\mu m$, also we found out that the intesity corresponding to non irradiated a-Si is of 3.

2.5 Conclusions

During this chapter we have demonstrated laser crystallization of a-Si in two different substrates: a similar behavior on both was spotted, for high powers the surface becomes darker, this is identify as damage on the a-Si layer. The capabilities to produce curved structures using this set up was tested finding that complicated structures could be performed with nice results. The characterization showed that the best power to form continuous crystallized tracks was $90mW$ or $2.54W/cm^{-2}$ and $120mW$ or $3.39W/cm^{-2}$ respectively to the a-Si/G and a-Si/Sc-Si. The power difference is related with the different thermal conduction between the a-Si and the substrate. The change of the writing speed showed a transition in the crystallization due to the cooling rate of the molten silicon: in this experiment it was notice that the best speed to achieved better crystallization in both substrates was $7mm/min$. Raman studies confirm the best crystallization is accomplished with the conditions mentioned finding a close relation of FWHM to a crystal silicon reference. By XRD measurements the formation of crystals along and across the tracks can be totally confirmed finding crystals as large as $32\mu m$ long and a crystallized ridge in the center of the tracks. In the transverse scanning of the tracks a

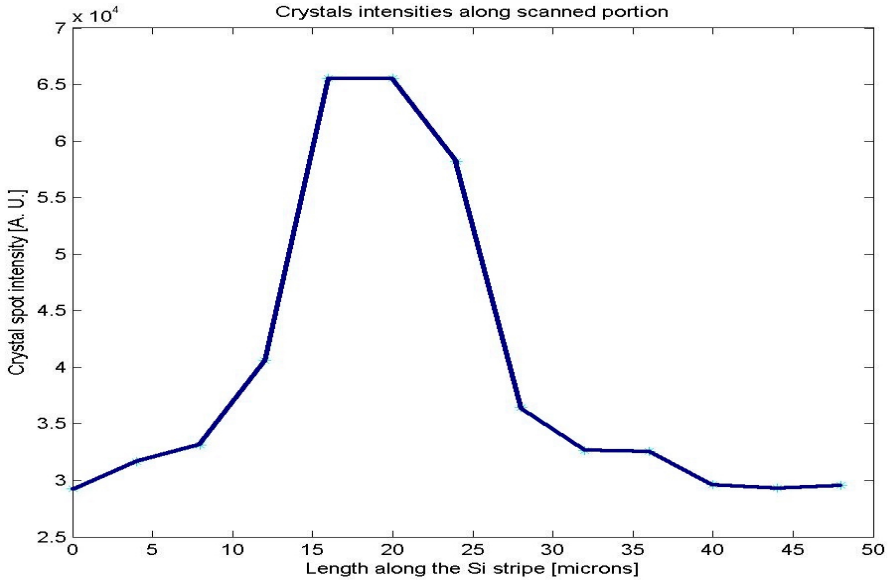

Figure 2.12: In this graph the crystal spot intensity through the scanning of $50\mu m$ along the laser cristallised track is presented. We notice that the intensity is higher along a distance of $32\mu m$.

formation of polycrystalline silicon material in the external sides of the tracks was formed: this is product of the Gaussian intensity distribution of the laser beam.

In summary, all the encouraging results reviewed in the preceding sections prompted the investigation of the a-Si crystallization on active photonic substrates such as LN for the fabrication of hybrid devices. In the following chapters the research results on this subject will be shown. After this point we will concentrate on the behavior of laser writing in amorphous silicon deposited on lithium niobate (a-Si/LN) and the capability of this method for the fabrication of optical waveguides.

References

[1] B. Fathpour and S. Jalali, *Silicon photonics for telecommunications and biomedicine*. CRC Press, 2011.

[2] R. Soref, "The past, present, and future of silicon photonics," *IEEE Journal of selected topics in quantum electronics*, vol. 12, no. 6, pp. 1678–1687, 2006.

[3] G. Denoyer, C. Cole, A. Santipo, R. Russo, C. Robinson, L. Li, Y. Zhou, J. . Chen, B. Park, F. Boeuf, S. Crmer, and N. Vulliet, "Hybrid silicon photonic circuits and transceiver for 50 gb/s nrz transmission over single-mode fiber," *Journal of Lightwave Technology*, vol. 33, p. 1247 1254, March 2015.

[4] M. J. R. Heck, H. W. Chen, A. W. Fang, B. R. Koch, D. Liang, H. Park, M. N. Sysak, and J. E. Bowers, "Hybrid silicon photonics for optical interconnects," *IEEE Journal of Selected Topics in Quantum Electronics*, vol. 17, p. 333 346, March 2011.

[5] M. Lipson, "Guiding, modulating, and emitting light on silicon-challenges and opportunities," *Journal of Lightwave Technology*, vol. 23, pp. 4222–4238, Dec 2005.

[6] K. Preston, S. Manipatruni, A. Gondarenko, C. B. Poitras, and M. Lipson, "Deposited silicon high-speed integrated electro-optic modulator," *Opt. Express*, vol. 17, pp. 5118–5124, Mar 2009.

[7] R. A. Soref and J. P. Lorenzo, "Single crystal silicon: a new material for 1.3 and 1.6 μm integrated optical components," *Electronics Letters*, vol. 21, pp. 953–954, October 1985.

[8] W. Bogaerts, R. Baets, P. Dumon, V. Wiaux, S. Beckx, D. Taillaert, B. Luyssaert, J. V. Campenhout, P. Bienstman, and D. V. Thourhout, "Nanophotonic waveguides in silicon-on-insulator fabricated with cmos technology," *Journal of Lightwave Technology*, vol. 23, pp. 401–412, Jan 2005.

[9] K. P. Yap, A. Delage, J. Lapointe, B. Lamontagne, J. H. Schmid, P. Waldron, B. A. Syrett, and S. Janz, "Correlation of scattering loss, sidewall roughness and waveguide width in silicon-on-insulator (soi) ridge waveguides," *Journal of Lightwave Technology*, vol. 27, pp. 3999–4008, Sept 2009.

[10] G. Liu and S. J. Fonash, "Selective area crystallization of amorphous silicon films by lowtemperature rapid thermal annealing," *Applied Physics Letters*, vol. 55, no. 7, pp. 660–662, 1989.

[11] A. T. Voutsas and M. K. Hatalis, "Crystallized mixedphase silicon films for thin film transistors on glass substrates," *Applied Physics Letters*, vol. 63, no. 11, pp. 1546–1548, 1993.

[12] L. Liao, *Low loss polysilicon waveguides for silicon photonics*. PhD thesis, Massachusetts Institute of Technology, 1997.

[13] L. Liao, D. R. Lim, A. M. Agarwal, X. Duan, K. K. Lee, and L. C. Kimerling, "Optical transmission losses in polycrystalline silicon strip waveguides: effects of waveguide dimensions, thermal treatment, hydrogen passivation, and wavelength," *Journal of electronic materials*, vol. 29, no. 12, pp. 1380–1386, 2000.

[14] J.-M. Shieh, Z.-H. Chen, B.-T. Dai, Y.-C. Wang, A. Zaitsev, and C.-L. Pan, "Near-infrared femtosecond laser-induced crystallization of amorphous silicon," *Applied Physics Letters*, vol. 85, no. 7, p. 1232, 2004.

[15] R. Nuclaires and L. Phase, "A Thermal description of the melting of c and a-Silicon under pulsed excimer lasers," vol. 36, no. 1959, pp. 1–11, 1988.

[16] R. Z. Bachrach, K. Winer, J. B. Boyce, S. E. Ready, R. I. Johnson, and G. B. Anderson, "Low temperature crystallization of amorphous silicon using an excimer laser," *Journal of Electronic Materials*, vol. 19, no. 3, pp. 241–248, 1990.

[17] D. Lowndes, J. Cleland, W. Christie, R. Eby, G. Jellison Jr, J. Narayan, R. Westbrook, R. Wood, J. Nilson, and S. Dass, "Pulsed excimer laser annealing of ion implanted silicon: Characterization and solar cell fabrication," *Applied Physics Letters*, vol. 41, no. 10, pp. 938–940, 1982.

[18] T. Sameshima, M. Hara, and S. Usui, "Xecl excimer laser annealing used to fabricate poly-si tft's," *Japanese Journal of Applied Physics*, vol. 28, no. 10R, p. 1789, 1989.

[19] J. Michaud, R.Rogel, T. Mohammed-Brahim, and M. Sarret, "Cw argon laser crystallization of silicon films: Structural properties," *Journal of non-cystalline solids*, vol. 352, pp. 998–1002, apr 2006.

[20] T. Mohammed-Brahim, M. Sarret, D. Briand, K. Kis-Sion, L. Haji, O. Bonnaud, D. Louer, and A. Hadjaj, "Effect of the starting amorphous structure on the solid-phase crystallization of silicon," *Philosophical Magazine B*, vol. 76, no. 2, pp. 193–212, 1997.

[21] J. F. Gibbons, K. F. Lee, T. J. Magee, J. Peng, and R. Ormond, "cw laser recrystallization of 100 si on amorphous substrates," *Applied Physics Letters*, vol. 34, no. 12, pp. 831–833, 1979.

[22] S. J. Park, Y. M. Ku, E. H. Kim, J. Jang, K. H. Kim, and C. O. Kim, "Selective crystallization of amorphous silicon thin film by a {CW} green laser," *Journal of Non-Crystalline Solids*, vol. 352, no. 920, pp. 993 – 997, 2006. Amorphous and Nanocrystalline Semiconductors - Science and TechnologyProceedings of the 21st International Conference on Amorphous and Nanocrystalline Semiconductors - Science and Technology21st International Conference on Amorphous and Nanocrystalline Semiconductors.

[23] L. Xu, C. P. Grigoropoulos, and T.-J. King, "High-performance thin-silicon-film transistors fabricated by double laser crystallization," *Journal of Applied Physics*, vol. 99, no. 3, p. 034508, 2006.

[24] N. Healy, S. Mailis, N. M. Bulgakova, P. J. Sazio, T. D. Day, J. R. Sparks, H. Y. Cheng, J. V. Badding, and A. C. Peacock, "Extreme electronic bandgap modification in laser-crystallized silicon optical fibres," *Nature materials*, vol. 13, no. 12, pp. 1122–1127, 2014.

[25] H. Wang, M. Chan, S. Jagar, V. M. Poon, M. Qin, Y. Wang, and P. K. Ko, "Super thin-film transistor with soi cmos performance formed by a novel grain enhancement method," *IEEE Transactions on Electron Devices*, vol. 47, no. 8, pp. 1580–1586, 2000.

[26] B. Kuyken, S. Clemmen, S. K. Selvaraja, W. Bogaerts, D. Van Thourhout, P. Emplit, S. Massar, G. Roelkens, and R. Baets, "On-chip parametric amplification with 26.5 db gain at telecommunication wavelengths using cmos-compatible hydrogenated amorphous silicon waveguides," *Optics letters*, vol. 36, no. 4, pp. 552–554, 2011.

[27] H. H. Chen, L. L. Hsu, and L.-K. Wang, "Method for fabricating complementary metal oxide semiconductor (cmos) devices on a mixed bulk and silicon-on-insulator (soi) substrate," Apr. 2001.

[28] M. J. Heck, J. F. Bauters, M. L. Davenport, J. K. Doylend, S. Jain, G. Kurczveil, S. Srinivasan, Y. Tang, and J. E. Bowers, "Hybrid silicon photonic integrated circuit technology," *IEEE Journal of Selected Topics in Quantum Electronics*, vol. 19, no. 4, pp. 6100117–6100117, 2013.

[29] D. A. Long and D. Long, *Raman spectroscopy*. McGraw-Hill New York, 1977.

[30] J. Filik, P. May, S. Pearce, R. Wild, and K. Hallam, "{XPS} and laser raman analysis of hydrogenated amorphous carbon films," *Diamond and Related Materials*, vol. 12, no. 37, pp. 974 – 978, 2003. 13th European Conference on Diamond, Diamond-Like Materials, Carbon Nanotubes, Nitrides and Silicon Carbide.

[31] L. Lagonigro, N. Healy, J. R. Sparks, N. F. Baril, P. J. A. Sazio, J. V. Badding, and A. C. Peacock, "Low loss silicon fibers for photonics applications," *Applied Physics Letters*, vol. 96, no. 4, p. 041105, 2010.

[32] C. E. Finlayson, A. Amezcua-Correa, P. J. A. Sazio, N. F. Baril, and J. V. Badding, "Electrical and raman characterization of and germanium-filled microstructured optical fibers," *Applied Physics Letters*, vol. 90, no. 13, p. 132110, 2007.

[33] J. Jin, Z. Yuan, L. Huang, S. Chen, W. Shi, Z. Cao, and Q. Lou, "Laser crystallization of amorphous silicon films investigated by raman spectroscopy and atomic force microscopy," *Applied Surface Science*, vol. 256, no. 11, pp. 3453 – 3458, 2010.

Chapter 3

Laser crystallization of a-Si on Lithium Niobate

3.1 Introduction

Hybrid integrated photonic devices consisting of silicon photonic circuits combined with materials such as LN have been consider since the inception of silicon photonics [1] to achieve a wider range of functionality. Improved performance optical devices, and implemented multifunction photonic integrated circuits to fullfill various communication applications have been demonstrated [2]. Many different hybrid photonic devices have been fabricated as Mach-Zehnder modulators, hybrid silicon/III-V lasers, silicon nitride-assisted polarization rotators, ring modulators [3, 4, 5]. These multitude of applications have motivated the investigation to merge other materials with Si. As it was presented in the previous chapter CW laser annealing of a-Si could potentially solve the difficulty of combining Si with substrates that possess important photonic properties. Through this chapter, the experiments and results of laser crystallization of a-Si on lithium niobate substrate will be presented. The same order to present the experiments and results followed for the a-Si/G samples in the previous chapter will be extended for the case of a-Si/LN. A similar behavior of the silicon layer is expected but with a difference in the power conditions since, as has been proved, the substrate changes the conditions of the intensity required to crystallize the a-Si layer. It should be mention that in this case the substrate is a crystal structure (LN), compared to the last

chapter where the deposition was in Silica an amorphous material. This difference in the substrates has a crucial play in the adhesion of the materials, making harder to keep in place the a-Si layer deposited in LN. Again a short review of the prior art of combining crystallized silicon with LN substrates will be presented. Then the results for the experimental characterization of laser power and scanning speed will be reported. For these samples, two different methods for the deposition of a-Si were utilized and compared: PECVD and HWCVD. A different behavior associated with the hydrogen concentration in the a-Si layer produced by the deposition method was observed. Finally, the presentation and discussion of Raman spectroscopy and XRD results will be shown.

Silicon devices on LN substrate prior art

Different attempts to combine this two materials to form a hybrid multifunctional photonic devices have been presented in the literature. The most significant of those works are reported in [5, 4, 6]. In these articles a silicon photonic devices have been manufactured using normally complex processes. It begins with a layer of crystallized silicon introduced by direct wafer bonding. This is costly and labour intensive to produce since the initial material is already crystal silicon and the wafers need to be prepared in a highly controlled environment [7].This layer deposition disables the possibility to have a local crystallized area. The next step is the device fabrication by photolithography which need to use an already patterned mask for each optical circuit, limiting the possibility to change the device fabrication during the crystallization process. A final etching step is needed to reveal the devices often perform by dry etching as reactive ion etching (RIE), here all the crystalline surface around the device is removed. Even when this technique has been proved to have very useful results for silicon on LN devices, it could be more efficient and with a lower cost production.

As it was shown in the previous chapter local crystallization by laser annealing of an underdeveloped layer of a-Si on different substrates is possible. We propose to extend this methodology to produce silicon devices on a LN substrate.

3.2 Laser crystallization of a-Si/LN

Amorphous Silicon of two different thicknesses ($200nm$ and $400nm$) was deposited using two different methods: PECVD and HWCVD on the positive face of a z cut lithium niobate crystal with dimensions of $2cm$ by $2cm$ and a thickness of $500\mu m$.

Using the same set up as for a-Si/G, the surface of the a-Si/LN was irradiated with a CW laser with central wavelengths of $488nm$ and $514.5nm$, producing tracks of $15mm$ of length. The irradiation was always in the y direction of the LN crystal to keep the same parameters during the process, in future work other orientations would be tried. The tracks were separated by $100\mu m$ between them. A 20x objective was used with a calculated spot diameter of $\sim 3\mu m$.

As in the a-Si/SG case, first the damage threshold was identified, where we found to be $1.69MW/cm^2$ for $400nm$ thick and $1.56MW/cm^2$ for the thinner film of $200nm$. Further investigations demonstrated that the behavior of crystallization depends just on the thickness of the sample and not in the a-Si deposition method. Since the thinner films exhibit a similar behaviour, with the only difference of a reduction in power of $10mW$ for each condition, just the results for $400nm$ thick a-Si/LN will be presented. For all the experiments the focusing conditions was kept the same so the analysis will be in terms of laser power rather than in intensity. Linear tracks of $15mm$ length were laser irradiated at different laser powers. The laser power was measured after the focusing of the objective lens. The range of laser power used in these experiments varied from $80mW$ to $20mW$ corresponding to intensities on range of $2.26MW/cm^2$ to $0.56MW/cm^2$. The power step between subsequent exposures was $5mW$. A reduction of power needed to ablate the a-Si film was lower than in the other cases of a-Si/S and a-Si/Sc-Si, we think this difference is caused by the thermal conductivity of the materials. LN has better heat conduction then it needs a lower amount of energy to heat a larger area compared to Silica.

3.2.1 a-Si/LN deposited by PECVD

Using the same procedure as previously described in the case of a-Si/SG, we investigated the behaviour on the a-Si/LN sample deposited by PECVD for different powers keeping a constant speed of $10mm/min$ in Figure 3.1.

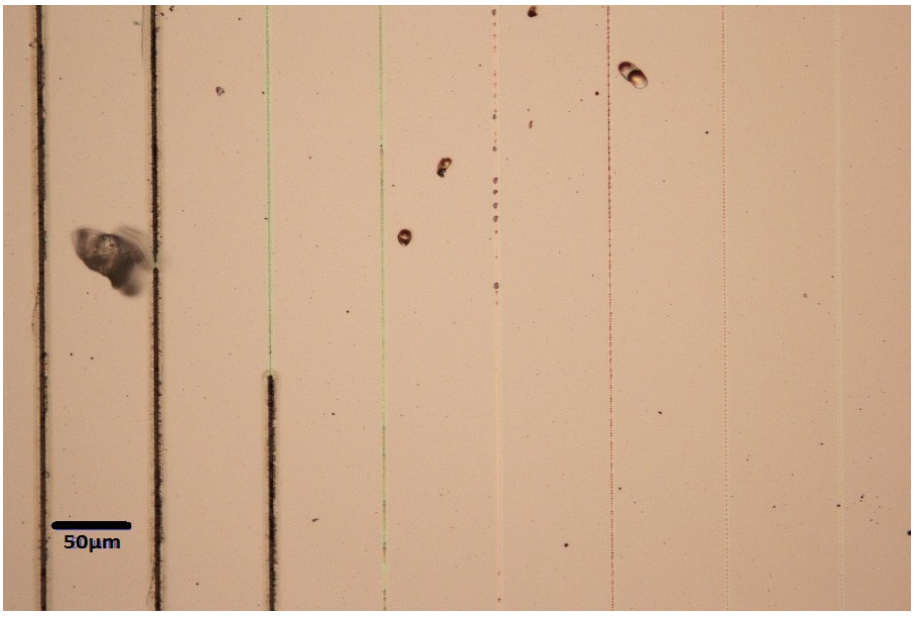

Figure 3.1: Laser irradiated tracks from left to right: with a speed of 10mm/min corresponding to different Powers $60mW$, $55mW$, $50mW$, $45mW$, $40mW$, $35mW$,$30mW$, $25mW$.

An overview of laser irradiated tracks for a range of conditions described before is shown in the optical microscopy image of Figure 3.1. In the first two tracks from the left, which correspond to $60mW$ and $55mW$ respectively, we observe damage on the surface along the irradiated track. The third track, which was laser crystallized with a power of $50mW$, corresponds to the laser damage threshold. However, external elements like dust or other surface defects induce extra absorption hence some parts of the track appear to be damaged. In the fourth track written with power $45mW$, we observe a continuous dark region in the center of the line. For the line written at $40mW$ we observe a continuous and clear line over the entire length. Here we found the best crystallization according to Raman spectroscopy. In the next lines written with powers of $35mW$ and $30mW$, a periodic pearl chain structure appears along the lines. Some research about the origin of the formation of the pearls or blisters has been performed and will be discussed in the next sections. For lower powers than $25mW$ we could not notice any change in the surface.

As with the a-Si/SG samples, the speed was varied from $5mm/min$, $7mm/min$, $10mm/min$ and $20mm/min$. The power was also changed for each irradiated track. Some pictures from an optical microscope for these conditions are shown below with more detail, see Figure 3.2.

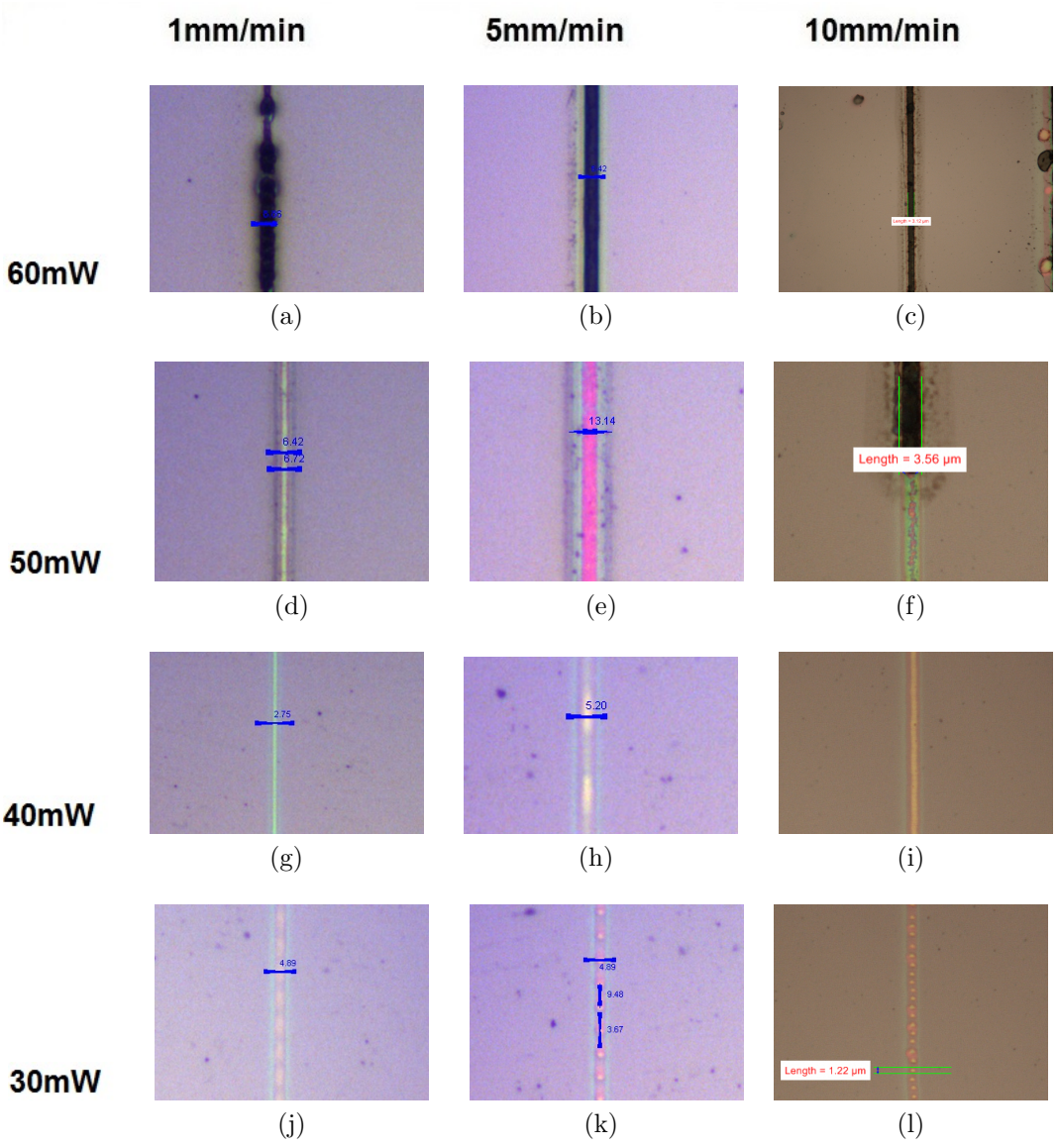

Figure 3.2: Optical Microscopy pictures corresponding to different laser powers, and scanning speeds as indicated

All the tracks in the first row of Figure 3.2 show damage on the surface of the a-Si. For powers below of $50mW$ the damage in the tracks does not appear. At lower powers periodic blister-like structure appear along the tracks. This behaviour was studied in more detail in section 3.2.4.

3.2.2 a-Si/LN deposited by HWCVD

A similar experimental investigation was conducted for the case of a-Si/LN deposited by HWVCD. In Figure 3.3 we observed irradiated lines produced at $10mm/min$ using the same laser power range as in the case of the PECVD samples. A general inspection of the behaviour of the surface after laser annealing shows no blister-chain formation for the lower powers unlike the PECVD case. This is attributed to a lower concentration of hydrogen during HWCVD [8] . Other random bulging features as shown in the track made at $35mW$ at Figure 3.3 appear along the tracks at this power: this could be random concentration of hydrogen in the a-Si layer due to the deposition. However the powers above the blister production have similar results in the annealed surface.

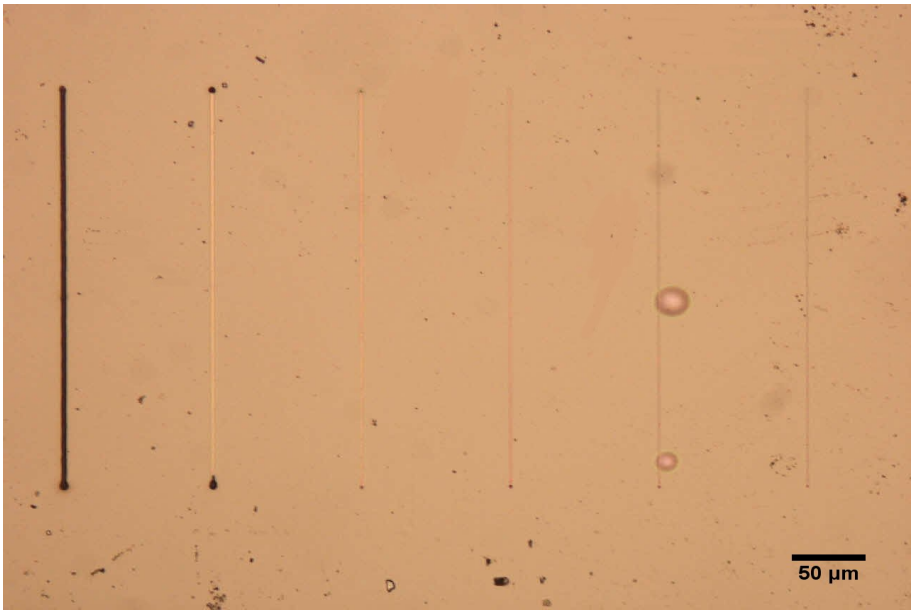

Figure 3.3: All the tracks were laser irradiated with a speed of 10mm/min and different Powers from left to right: $55mW$, $50mW$, $45mW$, $40mW$, $35mW$, $30mW$.

Raman spectroscopy results confirmed the similarity in the crystallization between this two deposition methods. These results will be presented in the following section.

3.2.3 Raman Spectroscopy of laser crystallised a-Si/LN both deposition processes

Results of Raman Spectroscopy analysis of laser irradiated a-Si/LN will be presented here. In Figure 3.4 four Raman spectra obtained from tracks produced with different laser powers at a fixed speed of $5mm/min$ are presented. We observe that the narrower Si line width is achieved for a laser power of $40mW$.

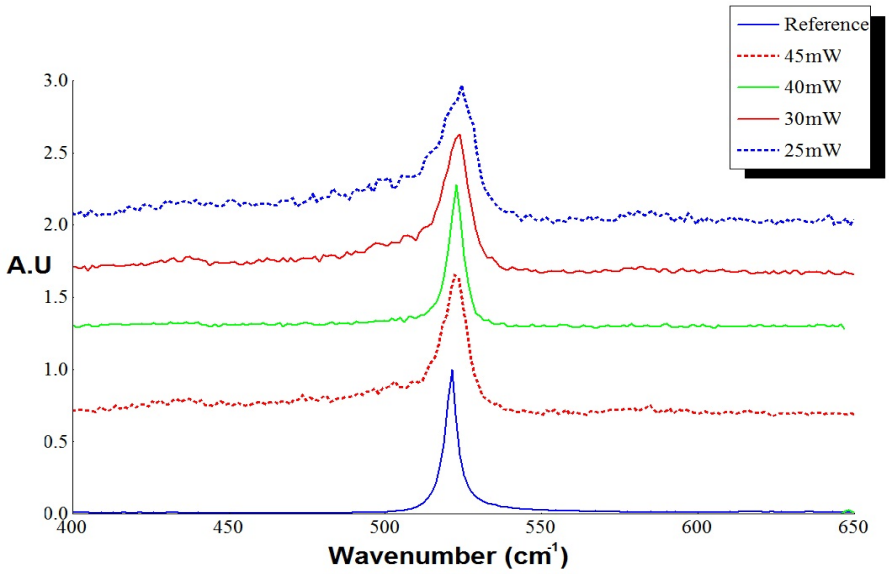

Figure 3.4: Raman spectra for different writing powers with a fixed scanning speed of $5mm/min$

All the spectra were analysed in the same fashion as was explained in Chapter 2, a Voigt function was fitted to the data by fixing the Gaussian width extracted from a c-Si reference, then the FWHM of the Lorentzian contribution from all the tracks was measured.

The FWHM of the Lorentzian fitted data for the irradiated tracks produced using different speeds and laser powers for the a-Si/LN sample deposited by PECVD are presented in Table 3.1.

Table 3.1: Table of the laser Power and the corresponding FWHM for different speeds (PECVD a-Si deposition)

	FWHM in cm^{-1} for different speeds		
Power (mW)	5mm/min	7mm/min	10mm/min
45	4.52	3.48	3.48
40	3.78	3.28	3.38
35	3.874	4.36	3.586
30	20.55	15.86	9.11

We observed that the best crystallization for all the speeds used was achieved for $40mW$ according to the measures with the Raman spectroscope, this power corresponds to a intensity of $1.13MW/cm^2$.

The FWHM of the Lorentzian fitted data for tracks irradiated using different speeds and laser powers, on the sample deposited by HWCVD are presented in Table 3.2 in the same manner as for the case of a-Si/SG.

Table 3.2: Table of the laser Power and the corresponding FWHM for different speeds (HWCVD a-Si deposition)

	FWHM in cm^{-1} for different speeds			
Power (mW)	5mm/min	7mm/min	10mm/min	20mm/min
50	6.09	5.01	5.43	5.69
45	3.42	3.19	3.33	3.59
40	3.29	3.13	3.22	3.62
35	3.58	3.53	3.66	3.76

Also in this case we observe that the best crystallization is achieved for $40mW$ according to Raman spectroscopy results. These results indicate that the deposition method does not affect laser intensity which is required to crystallize a-Si/LN. However in a closer inspection we see that the FWHM achieved are closer to crystalline silicone for HWCVD than the contra part done by PECVD deposition. This results confirms the crystallization of a-Si/LN

and shows that the best deposition method is HWCVD. The laser irradiated samples deposited by HWCVD were investigated by X-Ray diffraction.

3.2.4 Pearl Chain Structures

In this section the results of the investigation on the formation of the periodic pearl chain structures or blisters in a-Si/LN deposited by PECVD will be presented.

These pearl chain structures appear when the irradiating laser intensity is between 0.99 to $0.70 MW/cm^2$. They are only observed on PECVD deposited samples where the hydrogen content due to the deposition technique is grater as compared to HWCVD [9] . The formation of this structures could be associated to the pyroelectric effect of LN. A possible explanation to this phenomena could be explain as follow: due to a quick temperature change, an electrical current is created producing an ignition augmented by the concentration of hydrogen in the a-Si layer. This would be enough to lift the a-Si layer and create small domes.

To investigate more about this phenomenon an a-Si/LN sample deposited by PECVD was thermally annealed at a temperature of $800K$ for 12 hours in order to remove any remaining hydrogen [10]. The laser irradiated tracks were performed at different laser powers. No pearl formation was observed in this sample, demonstrating that this effect must be related to the hydrogen content. Another confirmation of this was recently found in a sample of a-Si/LN deposited by sputtering from a crystalline Si target where no pearl formations were found during the writing, since there was no presence of hydrogen in this deposition process.

To have a closer look at the pearls, the samples were imaged using a Scanning Electron Microscope (SEM). The pictures taken are shown in Figure 3.5. From Figure 3.5 we can conclude that the pearls are formed by deformation and detachment of the Si film from the LN substrate. They are hollow and have a diameter of $\sim 5\mu m$.

The topography of these pearl chain structures was studied using an interferometric contact less surface 3D optical profilometer (ZeScope). We

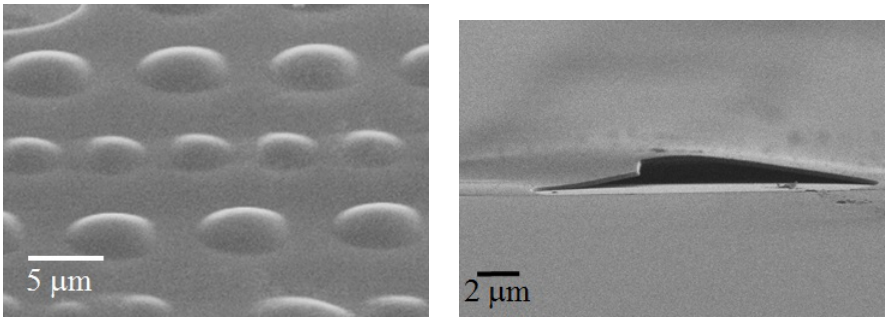

(a) (b)

Figure 3.5: SEM images of the pearl structures found after laser writting on a-Si/LN deposited by PECVD (a) Closer look from the top, (b) side look of a fractured peal showing the hollow nature, and lifting of the film.

present images of them in Figure 3.6, where we observe that the pearls are above the a-Si surface and they have a height of less than $100nm$.

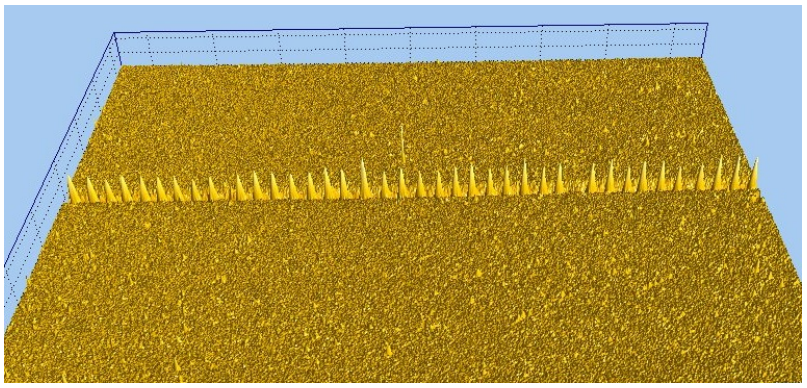

(a)

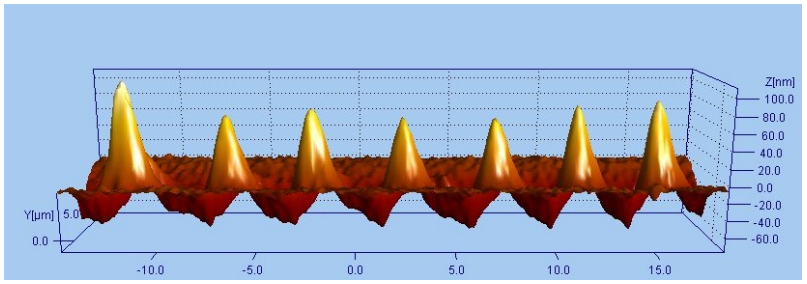

(b)

Figure 3.6: Images generated from ZeScope (a) Surface topography of a pearl chain structure, (b) zooming view of seven pearls with. Note that the hights are of the order of $100nm$.

In order to identify the range of conditions to obtain these periodic structures we will start by studying different writing powers from $35mW$ to $20mW$ and then varying the speed. Optical microscope pictures of this experiment are show in Figure 3.7.

In Figure 3.7 each row of images corresponds to a different power and each track was scanned with different speed. During the next paragraphs a description of all the images will be presented:

- In the first row (images from (a) to (c)) six tracks produced with $35mW$ can be observed. The first three tracks which correspond to speeds $0.1mm/min$, $0.5mm/min$ and $1mm/min$ respectively, do not present pearls chain structures. In the same row the last three tracks which corresponds to the speeds $5mm/min$, $10mm/min$ and $50mm/min$ respectively present spallation, where the Si layer flies off the substrate in solid chunks.

- In the second row (images from (d) to (f)) six lines made with $32mW$ can be observed, the first two tracks which corresponds to the speeds $0.1mm/min$ and $0.5mm/min$ respectively, do not present pearls chain structures. In the same row the next three lines which corresponds to the speeds $1mm/min$, $5mm/min$ and $10mm/min$ respectively, the pearls appear more frequently as the speed increases. In the last line with a speed of $50mm/min$ a periodic mix of pearls and non periodic shapes are found.

- In the third row (images from (g) to (i)) six lines made with $27mW$ are presented. We can be observe that all the lines for all the speeds present pearls chains. The pearls appear more frequently as the speed increases. Also the radius of the pearls decreases as the speed increases.

- In the fourth row (images from (j) to (l)) six lines made with $25mW$ can be observed: all the lines except for the last present pearls chains. The speeds where these pearls appear corresponds to $1mm/min$, $5mm/min$, $10mm/min$, $5mm/min$ and $10mm/min$ respectively. In the same row the last line which corresponds to the speed $50mm/min$ the pearls vanish completely; perhaps the fluency here was not enough to make any change in the a-Si.

- In the last row (images from (m) to (o)) six lines made with $20mW$ can be observed, the first line which corresponds to the speed $0.1mm/min$,

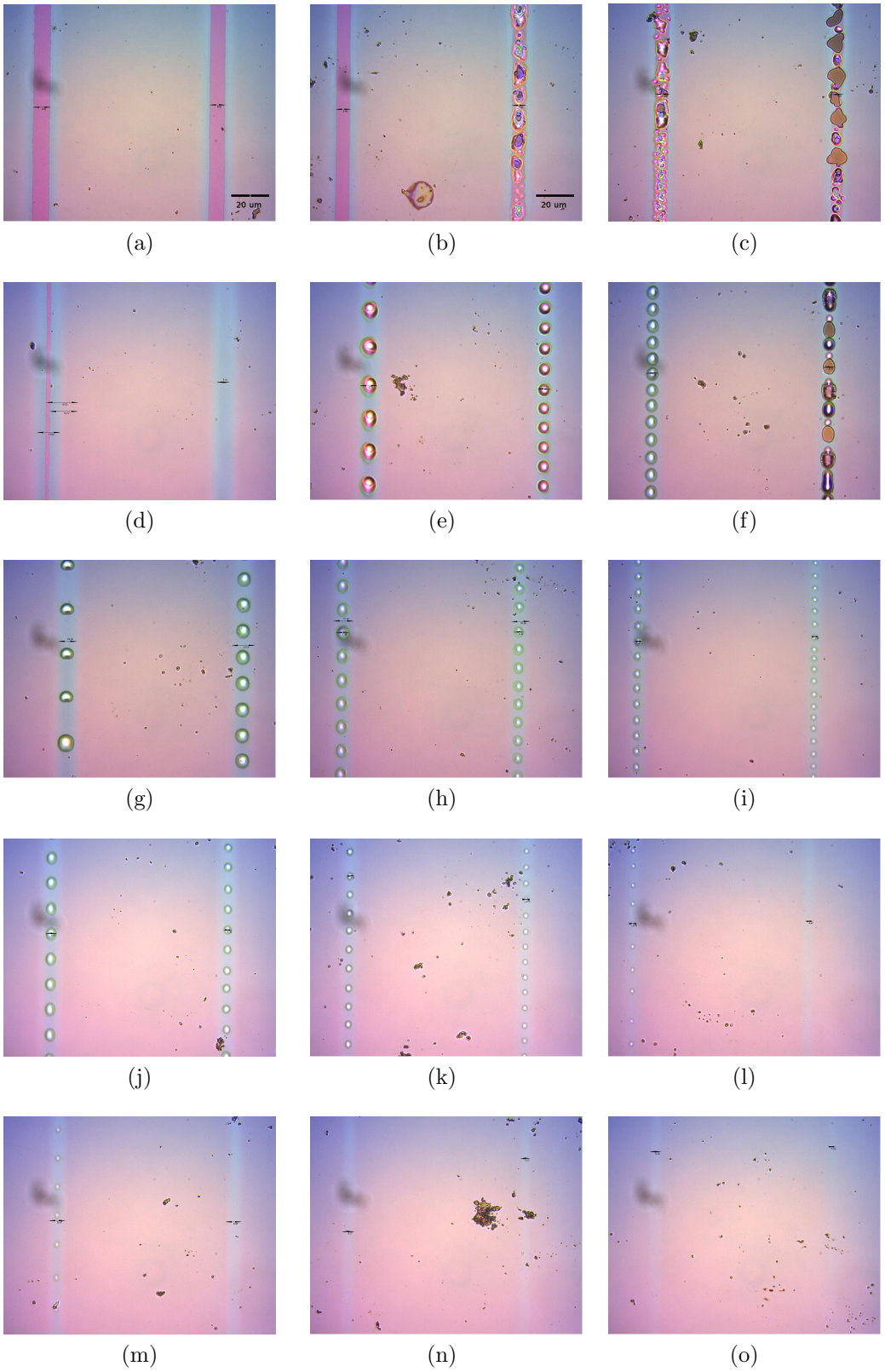

Figure 3.7: Optical Microscopy images of laser irradiated tracks using the parameters for pearl chain structure formations, in this image sequence each row corresponds to different power ($35mW$, $32mW$, $27mW$, $25mW$ and $20mW$) and each column has a different speed for each line in the first row $0.1mm/min$ and $0.5mm/min$, second $1mm/min$, third $5mm/min$, and the last one $10mm/min$ and $50mm/min$

is the only one with pearls chains. In the same row the next lines which corresponds to the speeds $0.5mm/min$, $1mm/min$, $5mm/min$ and $10mm/min$ respectively, doesn't present pearl chains and just blurry lines, for those cases the power was not enough to make any change in the surface of the a-Si.

After analysing the periodicity under different conditions a table with different powers and different speeds was constructed see Table 3.3. Here period 0 means no pearl shapes appearing, i.e. in these cases the lines were solid and continuous or vanished for the lack of power irradiation.

Table 3.3: Table of the speed and the period for different powers.

	Period for different powers				
Speed (mm/min)	32mW	30mW	28mW	25mW	23mW
0.1	0	0	0	0	6.28
0.5	0	4.44	4.6	3.8	3.79
1	4.68	4.35	4.02	3.75	3.71
5	3.269	3.33	3.83	3.57	3.26
7	3.036	3.09	3.65	3.59	3.0
10	2.815	3.29	3.51	3.51	2.65
50	2.544	3.02	3.18	3.5	0
80	0	3.12	3.33	3.26	0

Using the data from table 3.3 a graphic was produced in Figure 3.8. The graph shows that the speed is an important parameter for the periodicity of these pearl chain: it was found that if the speed decreases the period increases.

3.3 Conclusions

In summary, through this chapter we have demonstrated laser crystallization of a-Si deposited on LN by two different deposition methods PECVD and HWCVD. We found a similar behaviour of the laser-crystallization between them with the exception on the formation of periodic pearl like structures in the case of lower powers for the PECVD deposited films. It was found that these pearls have a shorter period for higher scanning speeds. The power for the action of forming continuous crystallized tracks was $40mW$ or $1.13MW/cm^2$ in both depositions methods: this was expected since the substrate and the deposited a-Si thickness were identical. Raman spectroscopy studies confirmed

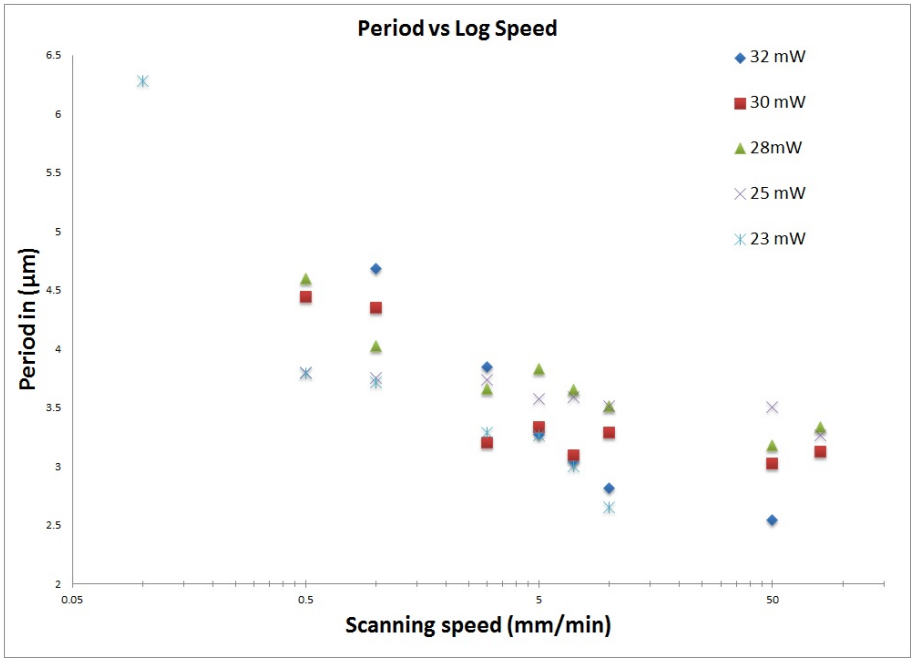

Figure 3.8: Graph of the period vs speed

the best crystallization is again at $7mm/min$ for $40mW$ as it was shown for a-Si/G and a-Si/ScSi. Best result according to the FWHM of the Raman spectra are found for HWCVD, proving that this deposition method is the best of the two for the waveguide purpose. XRD measurements will be shown in the next chapter since it was easier to spot crystallization after annealing once removing the a-Si.

In the next chapter, we will present the fabrication of silicon ridge waveguides by differential etching.

References

[1] R. Soref, "The past, present, and future of silicon photonics," *IEEE Journal of selected topics in quantum electronics*, vol. 12, no. 6, pp. 1678–1687, 2006.

[2] P. Dong, Y.-K. Chen, G.-H. Duan, and D. T. Neilson, "Silicon photonic devices and integrated circuits," *Nanophotonics*, vol. 3, no. 4-5, pp. 215–228, 2014.

[3] L. Chen, Q. Xu, M. G. Wood, and R. M. Reano, "Hybrid silicon and lithium niobate electro-optical ring modulator," *Optica*, vol. 1, pp. 112–118, Aug 2014.

[4] J. Chiles and S. Fathpour, "Mid-infrared integrated waveguide modulators based on silicon-on-lithium-niobate photonics," *Optica*, vol. 1, pp. 350–355, Nov 2014.

[5] P. Rabiei, J. Ma, S. Khan, J. Chiles, and S. Fathpour, "Heterogeneous lithium niobate photonics on silicon substrates," *Opt. Express*, vol. 21, pp. 25573–25581, Oct 2013.

[6] Y. S. Lee, G.-D. Kim, W.-J. Kim, S.-S. Lee, W.-G. Lee, and W. H. Steier, "Hybrid si-linbo3 microring electro-optically tunable resonators for active photonic devices," *Opt. Lett.*, vol. 36, pp. 1119–1121, Apr 2011.

[7] M. Howlader, T. Suga, and M. Kim, "Room temperature bonding of silicon and lithium niobate," *Applied physics letters*, vol. 89, no. 3, p. 031914, 2006.

[8] R. Schropp, "Industrialization of hot wire chemical vapor deposition for thin film applications," *Thin Solid Films*, vol. 595, Part B, pp. 272 – 283, 2015. 8th International conference on hot-wire {CVD} (Cat-CVD) processes (HWCVD 8).

[9] Ay and Aydinli, "Comparative investigation of hydrogen bonding in silicon based pecvd grown dielectrics for optical waveguides," *Optical Materials*, vol. 26, pp. 33–46, Apr. 2004.

[10] R. A. Street, *Hydrogenated amorphous silicon*. Cambridge University Press, 2005.

Chapter 4

Ridge waveguides by differential etching of laser-crystallized a-Si films

4.1 Introduction

In this chapter we will present a differential etching process for the fabrication of silicon ridge waveguides. Etching can be either dry (ion bombardment) or wet (chemical). In dry etching, plasmas or etchant gasses remove parts of the material[2, 3, 4]. This kind of etching is mainly used in conjunction with photolitography where a mask protects the surface that should not be removed [2]. The reaction that takes place utilizes the high kinetic energy of particle beams in the case of physical etching. In this method ion electron, or photon beams are used to etch parts of the materials [3]. There is no chemical reaction taking place and therefore all the materials on the surface will be removed. The etching rate will depend on the material and the energy of the ion beam. Therefore a mask made by a material with slower etching ratio could be used to protect the surface removing faster the unmasked part [5, 2, 3]. The need of a mask deposited to protect the surface adds an additional fabrication step.

Material removal rate for wet etching is usually faster than the rates for many dry etching processes and can easily be changed by varying temperature or the concentration of the etchant mix [6].

Wet etching is based on chemical reaction between the etchant and the material to be etched. Usually the sample is exposed to a liquid or gas chemical component that preferentially attacks exposed parts of the surface. Devices could be developed using a protecting mask or by changing the properties of the surface doping or implanting with different elements the selected surface, then removing with a selective etchant solution the exposed or non treated material [7, 8].

Optical circuits on Si and Silicon on Insulator (SOI) substrates have been produced by wet etching produced [9, 10, 4, 11]. Those production methods have the disadvantage to either using a mask [4, 11], which reduces the versatility of devices and shapes that could be produced since each circuit requires a different mask, or the needing of high temperature treatment to incorporate a dopant [10], limiting the variety of substrates that could be compatible for hybrid integrated optical devices.

A more suitable etching process for the development of ridge waveguides by laser annealing would be one to selectively etch amorphous silicon leaving the crystallized poly-Si on the surface of the substrate. The etching method selected for this research is a wet etching process named Secco-etch ($HF+K_2\ Cr_2\ O_7+H_2\ O$) that selectively removes a-Si and does not affect poly crystalline silicon nor the substrate materials [12]. The laser irradiated film was subsequently subjected to this chemical processing using a combinatorial etchant that preferentially removes a-Si, thus revealing ridge structures that correspond to the the laser crystallized ridges. In the following sections the characterization of the etchant and the surface quality after etching of the different samples will be expose and discus.

4.2 Ridge Waveguide formation

In this section we will review the final step of the process to produce poly-Si ridge waveguides. As was explained in previous sections this method begins by laser-irradiate tracks in the surface of an a-Si film which was deposited on a substrate. These tracks showed crystallization after the laser treatment. A final step is needed to develop the poly-crystalline ridges, a wet etching procedure was chosen to selectively remove a-Si from the crystallized silicon content in the tracks and reveal the poly-Si ridges.

Etching is the final process on this fabrication of ridge waveguides method. A sketch of the general procedure is shown in Figure 4.1.The first and second parts which correspond to deposition and laser annealing have been already cover in the previous chapters. In the following sections the last part, relative to Secco etching will be reviewed.

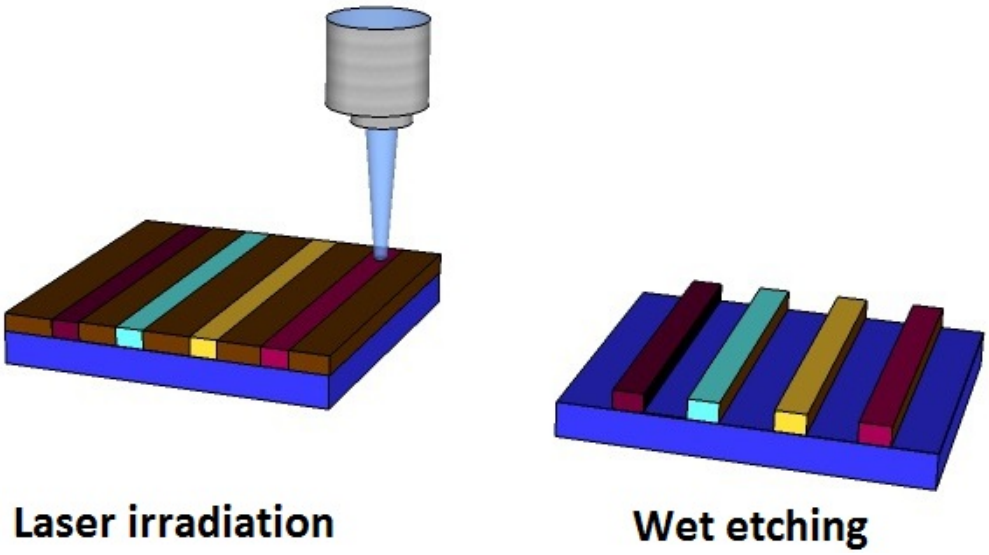

Figure 4.1: Schematic of the two steps of the process followed in this research. First a-Si deposition, Next laser annealing, finally Secco etching revealing the waveguide ridges.

All the samples were wet etched by Secco Etching: this process has been studied to remove crystalline defects on silicon during its fabrication [13]. Different concentrations of Secco mixture where tried to find a reliable etching rate at room temperature. The best concentration was found with $3ml$ of potassium dichromate, $6ml$ of hydrofluoric acid and $90ml$ of water. This etching rate was measured by measuring the height of the ridges with a stylus profilemeter for different etching times. One sample was first submerged in the Secco mix for one minute. The profilemeter measure a $90nm$ high ridge as seen in Figure 4.2 (a). The same sample was submerged for one more minute and scanned across with the stylus profile meter then the ridge develop had a height of $180nm$ as shown in Figure 4.2 (b). Finally this same sample was submerged for 2 more minutes reaching a $4min$ total etching time: the final height after this time was about $400nm$ as the stylus scanning shows in Figure 4.2 c).

The etching rate found was estimated to be $100nm$ per minute. After 3minutes and 45 seconds a layer of $\sim$ $400nm$ of a-Si was removed leaving

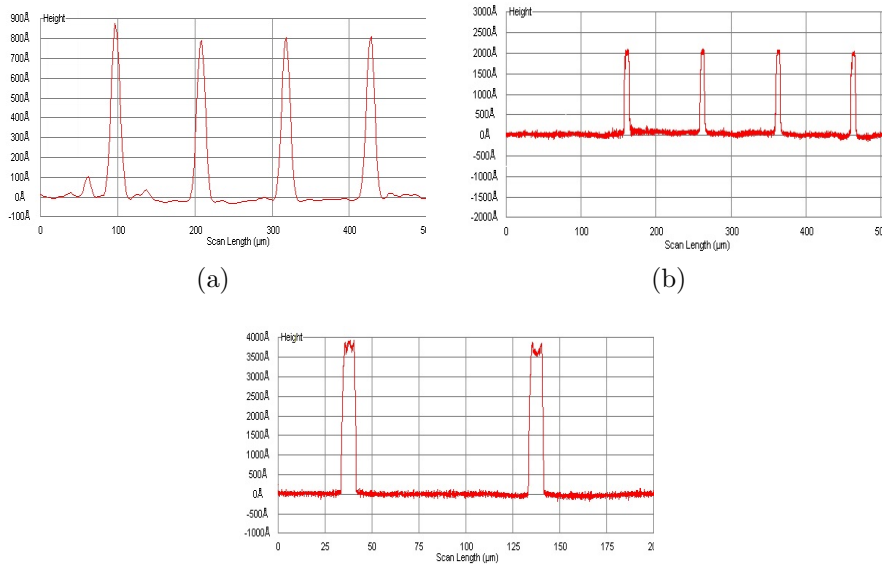

(a) (b)

(c)

Figure 4.2: Surface profilometer scans on ridges after different Secco-etching durations. (a)1min (b)2min (c)4min.

silicon ridges where the irradiation was applied demonstrating a high content of crystalline silicon in this region. This etch duration was kept for all the samples (on different substrates) showing the same etching ratio.

4.2.1 Poly-Si ridges on Silica Glass

Poly-Si ridge waveguides were fabricated by this method on the $400nm$ thick a-Si/SG samples deposited by HWCVD. In Figure 4.3 two images acquired by scanning electronic microscope of different angles from the same ridge are shown. In (a) we observe the polished edge of the ridge. In (b) a top view of the ridge could be seen, here we notice a different texture between the central ridge and the external parts, this was due to the intensity distribution of the laser beam while annealing, since the distribution was Gaussian. The consequence of the Gaussian intensity distribution is a non uniform temperature profile across the irradiated area which affects the quality of crystallisation across the ridge.

More complex structures could be produced using differential etching, as shown in Figure 4.4. In the SEM pictures we could see that they form in the same fashion as the straight ridges after the etching: in all of them we found continuous and solid central ridges and a more porous material at the

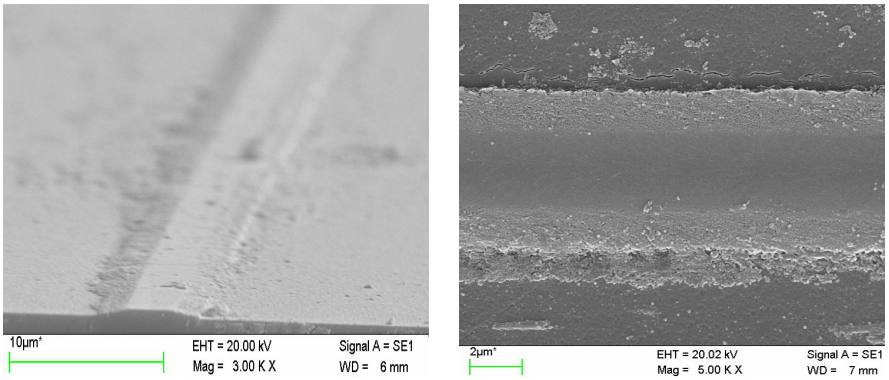

(a) (b)

Figure 4.3: SEM images of a selectively etched ridge structure. (a)Polished edge. (b)top view.

sides of the devices. This results encouraged the continuation of this research to fabricate and test other photonic devices by this same method.

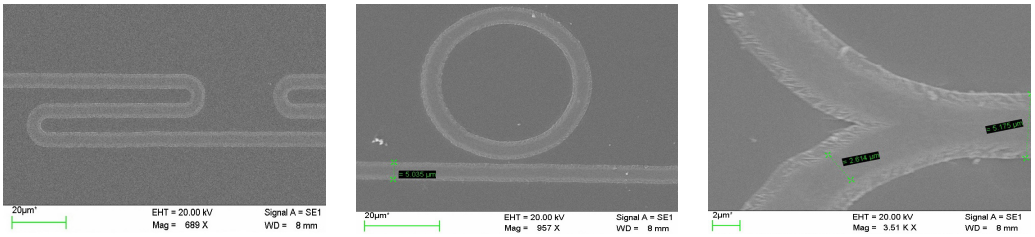

(a) (b) (c)

Figure 4.4: SEM pictures of different devices made by laser annealing of 250nm layer of a-Si/Glass after Secco etching. (a)Delay line, (b) ring resonator (c) Y junction.

Raman and XRD spectroscopic data where collected from the laser irradiated areas before and after Secco etching. An improvement in the crystallization data was found since Secco etching removed smaller crystals, leaving bigger crystals behind, making the contribution of bigger crystals higher after the etching [14]. In table 4.1 FWHM of waveguides made at different conditions are shown after Secco etching. An improvement of the crystallization is spotted since the FWHM are narrower after Secco etching than before etching [15].

XRD data also shows an improvement after etching, revealing larger crystals than before the etching process. A scanning of 50μm with a step of 4μm along a ridge waveguide was performed in the same manner as in Chapter 2. Here we found crystals as large as 48μm.Figure 4.5 shows a graph

Table 4.1: Table of the Power and the FWHM for different speeds on Glass substrate after Secco etching

	FWHM in cm^{-1} for different speeds			
Power (mW)	5mm/min	7mm/min	10mm/min	20mm/min
110	19.78	12.8	11.96	12.25
100	4.27	4.13	3.88	4.12
90	3.08	2.90	3.04	3.09
80	3.10	2.99	3.54	11.96
70	4.42	4.21	4.35	4.32

of XRD over the length of a ridge, revealing the largest crystal found after laser SECCO etching, this crystal has a length about $48\mu m$, in the graph we can just measure a length $38\mu m$ above 3 (which is the lowest value of crystallization) , but the first point was already on the track, then we can assume that the crystal is at least $10\mu m$ larger. This same graph was obtained by monitoring the same crystal spot in sequential XRD spectra obtained at different position along the etched ridge generated along the scanning. In this experiment it was noticed a reduction in the number of crystal spots per diffraction pattern: this confirms a selective etching where just the bigger crystals remain attached to the substrate.

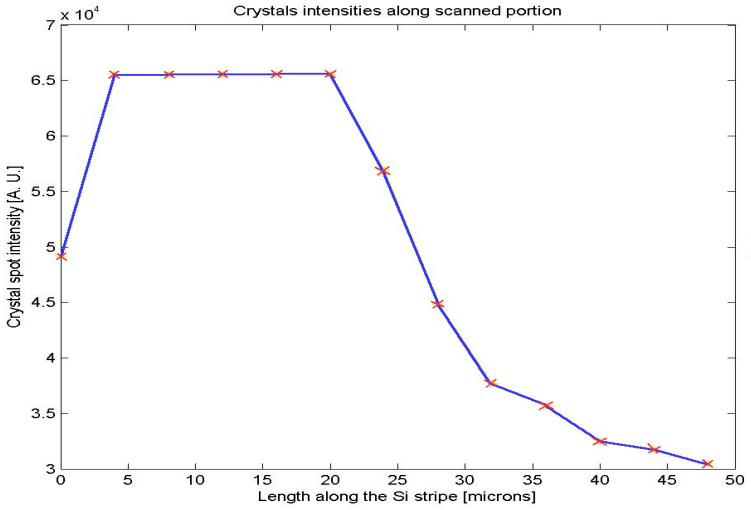

Figure 4.5: In this graph the crystal spot intensity through the scanning of $50\mu m$ is presented.We can notice the intensity higher than 3 (the lowest crystallization) for a length of $40\mu m$

In the next section the transmission loss measurements for the poly-Si ridge waveguides on Silica substrate are reviewed. Cut back method procedure was perform to analyse the loss transmission in the telecommunication spectra.

4.2.1.1 Differentially etched ridge waveguide transmission measurements

Interest in silicon as a material for optoelectronics has increased recently, amorphous silicon waveguide ridges have been developed [16, 17]. In the interest of increasing complexity, density of photonic integrated circuits, and multiple functionality such as the combinations with electronics. Crystalline silicon is of course a suitable material to cover many of these needs [18]. Crystalline silicon on insulator (SOI) substrates are now widely used for making highly efficient photonic integrated circuits [19, 20, 21, 22]. Crystal silicon has been considered for the realization of integrated waveguides reporting losses from 0.1 to $3dB/cm$ [23]. Unfortunately, the high temperature required for the growth of the silica layer, usually in excess of $600°C$ [24] makes c-Si not compatible with temperature sensitive components. To be CMOS compatible, the maximum temperature during all the process should be lower than $400°C$. Another disadvantage of c-Si ridge waveguide, is the complex and costly manufacture methods. Such as epitaxial growth [25, 26]. Addressing these problems provides motivation for this work focusing on a low temperature deposited a-Si followed by local laser annealing to achieve crystallization and finally using a differential etching process to produce poly-Si ridge waveguides.

In this section we will investigate the optical propagation characteristics of ridges that were obtained using this method. Using a laser beam of $\lambda = 1523nm$, light was injected from a polished edge of the ridge using a microscope objective lens. The output was collected by another microscope objective and sent through a relay imaging system, to perform some spatial filtering of the mode. The final ouput was visualised using an IR camera and the transmitted power was measured with an appropriate power meter.

Transmission Loss measurements of poly-Si ridges on Silica

The edges of the samples carrying poly-Si waveguide ridges on silica substrate were polished to facilitate coupling of optical radiation for the purpose of measuring the transmission loss. A He-Ne IR Laser at $1523nm$ with $< 1mW$of power, was coupled in and out of the ridge structures by end-fire coupling using a set up similar to the one sketched in Figure 4.6.

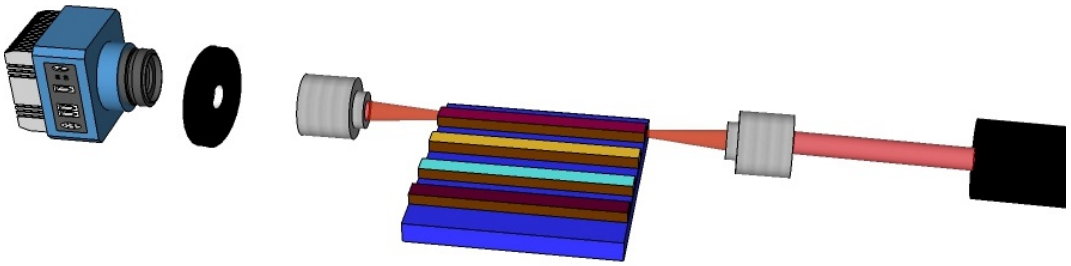

Figure 4.6: Schematic of the loss measurement set up where a 20x microscope objective was used to couple light to each waveguide and a 16x microscope objective as was used to image the mode on a camera.

The near field intensity distribution of the waveguide modes at the output of the ridges were imaged on an IR camera. An iris diaphragm was used for spatial filtering the modes to isolate them and then the power was measured using a powermeter. The polarization was fixed to TM, (No transmission at TE polarization was observed). A $20x$ microscope objective was used to inject the laser into the waveguides and a $16x$ objective was used for imaging. The optical loss was investigated using the cut-back method [27] where $1mm$ sections of the sample were polished off to shorten the waveguide.

Only waveguides produced with 2 different powers were possible to measure through all the process. In Figure 4.7 images of the waveguide modes at the output of ridge waveguides are shown. They correspond to a power of $90mW$. The modes are well defined and have a size of $\sim 6\mu m$ corresponding to the width of the ridges. In (a) a speed of $5mm/min$ was used to produce the waveguide transmitting this mode. In (b)the speed used was $7mm/min$: this mode corresponds to the best conditions for crystallization and corresponds to the best transmission than all the others,as shown in the loss data that will be presented below. Finally on (c) the annealing speed was $10mm/min$.

In graph 4.8 we show the loss measurements for waveguides produced using powers $95mW$ and $90mW$ at different speeds for different lengths. These graphs were obtained using the cut back technique. All the samples where carefully aligned in the set up trying to achieve the same injection conditions: this was confirmed by reviewing the second term in the straight line equation of the fitted lines finding an agreement for all of them.

After fitting a straight line for each set of data as shown in the graphs, the results of the losses are shown in table 4.2. In this table the calculated loss

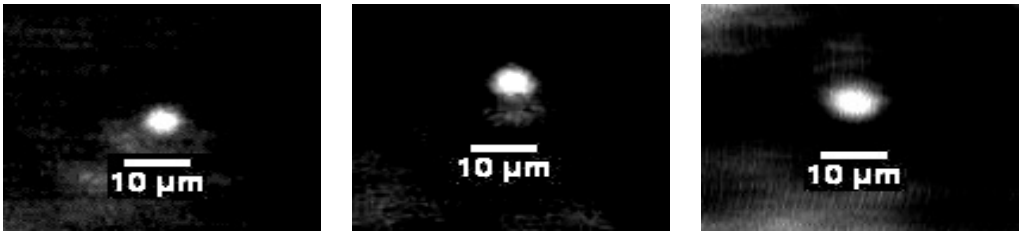

(a) (b) (c)

Figure 4.7: Near field of intensity distributions of waveguide modes through ridge waveguides produced with 90mW and speed of. (a) 5mm/min, (b)7mm/min, (c)10mm/min

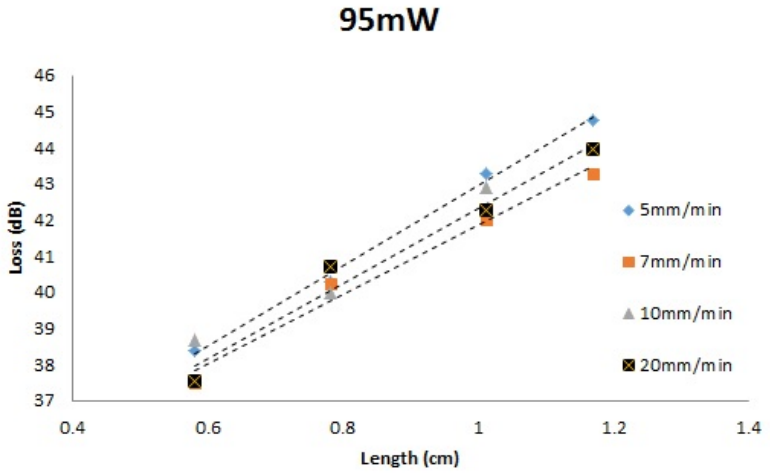

(a)

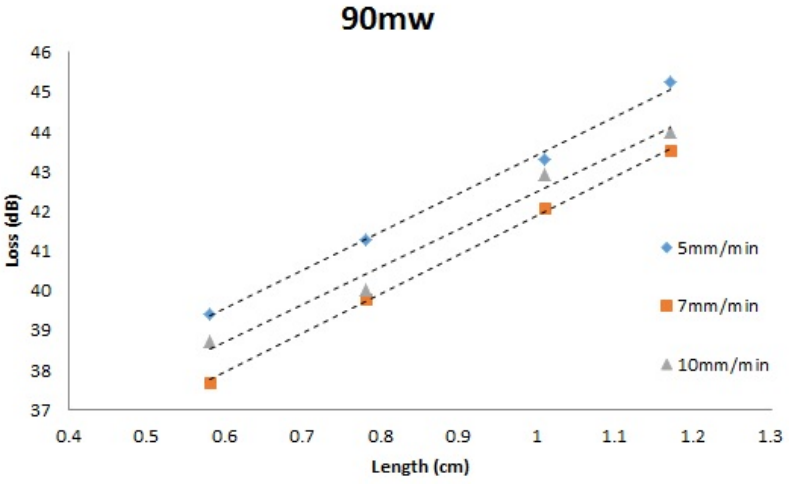

(b)

Figure 4.8: Graph of losses from waveguides with different conditions of speeds and power (a)95mW (b)90mW

for each set of conditions ,power and speeds, is presented: here the losses have units of dB/cm finding the best conditions with the lowest loss with $90mW$ and $7mm/min$ with a value of $9.3dB/cm$

Table 4.2: Table of the fitted slope in the transmission loss data

	Optical Loss in dB/cm			
Power (mW)	5mm/min	7mm/min	10mm/min	20mm/min
95	11.09	9.4	9.6	10.36
90	9.8	9.3	9.6	*No data*

4.2.2 Double annealing of poly-Si ridge waveguides on Silica substrate

Double annealing could potentially reduce the losses in the waveguides resulting in a smoother surface and recrystallizing the ridges. We repeated the laser irradiation of the ridges using a microscope objective that produces a bigger spot than that used in the original crystallization process. That was necessary in order to irradiate the full width of the ridge, that was revealed by Secco etching, with a near-uniform intensity distribution. In this case a 10x objective was used producing a spot size of $\sim 4.5\mu m$ of diameter. Using this objective the laser power to re-crystallise the samples was identified to be between $150mW$ to $120mW$. The intensity range calculated for this second crystallization is from $1.88MW/cm^2$ to $1.50MW/cm^2$. In Figure 4.9 we compare the same ridge before and after the second laser irradiation: we found a less porous ridge sides in the double annealed line and a bigger central part. The small particles surrounding the ridges could be explained as a compound of remaining a-Si that was redeposited during the etching process, and dirt during the gold covering needed to take the SEM images.

The speed to recrystallize was fixed to $7mm/min$ since this speed was proved to have the best results during the previous experiments. Raman spectroscopy after the second annealing was perform in a low quality polycrystalline ridge, with an initial FWHM of $4.15cm^{-1}$, to measure the change in crystallization after the second laser writing: this process showed an increase in the crystallization, according to Raman spectroscopy.

In Table 4.3 the FWHM of the Si Raman peak before and after second crystallisation are compared: we notice an increment in the quality of the

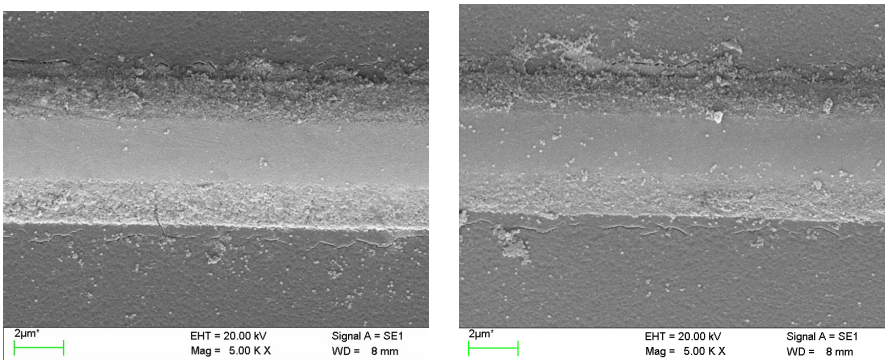

(a) (b)

Figure 4.9: SEM pictures from the top of a-Si/G waveguides. (a) waveguide after Secco etching where the sides are more porous, (b) waveguide after second annealing, central part of the ridge wider and less porous in the ridges.

Table 4.3: Table of the Power and the FWHM for the same waveguide before and after second annealing

	FWHM in cm^{-1}	
Power (mW)	Before	After
120	4.15	2.8

crystallization for the same waveguide after the second annealing which is a very encouraging result.

4.2.3 Poly-Si ridges on Silica on c-Si substrate

Samples of a-Si/Sc-Si were also Secco etched: $400nm$ were totally removed in $4min$ leaving polycrystalline silicon ridges in the annealed tracks. In Figure 4.10 a SEM picture of the silicon ridges in the substrate is presented. As we can notice from the SEM picture there is a solid central ridge with a noticeable different roughness than the external parts. We observe a better reshaping in this substrate compared to a-Si/Glass, making this combination of materials a good option to produce silicon photonic devices.

Raman results after Secco etching for the same conditions as presented in chapter 1 are shown in table 4.4. As was the case for a-Si/SG the crystallization results where improved since the contribution of smaller crystals in the FWHM now is diminished.

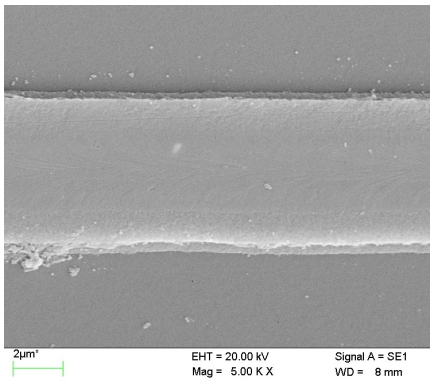

Figure 4.10: SEM picture of one ridge waveguide on a-Si/Sc-Si after Secco etching.

Table 4.4: Table of the Power and the FWHM for different speeds on Silica on c-Si substrate

	FWHM in cm^{-1} for different speeds			
Power (mW)	5mm/min	7mm/min	10mm/min	20mm/min
120	3.16	2.99	3.10	3.05
110	3.05	2.98	3.08	3.17
100	3.16	3.02	3.02	3.13

4.2.4 Poly-Si ridges on LN

Silicon ridges on samples of a-Si/LN were produced using the differential etching method. In Figure 4.11 (a) a top view SEM picture from one of the ridges is shown: we notice a regular ridge developed after the etching with well defined edges. The adhesion between the a-Si film and LN is not very good [28] resulting in section of the ridges being lifted from the substrate during the etching process or during cleaning, polishing. Figure 4.11 (b)shows a SEM image of a silicon ridge with a detached section inside the red rectangle.

In the same manner as for a-Si/SG and a-Si/Sc-Si Secco etching improved the FWHM of the ridges in a-Si/LN. If we compare table 4.5 with the correspondent table before etching present in chapter 3 , we can notice smaller values of the peak widths. This is due to preferential removal of smaller crystals by the etchant.

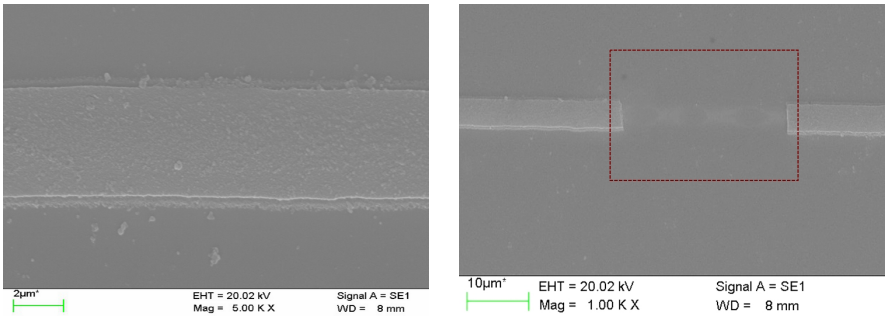

(a) (b)

Figure 4.11: SEM pictures of a-Si/LN waveguides. (a) Detached part of one waveguide (b) Frontal part of detached waveguide inside a red rectangle

Table 4.5: Table of the Power and the FWHM for different speeds

	FWHM in cm^{-1} for different speeds			
Power (mW)	5mm/min	7mm/min	10mm/min	20mm/min
50	5.85	4.36	5.12	5.25
45	3.12	3.06	3.13	3.42
40	3.11	3.03	3.08	3.50
35	3.36	3.23	3.45	3.51

4.2.4.1 XRD Analysis on laser-processed a-Si/LN

A different set up was required to perform ray diffraction experiments on crystallized a-Si on lithium niobate. This is due to the fact that the substrate was single crystal LN producing strong diffraction during the X-ray experiments making difficult to identify the c-Si diffracted spots. Diffraction associated with LN is very close to the Si diffraction positions. This made it difficult to distinguish diffraction from Si crystals with diffraction from LN. Then a different set up was needed to investigate the crystallized a-Si on this substrate. The samples were placed in a manner where the x-ray beam was incident at an angle of 10° . A schematic of this set up is shown in Figure 4.12. Due to this positioning the beam distribution on the surface at the sample forms an oval with a major axis of $30\mu m$ and a minor axis of $3\mu m$. The major axis was placed along to the ridges to maximize the interaction between the beam and the annealed surface. Again a Si powder sample was used as a reference. Unfortunately this set up distribution has the disadvantage to reduce the length of the scanning to just $10\mu m$. The scanning were performed perpendicular to the ridges. Some qualitative results could be observed for

different annealing conditions.

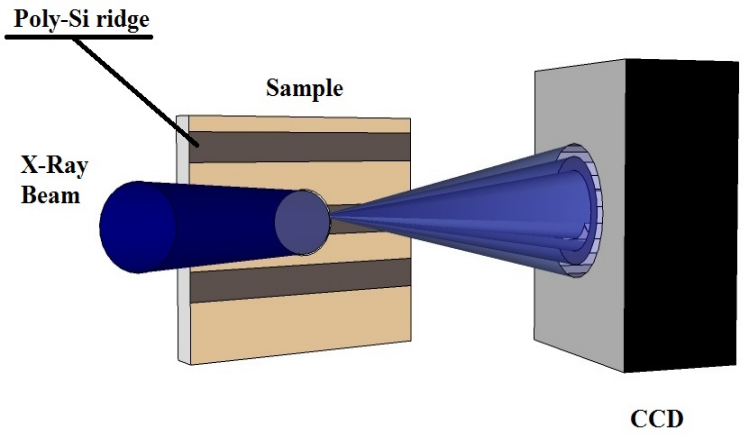

Figure 4.12: X-ray diffraction set up for grazing incidence

We will discuss the results from a sample of a-Si/LN deposited by HWCVD for a fixed speed of $7mm/min$ after Secco etching, since has been demonstrated to have the best crystallization according to Raman results; the irradiation power was varied as already mentioned in the previous sections.

In Figure 4.13 three diffraction patterns of different ridges made by laser annealing with different powers at similar speed $7mm/min$ are shown. On each pattern, Debye rings corresponding to crystal planes of Si in yellow and LN in dashed red are plotted [29, 30].

Figure 4.13 (a) shows a diffraction pattern from a ridge made by $50mW$. In this diffraction pattern we observe many spots along the LN rings. These spots show up because the surface could be damaged at this position due to the high power and the LN crystal substrate appears. Nano-crystals of silicon are spotted along the three first rings of silicon, this is assumed because continuous bright rings are present. This explain a low crystallization quality in the ridge which is in agreement with the Raman data presented in the previous section.

In the case of the diffraction pattern for the ridges made at $40mW$ shown at (b) in Figure 4.13), the diffracted pattern corresponds to the best crystallization according to Raman results. Only few spots were formed along the LN define circles but less than the ones found in (a). Nano-crystals of silicon appear along the three first Si crystal planes and one bright spot in the forth ring. This bright spot indicates one crystal plane with the orientation of

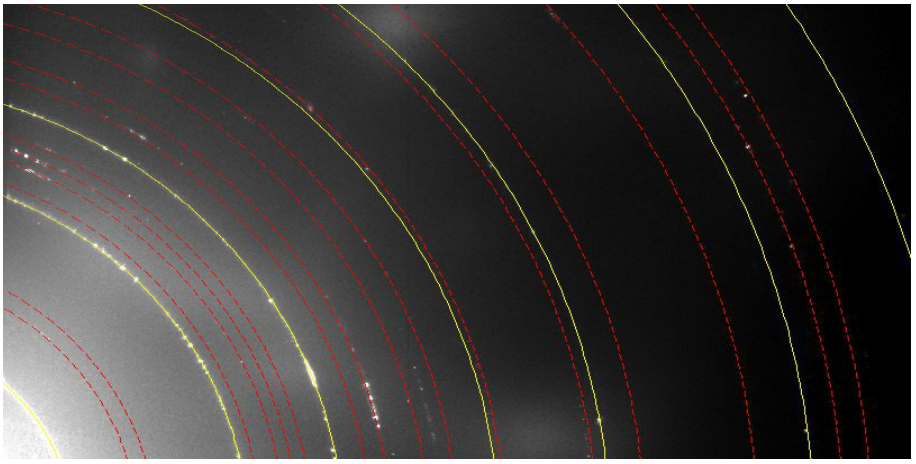

(a)

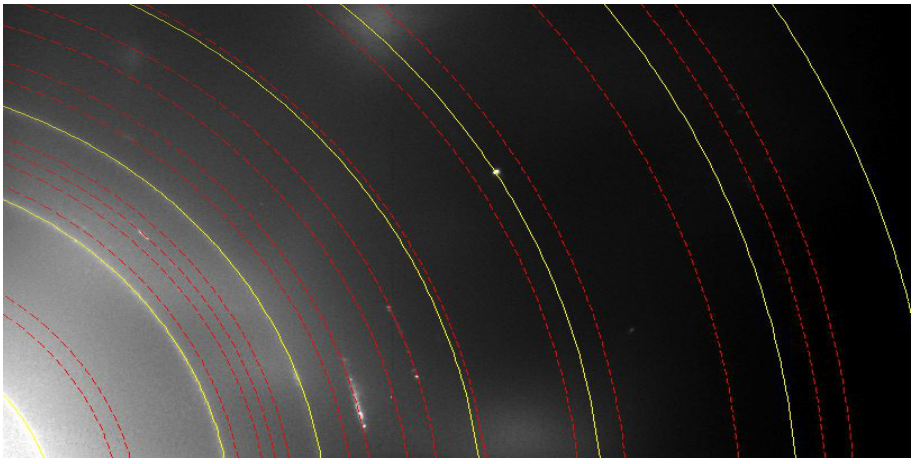

(b)

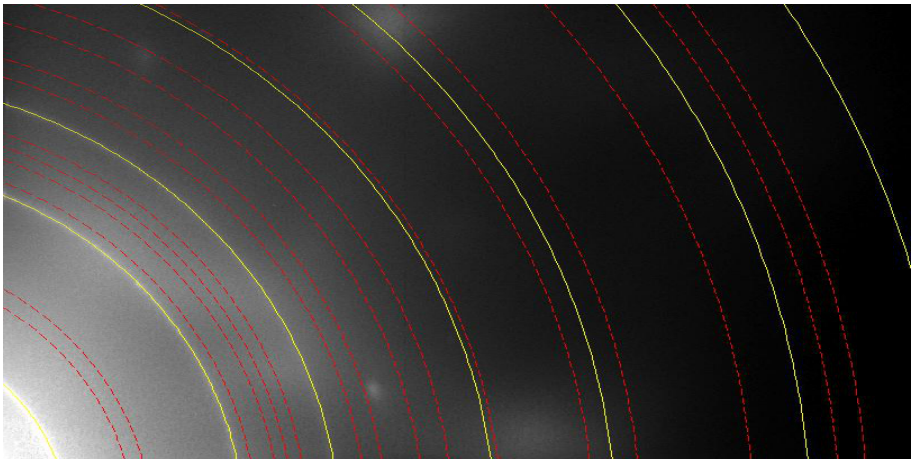

(c)

Figure 4.13: XRD patterns with reference crystal Debye rings for ridges made with $7mm/min$ at different powers. Rings in yellow corresponds to c-SI planes, dashed red rings corresponding to must relevant c-LN. (a)$50mW$ (b)$40mW$ (c)$30mW$

$< 400 >$; this spot appear in all the patters through the $10\mu m$ lateral scanning of this ridge.

Figure 4.13 (c) shows a lower crystallization with no individual diffraction spots along the LN diffraction rings corresponding to power annealing of $30mW$. Nanocrystals of silicon appear along the three first silicon rings: this corresponds to a low quality crystallization of the ridge as was noted from Raman data.

XRD confirms the existence of crystals on the ridges with the best conditions achieved in the samples of a-Si/LN at $40mW$ and $7mm/min$. These studies corroborate the Raman investigation presented in the past section.

Some recommendations to improve the adhesion between this two materials could be suggested. The first is depositing a thin layer of silica before the a-Si layer; this will have a structure a like the a-Si/Sc-Si samples and we expect a similar behaviour. Other options could include pre patterning a-Si ridges by other method as photolitography and RIE [16].

4.2.4.2 Laser processing of a-Si/LN pre patterned ridges

Good quality crystallization of a-Si by laser writing in planar structures is possible. An adhesion problem between crystallized silicon and LN has been found and reported in [28], making difficult to keep the ridges on the substrate during the processing steps. A sketch of the technique proposed is illustrated in Figure 4.14.

Using photolitography developed in [31] a set of ridges with different widths from $10\mu m$ to $4\mu m$ were fabricated over the surface of a-Si/LN. Later, using ion reactive etching [3], the exposed a-Si was removed to obtain ridges of $400nm$ high of a-Si/LN as seen in Figure 4.15 (a). These a-Si ridges were laser annealed with a lower magnification microscope objective to irradiate with the whole width of the ridge structure. The microscope objective used was a 10x objective producing $\sim 2.25\mu m$ spot size. Raman studies were performed on these ridges after laser annealing. The narrower FWHM observed was of $3.1cm^{-1}$ using $125mW$ at $7mm/min$: the intensity calculated for this conditions was about $1.57MW/cm^2$, which is in the range of intensities used to crystallized a-Si on LN. In Figure 4.15 we can observe the ridge before and

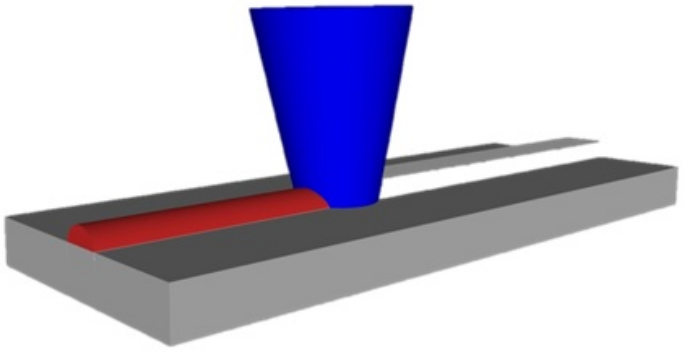

Figure 4.14: Sketch of laser annealing of an a-Si pre patterned ridge waveguide in LN.

after laser annealing. Here we see a reshaping of the surface of the ridge. However since the width of the ridge was about the same as the beam diameter, the ridge was not heated uniformly as shown in Figure 4.15 (b). Smaller ridges are required for uniform crystallisation using this method.

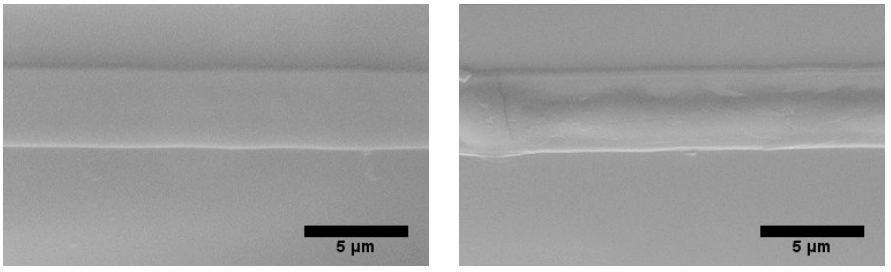

(a) (b)

Figure 4.15: SEM pictures of a-Si/LN patterning ridges. (a) Non annealed ridge (b) Same ridge after laser irradiation.

E-beam patterning has the potential to produce smaller ridges which could match in a better manner with the beam diameter. This has proven success in a-Si/Sc-Si samples. Good results for laser crystallization on pre patterned a-Si ridges on silica on c-Si were found in a different research inside our group and we plan to extend this to a-Si/LN in the future. Even when better crystallization and lower transmission losses has been achieved this technique has the disadvantage to required a pre patterned structure, but it could be a good solution for the integration with other materials.

We have shown that this method is suitable for the fabrication of crystallised poly-Si ridges in different substrates. The best results at a glance are the ridges formed at a-Si/Sc-Si. These samples where the last material in the research to be characterized so loss measurements where not performed, however as this technique has been proved for a-Si/SG, similar results can be expected.

4.3 Conclusions

To conclude, ridge silicon waveguides produced by laser annealing have been demonstrated on a silica glass substrate, transmission measurements were shown demonstrating a fast and cheap method to fabricate optical circuits compared with the methods available until today. Local laser crystallization on a-Si in different substrates with an a-Si layer were fabricated, making this method a great way to produce optical waveguides by crystallizing a poor quality a-Si layer. It should be noted that the deposition and etching methods are useful and compatible with other substrates where optical circuits could be implemented. Even when the loss transmission was of $9.3dB/cm$ and diverse manufacturing techniques claim lower losses, there exist potential for this method to increase the transmission; since better crystallization corresponded to better transmission and larger crystal sizes, and double annealing had proven a rise in the crystallization of the already developed waveguides, then re annealing the surface of the ridges could reduce the losses through all of the optical circuits.

Some other experiments were performed during this research like optical transmission losses for waveguides found underneath the silicon ridges inside lithium niobate, a first attempt to recrystallizing patterned ridges, laser annealing of a-Si for removable gratings on a-Si substrates, laser crystallization of a thin layer of amorphous lithium niobate using the good absorption of crystal silicon at $\lambda = 488nm$. All these investigations will be presented and analyzed in the next chapter.

References

[1] S. Tachi, K. Tsujimoto, and S. Okudaira, "Lowtemperature reactive ion etching and microwave plasma etching of silicon," *Applied Physics Letters*, vol. 52, no. 8, pp. 616–618, 1988.

[2] C. Steinbrüchel, H. Lehmann, and K. Frick, "Mechanism of dry etching of silicon dioxide a case of direct reactive ion etching," *Journal of The Electrochemical Society*, vol. 132, no. 1, pp. 180–186, 1985.

[3] S. Tachi, K. Tsujimoto, and S. Okudaira, "Lowtemperature reactive ion etching and microwave plasma etching of silicon," *Applied Physics Letters*, vol. 52, no. 8, pp. 616–618, 1988.

[4] N. Chekurov, K. Grigoras, A. Peltonen, S. Franssila, and Tittonen, "The fabrication of silicon nanostructures by local gallium implantation and cryogenic deep reactive ion etching," *Nanotechnology*, vol. 20, no. 6, p. 065307, 2009.

[5] T. Corman, P. Enoksson, and G. Stemme, "Deep wet etching of borosilicate glass using an anodically bonded silicon substrate as mask," *Journal of Micromechanics and Microengineering*, vol. 8, no. 2, p. 84, 1998.

[6] E. Vazsonyi, K. D. Clercq, R. Einhaus, E. V. Kerschaver, K. Said, J. Poortmans, J. Szlufcik, and J. Nijs, "Improved anisotropic etching process for industrial texturing of silicon solar cells," *Solar Energy Materials and Solar Cells*, vol. 57, no. 2, pp. 179 – 188, 1999.

[7] D. Zhuang and J. Edgar, "Wet etching of Ga N, Al N, and Si C: a review," *Materials Science and Engineering: R: Reports*, vol. 48, no. 1, pp. 1–46, 2005.

[8] W. Kern, "The evolution of silicon wafer cleaning technology," *Journal of the Electrochemical Society*, vol. 137, no. 6, pp. 1887–1892, 1990.

[9] P. Sievilä, N. Chekurov, and I. Tittonen, "The fabrication of silicon nanostructures by focused-ion-beam implantation and tmah wet etching," *Nanotechnology*, vol. 21, no. 14, p. 145301, 2010.

[10] C. Eijkel, J. Branebjerg, M. Elwenspoek, and F. Van de Pol, "A new technology for micromachining of silicon: dopant selective hf anodic etching for the realization of low-doped monocrystalline silicon structures," *IEEE electron device letters*, vol. 11, no. 12, pp. 588–589, 1990.

[11] B. Schmidt, L. Bischoff, and J. Teichert, "Writing {FIB} implantation and subsequent anisotropic wet chemical etching for fabrication of 3d structures in silicon," *Sensors and Actuators A: Physical*, vol. 61, no. 13, pp. 369 – 373, 1997. Proceedings of {EUROSENSORS} X.

[12] A. Abbadie, J.-M. Hartmann, and F. Brunier, "A review of different and promising defect etching techniques: From si to ge," *ECS Transactions*, vol. 10, no. 1, pp. 3–19, 2007.

[13] F. S. d'Aragona, "Dislocation etch for (100) planes in silicon," *Journal of The Electrochemical Society*, vol. 119, no. 7, pp. 948–951, 1972.

[14] M. W. Jenkins, "A new preferential etch for defects in silicon crystals," *Journal of The Electrochemical Society*, vol. 124, no. 5, pp. 757–762, 1977.

[15] J. Jin, Z. Yuan, L. Huang, S. Chen, W. Shi, Z. Cao, and Q. Lou, "Laser crystallization of amorphous silicon films investigated by raman spectroscopy and atomic force microscopy," *Applied Surface Science*, vol. 256, no. 11, pp. 3453 – 3458, 2010.

[16] A. Harke, M. Krause, and J. Mueller, "Low-loss singlemode amorphous silicon waveguides," *Electronics Letters*, vol. 41, no. 25, p. 1377 1379, 2005.

[17] S. K. Selvaraja, E. Sleeckx, M. Schaekers, W. Bogaerts, D. V. Thourhout, P. Dumon, and R. Baets, "Low-loss amorphous silicon-on-insulator technology for photonic integrated circuitry," *Optics Communications*, vol. 282, no. 9, pp. 1767 – 1770, 2009.

[18] N. Greenwood and A. Earnshaw, *Chemistry of Elements*. Oxford.

[19] P. Dumon, G. Priem, L. R. Nunes, W. Bogaerts, D. Van Thourhout, P. Bienstman, T. K. Liang, M. Tsuchiya, P. Jaenen, S. Beckx, *et al.*, "Linear and nonlinear nanophotonic devices based on silicon-on-insulator wire waveguides," *Japanese journal of applied physics*, vol. 45, no. 8S, p. 6589, 2006.

[20] B. Schmidt, Q. Xu, J. Shakya, S. Manipatruni, and M. Lipson, "Compact electro-optic modulator on silicon-on-insulator substrates using cavities with ultra-small modal volumes," *Optics Express*, vol. 15, no. 6, pp. 3140–3148, 2007.

[21] Z. Sheng, D. Dai, and S. He, "Improve channel uniformity of an si-nanowire awg demultiplexer by using dual-tapered auxiliary waveguides," *Journal of Lightwave Technology*, vol. 25, no. 10, pp. 3001–3007, 2007.

[22] F. Xia, L. Sekaric, and Y. Vlasov, "Ultracompact optical buffers on a silicon chip," *Nature photonics*, vol. 1, no. 1, pp. 65–71, 2007.

[23] K. P. Yap, A. Delage, J. Lapointe, B. Lamontagne, J. H. Schmid, P. Waldron, B. A. Syrett, and S. Janz, "Correlation of scattering loss, sidewall roughness and waveguide width in silicon-on-insulator (soi) ridge waveguides," *Journal of Lightwave Technology*, vol. 27, pp. 3999–4008, Sept 2009.

[24] Y. Yamada, A. Takagi, I. Ogawa, M. Kawachi, and M. Kobayashi, "Silica-based optical waveguide on terraced silicon substrate as hybrid integration platform," *Electronics Letters*, vol. 29, no. 5, p. 444 446, 1993.

[25] R. Soref and J. Larenzo, "All-silicon active and passive guided-wave components for $\lambda = 1.3$ and $1.6\mu m$," *IEEE Journal of Quantum Electronics*, vol. 22, pp. 873–879, Jun 1986.

[26] A. Splett, J. Schmidtchen, B. Schuppert, K. Petermann, E. Kasper, and H. Kibbel, "Low loss optical rigde waveguides in a strained gesi epitaxial layer grown on silicon," *Electronics Letters*, vol. 26, pp. 1035–1037, July 1990.

[27] L. Liao, *Low loss polysilicon waveguides for silicon photonics*. PhD thesis, Massachusetts Institute of Technology, 1997.

[28] M. Howlader, T. Suga, and M. Kim, "Room temperature bonding of silicon and lithium niobate," *Applied physics letters*, vol. 89, no. 3, p. 031914, 2006.

[29] C. R. Hubbard, H. t. Swanson, and F. Mauer, "A silicon powder diffraction standard reference material," *Journal of Applied Crystallography*, vol. 8, no. 1, pp. 45–48, 1975.

[30] H. E. Swanson, E. Tatge, and R. K. Fuyat, *Standard X-ray diffraction powder patterns*. US Government Printing Office, 1953.

[31] J.aeger and C. Richard, *Lithography, Introduction to Microelectonic Fabrication*, vol. 1. Upper Saddle River: Prentice Hall, 2nd ed., 2002.

Chapter 5

Laser processing of a-Si in a crystalline matrix and other intermediate results

5.1 Introduction

This chapter will cover experiments related to laser processing performed during the course of this research. This work consist of intermediate results that are of relevance to the laser crystallisation process on different substrates (as waveguides found underneath the silicon ridges inside lithium niobate, a-Si gratings removed by laser irradiation, and, laser crystallization of amorphous lithium niobate on c-Si substrates).

5.2 Laser annealing of a-Si gratings on Silica substrate

Among the studies that have been presented in the previous chapters some other experiments have been performed in a collaboration with the Si photonics group at the ORC. The most relevant will be introduced here.

Grating couplers were first demonstrated by Dakss et al [1]. They offer the ability to couple light in to or out from any location on the device

without the need for polishing, thus making them a good candidate for an optical test point. The possibility of fabricating grating structures which can be individually erased opens new possibilities in the world of silicon photonics, specifically in the area of optical testing, which requires a minimally intrusive technology [2].

Implanted diffractive gratings of $15\mu m$ length and $15\mu m$ width were made using the method followed in [3]. These gratings are formed by periodic regions of amorphous and crystalline silicon deposited on a SiO_2 substrate (See Figure 5.1). They were patterned to create a modulated effective index due to differing refractive indices of each allotrope. This is because the a-Si regions exhibit a lower index of refraction compared with c-Si regions.

Figure 5.1: Sketch of an implanted diffractive grating coupler.

To erase the implanted grating coupler laser exposure was performed, working on the same set up for laser writing (See Figure 2.1). Using a cw $488nm$ laser with a beam waist of $2.2\mu m$ the gratings were totally scanned across their width with a separation between adjacent scans set to $0.5\mu m$, such that there was an overlap between successive scans. This overlap ensures uniform melting of the surface by the Gaussian shaped beam. Different powers, from $300mW$ to $100mW$, corresponding to intensities of $3.7MW/cm^2$ to $1.25MW/cm^2$, and different speeds from $.01mm/min$ to $5mm/min$ were tested pursuing the best conditions for erase the grating without damaging the surface of the photonic device. By this method was possible to remove the implanted gratings selectively using the best conditions of $180mW$ or $2.26MW/cm^2$ at $0.5mm/min$.

In Figure 5.2 we observe in the same photonic device three different conditions of the laser writing. At the right section the grating was not annealed, in the middle section the laser writing conditions (speed and power) were able to remove completely the grating without damaging the surface and finally at the left section the surface was melted due to a higher power of the laser annealing.

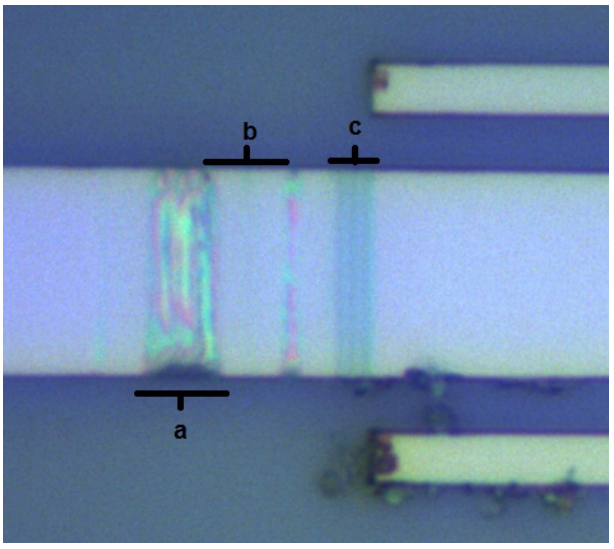

Figure 5.2: Optical Microscope picture of a photonic device with a grating. Here we can observe in the same device three different conditions: (a) at the left the melted surface produced by laser writing due a higher power irradiation, (b) in the middle the grating was erased by laser annealing and (c) at the right a grating not irradiated.

The erasable gratings were tested by the Si photonics group using a very particular manner. Using only a direct measurements would require measuring an absence of light if the grating coupler was erased successfully. But absence of light could be caused by operator errors such as reduced alignment accuracy, a shift of the operational wavelength of the grating coupler or coupling the power to other leaky modes due to a refractive index change. Thus characterising the output of an erasable grating coupler to show the performance of the device before and after annealing would be a very crude measure of the erasability. For this reason the concept of a bow tie structure was introduced as shown in Figure 5.3. This structure allows the erasable grating to be considered as a three part device.

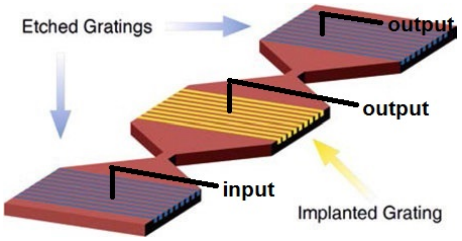

Figure 5.3: Bow tie silicon waveguide structure for characterising erasable gratings. The end coupling regions represent surface relief gratings, the middle grating region represents an erasable implanted coupler.

The optical characterisation of the bow tie structures can be performed for the case of: (i) coupling into a conventional etched grating coupler and out coupling through the implanted grating coupler and (ii) coupling from one conventional etched grating (input) to the other (output). A successfully erased device will show both a substantial decrease in the optical power in the etched grating to implanted grating transmission (case i), and an increase in optical power in the etched grating to etched grating transmission (case ii), when compared with pre-annealed measurements.

Firstly the implanted grating performance before laser annealing was measured, followed by measuring the performance after the grating anneal. The results of these measurements are shown in a graph at Figure 5.4. Here we can observe that the transmission loss decrease after the annealing.

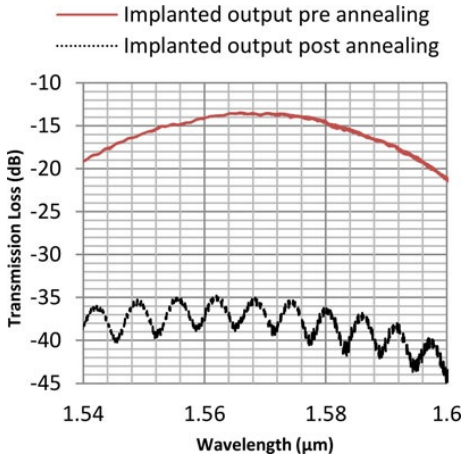

Figure 5.4: Coupling in the grating before and after laser annealing.

Then it is important to demonstrate that transmission through the annealed region has increased, by measuring the throughput of the device before and after annealing. These results are shown in Figure 5.5, where the transmission loss increase after the annealing as was expected. The results have been normalised to a standard transmission measurement of the optical setup, which excludes the device under test.

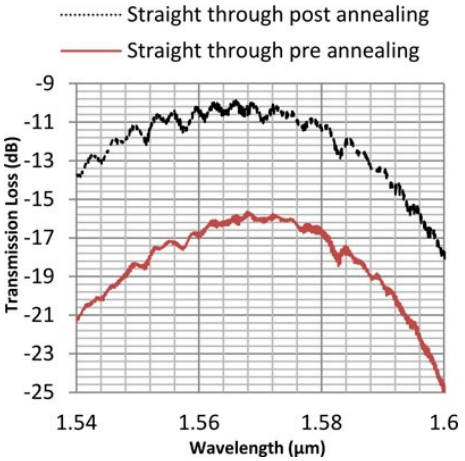

Figure 5.5: Performace of end to end cuopling before and after laser annealing.

This testing method results in a waveguide with an unperturbed surface, and an optical circuit that is not impeded by the erased test point. After laser annealing the performance of the implanted grating decreases by $21dB$, while the transmission through the annealed regions increases by $5.7dB$ when compared with the grating transmission performance before annealing. These results suggest that this is a very powerful wafer scale testing method that will directly enable an increased yield of optical integrated circuits when fabricating complex photonic designs.

5.3 Laser-induced waveguide formation in LN

LN crystals play an important role as a source material for optical devices due to their mechanical robustness, good availability, optical homogeneity, and advantageous ferroelectric, electro-optic, and photorefractive properties [4, 5]. Integrated optics with lasers, modulators,and filters on a single LiNbO3 wafer have been fabricated with excellent results [6, 7, 8, 9, 10]. This is why is imperative to find new methods to integrated LN as optical waveguides with other optical materials as Si to be able to guide, control, and modify the light in one optical circuit. High quality LN embedded waveguides have been fabricated by proton exchange [11] , also by Lithium Diffusion as a result of the laser heating absorved from a UV source [12, 13] and diffusion of titanium [14, 15]. These techniques enhance the refractive index in the surface of LN and thus enable the guiding of light between the surface and the substrate.

Proton exchange in Lithium Niobate involves a replacement of Lithium ions (Li+) by hydrogen ions, or protons (H+). This replacement causes a change in the refractive index of the treated area. This method for fabricating LN waveguides is a low-temperature process ($120°C250°C$) whereby Li ions from the LN substrate are exchanged with protons from an acid bath usually benzonic acid [16, 17, 11].

Laser Lithium diffusion it is a method where an continuous UV laser is focused on LN, through direct writing, creating LN waveguides in the irradiated area. It is proposed that the UV illumination induces heating of the surface and subsequent thermal diffusion of lithium alters the refractive index[13].

During the research presented in this thesis a method to produce embedded LN waveguides was found. These waveguides were found underneath the laser annealed a-Si deposited on the LN substrate. This technique not just makes optical waveguides, it also provides a poly silicon ridge over the circuit increasing the properties of the devices that could be produced.

Laser irradiated tracks were written on the a-Si/LN samples using the optimum Si crystallization conditions, as well for those with pearl chain lines. After polishing the edges, polarized (TE and TM) light of a He-Ne laser with wavelengths of $633nm$ and at $1523nm$ was injected through the sample and the output signal intensity from each written line was collected. Light guiding was found inside LN, as optical waveguides were formed below the laser irradiated tracks. Figure 5.6 shows an sketch of the embedded waveguides under the laser written tracks.

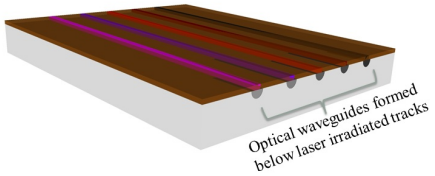

Figure 5.6: Optical waveguides in LN formed below laser irradiated tracks.

The formation of this waveguides inside lithium niobate is attributed to proton exchange or lithium diffusion by temperature change.

In this case protons from the a-Si layer could be interchange for lithium ions due to the laser irradiation, producing this change in the index of refraction.

However since the source is a continuous laser and the heat is enough to melt the a-Si deposited in LN, this heat could be enough to produce diffusion of lithium atoms as in the case of [12, 13]. In Figure 5.7 a sketch of process formation of LN waveguides. First the heat is absorbed by the a-Si layer and transmitted to the LN substrate: this makes lithium diffusion locally underneath the laser crystallized a-Si, producing a change in the refractive index of LN and forms a waveguide.

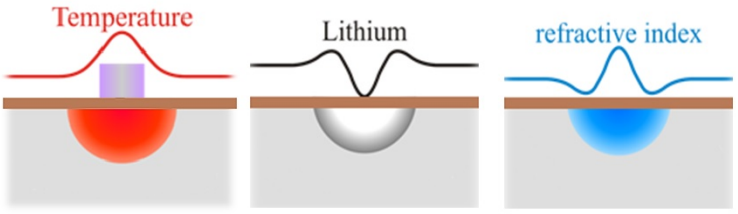

Figure 5.7: Representation of the formation of LN waveguides underneath a-Si irradiated tracks.

The results of TM polarization testing in the LN waveguides written with different speeds, $5mm/min$, $7mm/min$ and $10mm/min$ are shown in Figure 5.8. For all the profiles, the surface of amorphous silicon is oriented to the top of the picture. Also to make a connection to the degree of crystallization of the amorphous silicon at the surface, the Lorentzian fitted widths from Raman spectrometer analysis are shown for each profile. We recall from the precedent section that the pearl chain lines appear in the power range between $25mW$ and $30mW$, so the last profiles correspond to these pearl chains.

In Figure 5.8 the intensity profiles of LN waveguides, underneath the crystallized a-Si layer, written with a speed of $5mm/min$ for different powers are shown. We observe that all the profiles have a size of the order of $10\mu m$, also as the power is getting lower the number of propagating modes inside the waveguides decreases. Finally we can notice that the best crystallization is achieved in (c).

In Figure 5.9 the intensity profiles of waveguides written with a speed of 7mm/min for different powers are shown. Here again the size of tens of μm is conserved and also as the power is getting lower the mode inside the waveguides become single mode. The best crystallization for the a-Si is in (c).

In Figure 5.10 the intensity profiles of waveguides written with a speed of $10mm/min$ for different powers are shown. For the last two pictures (e) and (f) we observe that the modes become diffuse, probably because of the fact

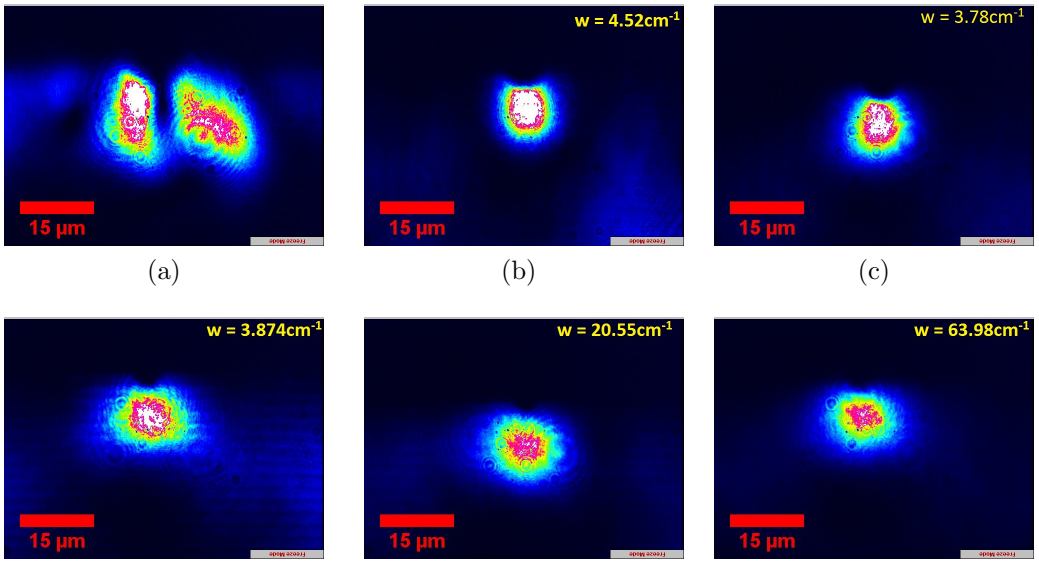

(a) (b) (c)

(d) (e) (f)

Figure 5.8: Profiles of LN waveguides for $\lambda = 633nm$, due to crystallization of the a-Si film, with corresponding widths from Raman spectroscpy analysis. Different Powers on writing with $\lambda = 488nm$ and same speed of 5mm/min (a)55mW, (b)45mW, (c)40mW, (d)35mW, (e)30mW, (f)25mW

that these two waveguides were written with the lowest powers and the fastest speed, so that the energy absorbed was lower as compared to other waveguides.

It was not possible to couple IR light to all the different waveguides. The best intensity profiles acquired for Infra Red (IR) Laser at $\lambda = 1523nm$ for the same waveguides used before are presented in Figure 5.11: (a) and (b) show the intensity profiles of a waveguides written at $5mm/min$ using $55mW$ and $45mW$, (c), (d) and (e) show profiles for waveguides written at $7mm/min$ using $55mW$, $50W$ and $50mW$, (f) shows a profile for a waveguide written at $10mm/min$ using $45mW$, all of them are single mode and well defined. From all the presented modes we can notice that the most defined is the figure (e) which corresponds to the conditions of $40mW$ at $7mm/min$: these conditions are also associated to the best crystallisation of the tracks according to Raman studies.

The waveguide intensity profiles for visible have a size of micrometers and the infra-red have a size of tens of micrometers, both of them are well defined propagation modes. We observed that for all the waveguides, as the intensity used in the writing was lowered the number of modes was decreased. This process has proved to be a new method in the fabrication of embedded

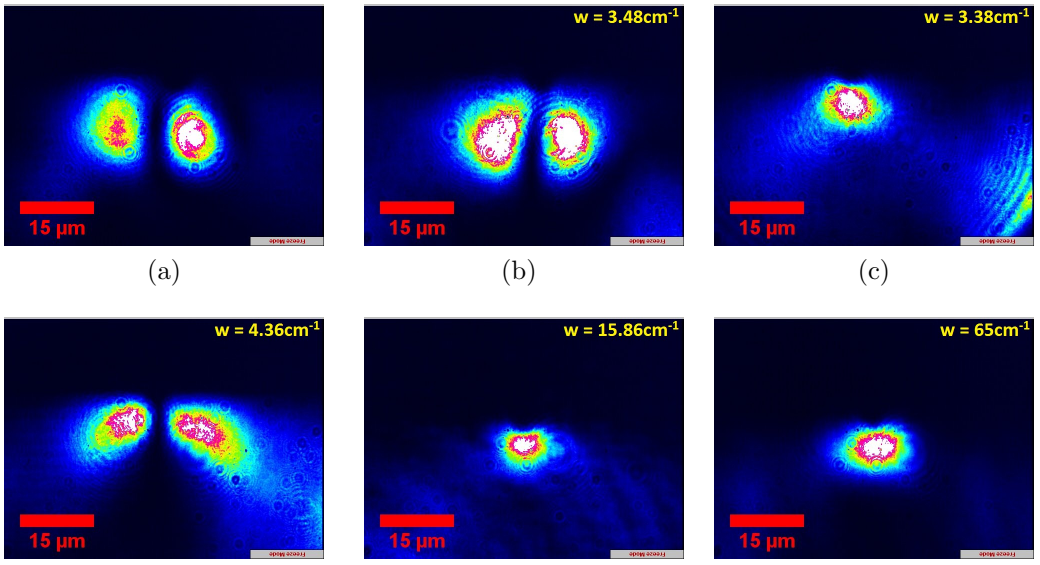

(a) (b) (c)

(d) (e) (f)

Figure 5.9: Profiles of LN waveguides on a-Si/LN; Different Powers on writing with 488nm and same speed of 7mm/min (a)55mW, (b)45mW, (c)40mW, (d)35mW, (e)30mW, (f)25mW

optical waveguides for visible and IR in lithium niobate.

Transmission loss measurements

Transmission loss studies for these waveguides have been performed using the cutback technique. The intensity was measured for each individual waveguide, then the whole sample was polished again removing $1mm$ from one of the edges and the intensity for each waveguide was remeasured. This method was follow another 4 times in order to determine the loss in the transmission of the waveguide in the same manner as the silicon ridges. Finding the lowest loss to be $4.54dB/cm$ for the case of $40mW$ at $7mm/min$. This method makes a great alternative to produce in an easy way embedded LN waveguides.

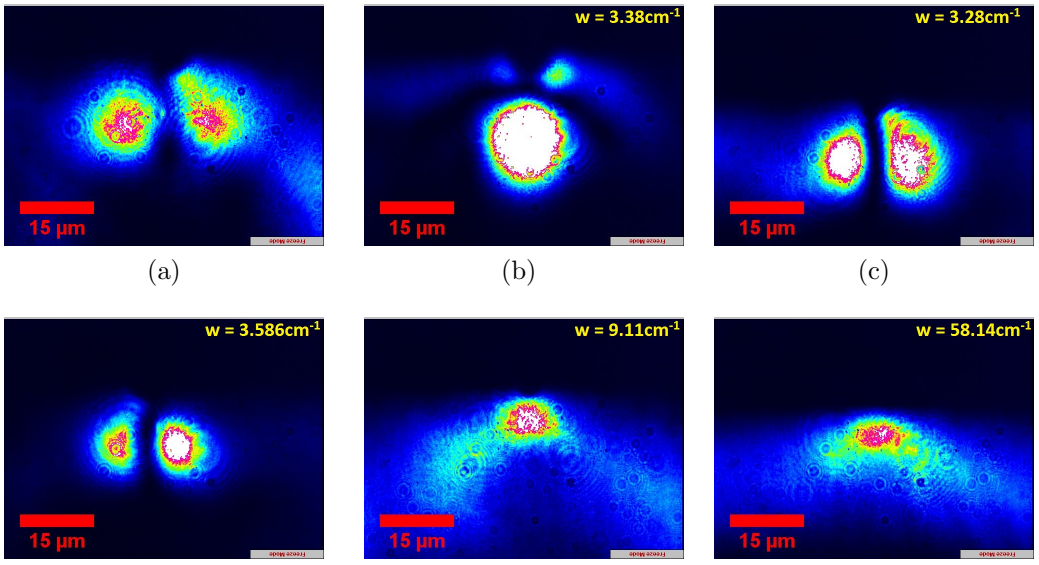

Figure 5.10: Profiles of LN waveguides on a-Si/LN; Different Powers on writing with 488nm and same speed of 10mm/min 9a)55mW, (b)45mW, (c)40mW, (d)35mW, (e)30mW, (f)25mW

5.4 Laser annealing of amorphous LN/c-Si

Silicon is a good absorber at visible wavelength ($488nm$,$514.5nm$). This gave the idea to use the heat transfer with the purpose to recrystallize other materials not absorbing at visible wavelengths deposited on top of Si. A film of amorphous lithium niobate deposited by CVD with a thickness of $120nm$ on a substrate of crystalline silicon (a-LN/c-si) was fabricated by 3D-oxides. The deposition was performed by placing the c-Si substrate into a reactor, on a heated holder. The precursor gases used in the deposition were lithium t-butoxide and niobium ethoxide. These gasses had to be kept at $190°C$ and $150°C$, respectively during all the deposition process. A carrier gas of 23% oxygen and 77% nitrogen was bubbled through the precursors at a flow rate of $\sim 0.5slpm$. Growth of amorphous films was typically carried out at a substrate temperature of $\sim 650°C$. Films grown over the temperature range of $500°C$ to $700°C$ [18].

Laser irradiated tracks, $2mm$ long, were laser inscribed with a CW visible multi-line Argon ion Laser with two main wavelengths at $488nm$ and $514.5nm$ on the surface of a a-LN/c-Si sample using the same set up described in the past chapters. Using a $20X$ magnification, focussing the laser beam to a spot size of $1.5\mu m$ different powers were ranging from $700mW$ (corresponding

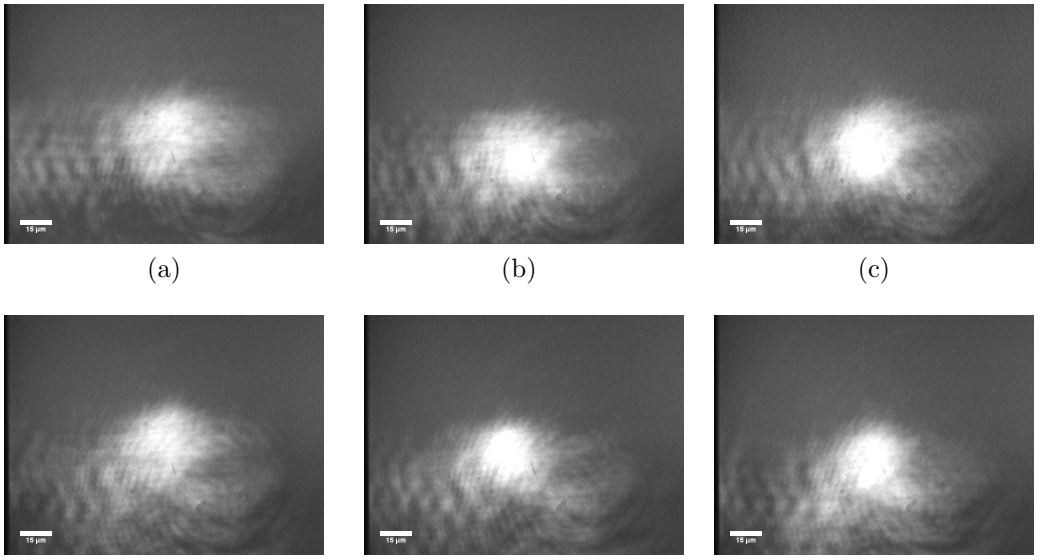

(a) (b) (c)

(d) (e) (f)

Figure 5.11: Near field mode profiles of embebded waveguides on a-Si/LN for 1523nm; Different Powers and speeds (a)55 mW at 5 mm/min, (b)45 mW at 5 mm/min, (c)55 mW at 7 mm/min, (d)50 mW at 7 mm/min, (e)40 mW at 7 mm/min, (f)45 mW at 10 mm/min

to an intensity of $19.8 MW/cm^2$), where the material was damaged at the surface, to $250mW$ with an intensity of $7.07 MW/cm^2$, where no visible change was observed on in the a-LN surface. The speed was also varied in the range of $1mm/min$ to $20mm/min$. We noticed that these intensities are greater than the ones used for a-Si/G and a-Si/LN because now the substrate is crystal silicon which has a better heat conductivity compared to the a-Si films that were used in previous experiments that were presented in this thesis.

In Figure 5.12 three tracks irradiated with different laser powers at a speed of $1mm/min$ are shown. In Figure 5.12 (a) where a power of $700mW$ was used, the surface becomes severely damaged after the laser exposure. In (b) where a power of $500mW$ was used a smooth and continuous track is observed and finally at (c) where a lower power of $300mW$ was used during the process the surface is almost unchanged. We worked mostly at a laser power around $500mW$ that was below the damage threshold and which was expected to produce high temperatures that would facilitate crystallization of a-LN.

Raman studies after laser irradiation were performed on these tracks to investigate the impact of the laser process on the original a-LN film. The Raman spectrometer used in this particular case was a Renishaw (comercial

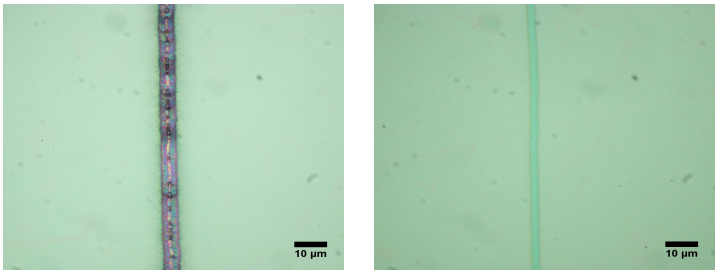

(a) (b)

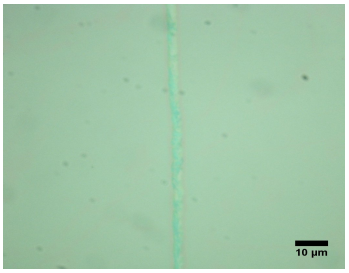

(c)

Figure 5.12: Optical microscope images of different tracks on a-LN/Si that were produced using laser powers: $1mm/min$ on a sample of a-LN/c-Si (a)700mW, (b)500mW, (c)300mW. The scanning speed was kept at $1mm/min$

Raman setup), using the smallest spot size available with an microscope objective of $100X$ and short wavelength of $473nm$. Figure 5.13 shows a sequence on Raman spectra, obtained from the original a-LN film, from crystalline lithium niobate reference, and from a laser-irradiated track. Due to the fact there was a c-Si substrate, a big contribution of this material was presented in all the spectra, for this reason they had to be cut before $521cm^{-1}$ to remove the silicon peak. We can notice there was a change in the spectra after the laser annealing noticing a resemble to the LN reference. However not all the peaks match to the reference but there was a change after annealing.

We will present Raman spectroscopy results obtained at a power of $550mW$ corresponding to and intensity of $15.56MW/cm^2$. These results correspond to the best laser-crystallisation conditions found so far. In Figure 5.14 Raman spectra for different laser scanning speeds are presented (a)1 mm/min (b)5 mm/min (c)10 mm/min (d)15 mm/min. For each spectrum the position of the peaks corresponding to c-LN are indicated and the silicon peak at $521cm^1$ was removed because it dominated the spectrum. Since different crystallography orientations of LN are possible after the laser treatment here we show the most common ones, X, Y and Z orientations. The corresponding

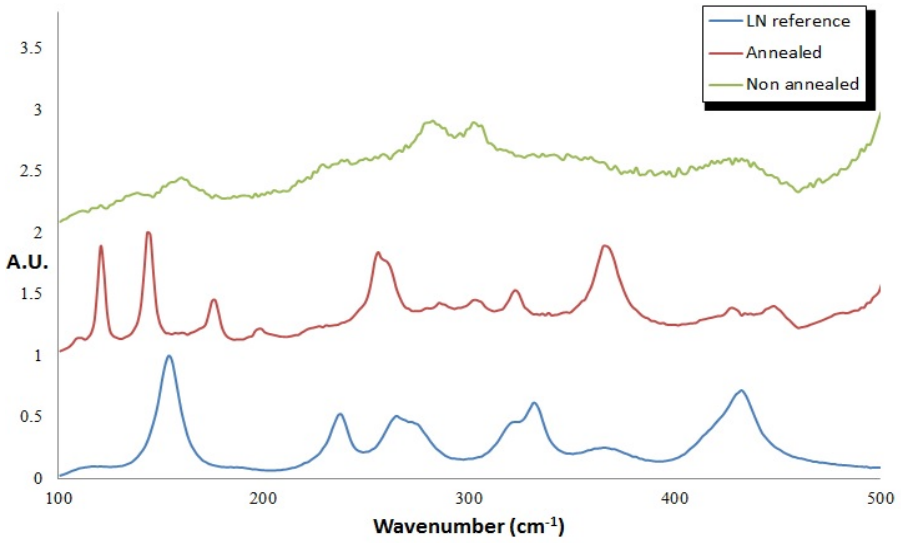

Figure 5.13: Comparative of Raman spectra, in blue a crystal LN reference, in green the surface of the samples as fabricated, in red surface of sample after laser annealing.

peaks are indicated in the spectra. The single crystal Raman peaks for LN are indicated by blue, green and red short lines corresponding to the Z, X and Y orientations respectively.

The spectrum that corresponds to the laser-crystallised track shows some of the crystalline Raman peaks for LN, which is an indication that LN crystals were formed as a result of the laser treatment. However there are also peaks that are unaccounted for: those could be attributed to strained LN crystals that produce spectrally shifted Raman lines, or other non-ferroelectric phases of LN that coexist in the laser treated film. Further investigations of the film was conducted using the micro-focus XRD at the Diamond light source. In all we found some peaks matching with the different crystal position pointers, demonstrating a change in the surface of the sample which resemble more to crystalline LN with Z cut, specially on (a).

Micro focus XRD measurements on the laser irradiated tracks were taken in similar manner as the ones of a-SI/LN, making use of the grazing incidence set up. Figure 5.15 shows the diffraction spectra corresponding to the non annealed part of the film. This pattern corresponds to a-LN as grown. The bright spot that could be observed on this spectrum corresponds to the Si crystal plane of $< 311 >$ originating in the substrate. This spot is present in all the diffraction patterns, taken from the same substrate. This bright diffraction

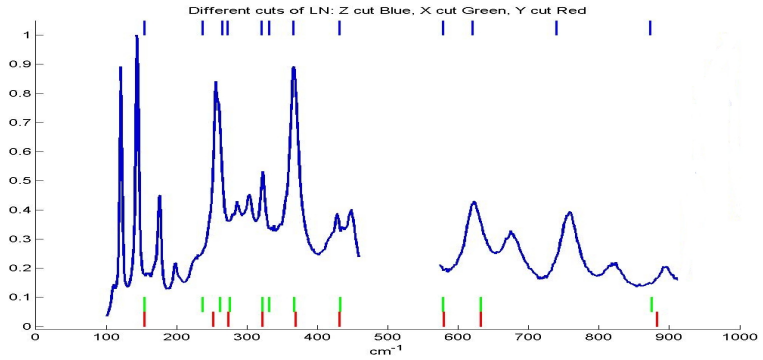

(a)

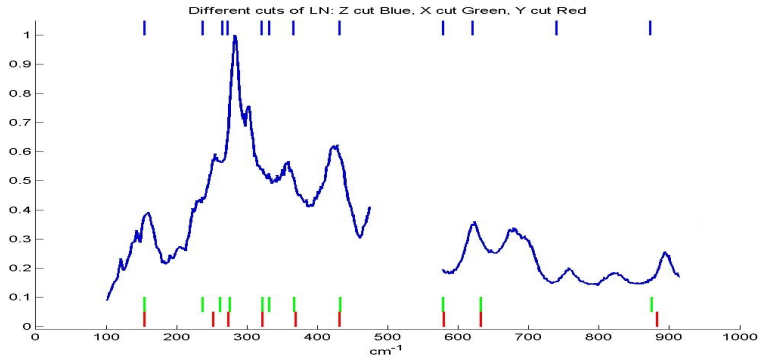

(b)

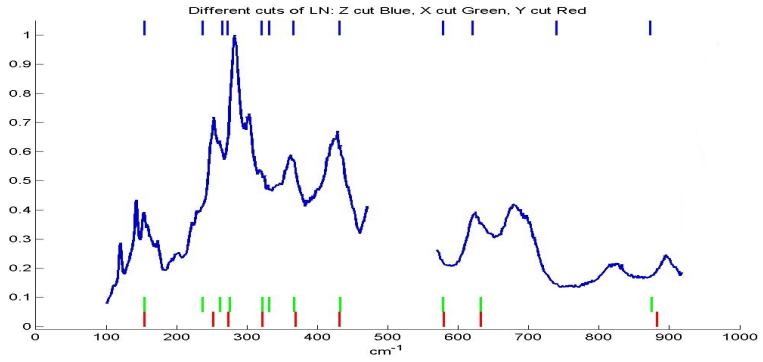

(c)

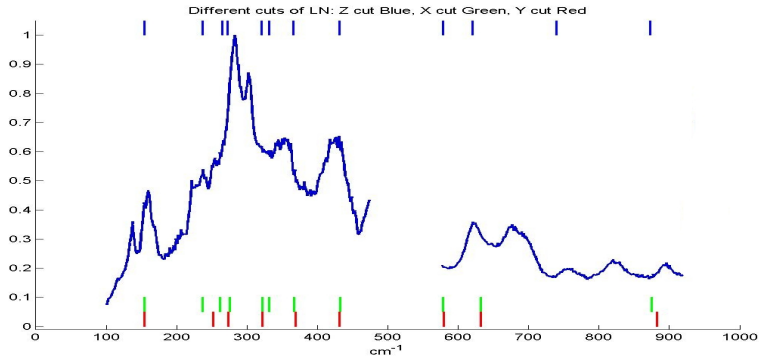

(d)

Figure 5.14: Raman data from lines made at $550mW$ for different speeds (a)1mm/min (b)5mm/min (c)10mm/min (d)15mm/min, for all of them small lines at top and bottom point the positions for c-LN peaks of the different cuts, Z cut blue, X cut green and Y cut red. Silicon peak was cut to highlight the contribution of LN

spot, from the substrate has been digitally removed from subsequent spectra, taken from the laser irradiated tracks to improve the visibility of the film's diffraction data.

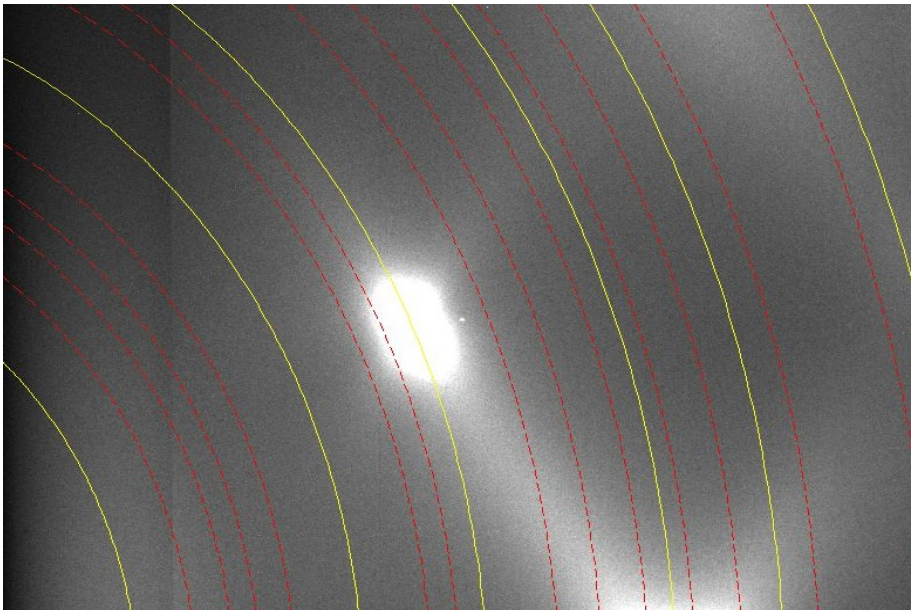

(a)

Figure 5.15: XRD spectrum from the as-grown a-LN film. Rings in yellow corresponds to c-SI planes, dashed red rings corresponding to c-LN (from database) The bright spot corresponds to diffraction from the c-Si substrate.

Diffraction patterns with the background reference removed from the same tracks of the same Raman data showed are presented in Figure 5.16. In all of them we can observe diffraction spots that match with the Debye ring sections corresponding to LN (red dashed) or Si (yellow). In (a) a very bright spot at the last LN ring is seen: this indicates the presence of a large crystalline LN. The images (c) and (d) show denser continuous diffraction signatures implying the formation of nano crystals over for the corresponding laser irradiation conditions.

In all the diffraction patterns we observe many coincidences between the LN Debye rings and the diffraction spots. We specially focus in the $8th$ ring which corresponds to LN with at crystal plane of $< 214 >$. Over this ring the azimuthal intensity profile was extracted for each image. The intensity for each spot is placed on a graph along the circumference in Figure 5.17. In (a) at Figure 5.17 we find a low level signature of LN crystals along the ring; in the same figure at (b) a very intense peak is spotted indicating a strong

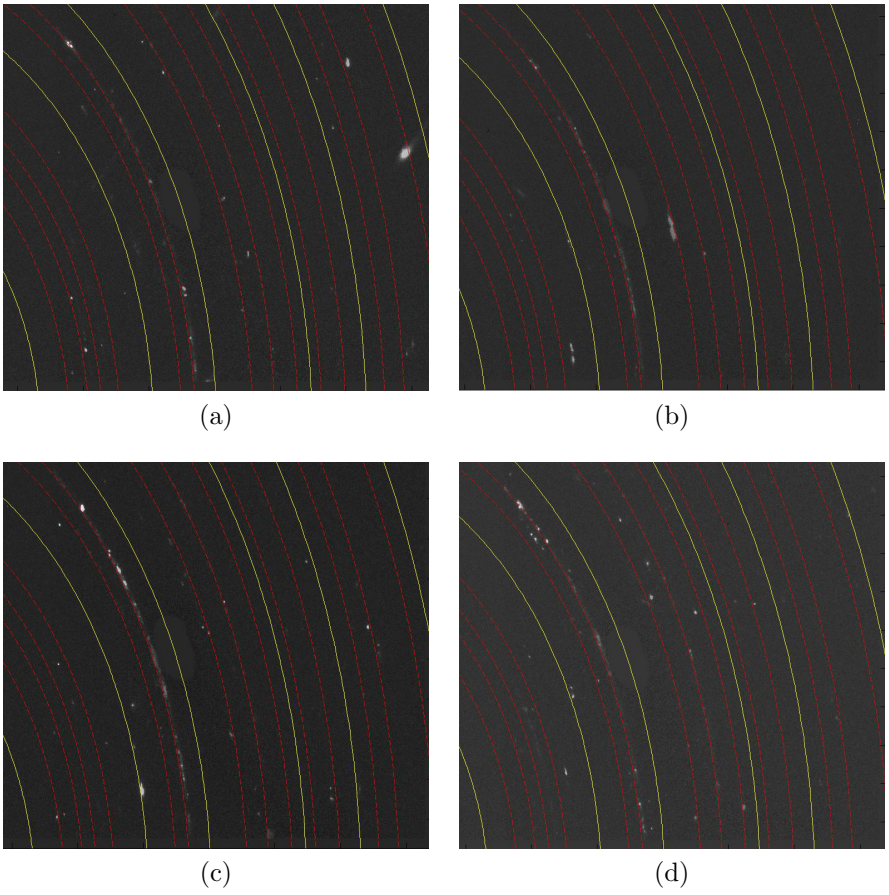

(a) (b) (c) (d)

Figure 5.16: X-Ray diffraction patterns for each line associated with Figure 5.14

contribution of one LN crystal in this crystal plane. In the case of (c) and (d) smaller peaks were found this is associated with LN nano-crystals.

All the the results presented above show structural change in the film. Both Raman and XRD studies points at the presence of crystallized material. Further work is needed to optimize the combination of growth and laser crystallisation conditions. This work is beyond the scope of this thesis.

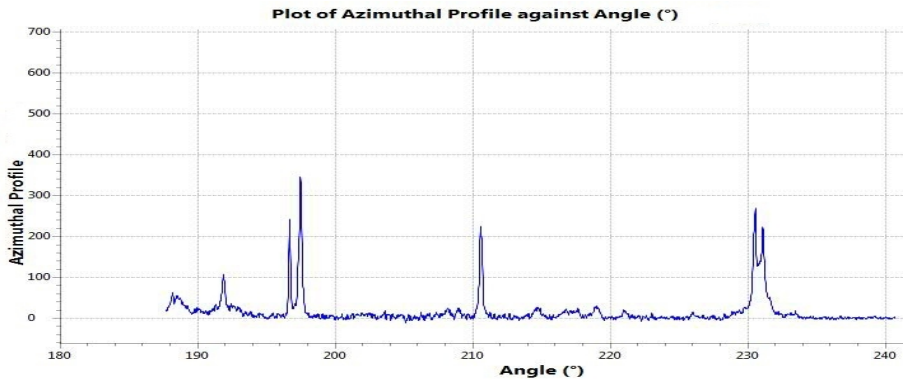

(a)

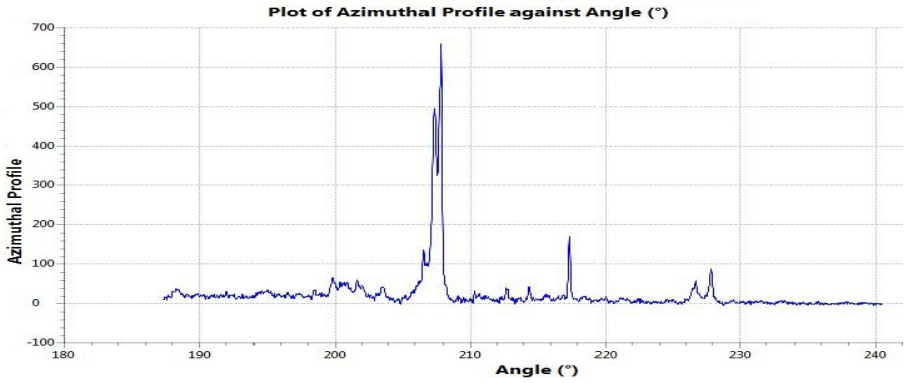

(b)

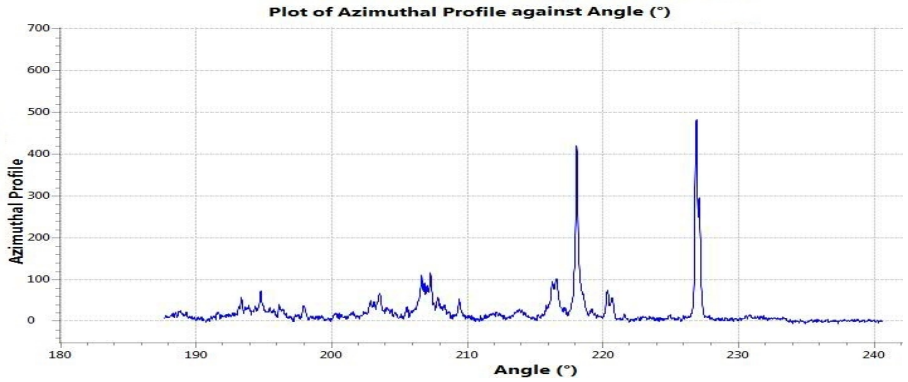

(c)

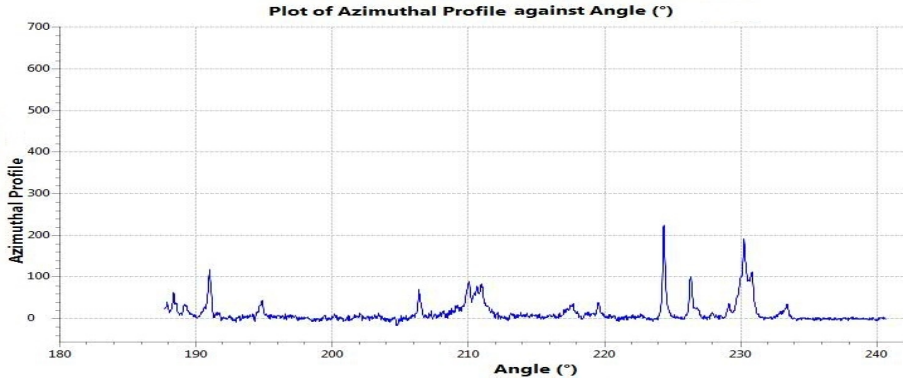

(d)

Figure 5.17: Plots of intensity vs azimuthal angle for Debye ring sections corresponding to a LN crystal plane $< 214 >$, for each XRD pattern presented in Figure 5.16

5.5 Conclusions

To conclude, we presented results that correspond to findings that occurred during the core investigation of this thesis.

Results on the annealing of a-Si gratings proved to be an interesting and useful option for uniformly erasing a-Si gratings in silicon photonic circuits. The experiment of transmission loss indicate that after laser annealing the devices maintains its functionality as compared to the same device before annealing. This technique could potentially be extended to remove other a-Si components in reconfigurable optical circuits in Si.

It was demonstrated that optical waveguides are formed underneath the laser annealed tracks in a-Si. The formation of these waveguides could be explained by the change of refractive index in LN produced by lithium diffusion caused by the heat produced by the light absorption of the a-Si layer. The mode profiles of the LN waveguides were shown be multi mode or single mode in the visible range $\lambda = 633nm$ and the IR $\lambda = 1523nm$ spectral region. The transmission loss of these waveguides were measured using the technique of cut back showing a loss as low as $4.54dB/cm$.

Finally we presented preliminary results on the crystallization of a-LN on a c-Si substrate indicating that laser processing produces crystals of LN. Extending this work could be a suitable option to produce hybrid devices by placing locally crystallised LN on Si photonic components already fabricated instead of growing the LN crystal individually and then using complex methods to bond it to the substrate of interest.

All of results presented in this chapter could potentially open future research directions.

References

[1] M. L. Dakss, L. Kuhn, P. F. Heidrich, and B. A. Scott, "Grating coupler for efficient excitation of optical guided waves in thin films," *Applied Physics Letters*, vol. 16, pp. 523–525, 1970.

[2] R. Loiacono, G. T. Reed, G. Z. Mashanovich, R. Gwilliam, S. J. Henley, Y. Hu, R. Feldesh, and R. Jones, "Laser erasable implanted gratings for

integrated silicon photonics.," *Optics express*, vol. 19, pp. 10728–34, May 2011.

[3] R. Topley, L. O'Faolain, D. J. Thomson, F. Y. Gardes, G. Z. Mashanovich, and G. T. Reed1, "Planar surface implanted diffractive grating couplers in SOI ," *Optics Express*, vol. 22, pp. 1076–1084, 2014.

[4] M. J. Heck, J. F.Bauters, L.Devenport, and J. E. Bowers, "Lithium niobate: Summary of physical properties and crystal structure," *Appl. Phys. A, Solids Surf*, vol. 37, pp. 191–203, 1985.

[5] K. Peithmann, M.-R. Zamani-Meymian, M. Haaks, K. Maier, B. Andreas, K. Buse, and H. Modrow, "Fabrication of embedded waveguides in lithium-niobate crystals by radiation damage," *Applied Physics B*, vol. 82, no. 3, pp. 419–422, 2006.

[6] C. Becker, A. Greiner, T. Oesselke, A. Pape, W. Sohler, and H. Suche, "Integrated optical ti:er:linbo3 distributed bragg reflector laser with a fixed photorefractive grating," *Opt. Lett.*, vol. 23, pp. 1194–1196, Aug 1998.

[7] R. C. Alferness, R. V. Schmidt, and E. H. Turner, "Characteristics of ti-diffused lithium niobate optical directional couplers," *Appl. Opt.*, vol. 18, pp. 4012–4016, Dec 1979.

[8] W. E. Martin, "A new waveguide switch/modulator for integrated optics," *Applied Physics Letters*, vol. 26, no. 10, pp. 562–564, 1975.

[9] W. Burns, A. Lee, and A. Milton, "Active branching waveguide modulator," *Applied Physics Letters*, vol. 29, no. 12, pp. 790–792, 1976.

[10] V. Ramaswamy, M. Divino, and R. Standley, "Balanced bridge modulator switch using ti-diffused linbo3 strip waveguides," *Applied Physics Letters*, vol. 32, no. 10, pp. 644–646, 1978.

[11] J. L. Jackel, C. Rice, and J. Veselka, "Proton exchange for high-index waveguides in linbo3," *Applied Physics Letters*, vol. 41, no. 7, pp. 607–608, 1982.

[12] A. Muir, G. Daniell, C. Please, I. Wellington, S. Mailis, and R. Eason, "Modelling the formation of optical waveguides produced in linbo 3 by laser induced thermal diffusion of lithium ions," *Applied Physics A: Materials Science & Processing*, vol. 83, no. 3, p. 389 396, 2006.

[13] S. Mailis, C. Riziotis, I. T. Wellington, P. S. C. Gawith, and R. W. Eason, "Direct ultraviolet writing of channel waveguides in congruent lithium niobate single crystals," *Opt.Lett*, vol. 28, pp. 1433–1435, Apr. 2003.

[14] R. Schmidt and I. Kaminow, "Metal-diffused optical waveguides in linbo3," *Applied Physics Letters*, vol. 25, no. 8, pp. 458–460, 1974.

[15] D. Kip, "Photorefractive waveguides in oxide crystals: fabrication, properties, and applications," *Applied Physics B: Lasers and Optics*, vol. 67, no. 2, pp. 131–150, 1998.

[16] E. L. Wooten, K. M. Kissa, A. Yi-Yan, E. J. Murphy, D. A. Lafaw, P. F. Hallemeier, D. Maack, D. V. Attanasio, D. J. Fritz, G. J. McBrien, *et al.*, "A review of lithium niobate modulators for fiber-optic communications systems," *IEEE Journal of selected topics in Quantum Electronics*, vol. 6, no. 1, pp. 69–82, 2000.

[17] M. L. Bortz and M. M. Fejer, "Annealed proton-exchanged linbo3 waveguides," *Opt. Lett.*, vol. 16, pp. 1844–1846, Dec 1991.

[18] V. Joshkin, K. Dovidenko, S. Oktyabrsky, D. Saulys, T. Kuech, and L. McCaughan, "New methods for fabricating patterned lithium niobate for photonic applications," *Journal of Crystal Growth*, vol. 259, no. 3, pp. 273 – 278, 2003.

Chapter 6

Conclusions and outlook

6.1 Conclusions

In this final chapter the conclusions from the work that was presented in this thesis as well as possible future direction will be presented.

An introduction of materials and methods followed in the work that is contained in this thesis was presented in the first introductory chapter. The properties of the materials used as their relevance to the work was discussed. A short introduction to Si as photonic material was given as motivation for the development of novel production methods for the production of silicon devices with different substrates, with less proceedings, in a faster fashion and cheaper than the technology used until today.

The methods to incorporate a-Si in the different substrates were explained. PECVD and HWCVD were explained and the difference between them was identified. The analytical methods used for this work, Raman spectroscopy and X-ray diffraction were reviewed and settle in this chapter. Finally a review of the functionality fabrication methods for optical waveguides were presented.

In the second chapter we have demonstrated laser crystallization of a-Si in two different substrates Silica Glass and Silica on Silicon using visible wavelengths. The writing set up was used for the production of curved structures finding a smooth displacement and a fast implementation of any shape, as ring resonators, y junctions or delay lines. A range of irradiation conditions

for laser powers and scanning speeds were investigated. The results of laser irradiation were analysed to identify the presence of crystalline Si using Raman spectroscopy and X-Ray diffraction.

Raman studies confirmed laser induced crystallization. The analytical method to address the best crystallization conditions used was explained in the chapter. By comparing the Lorentzian FWHM of the fitted Voigt function from a Si crystal wafer with the value of $2.7 \pm 2cm^{-1}$ [1] to each one of the different irradiation conditions. It was found, for the case of a-Si/G that the closer value of the FWHM to the c-Si is of $3.02cm^{-1}$ with a peak shift of $2.26cm^{-1}$ to the right due its polycrystalline composition[2]. The conditions of power and intensity for this case were $90mW$ or $2.54W/cm^{-2}$. In the other sample configuration, a-Si/Sc-Si, the best FWHM was of $3.04cm^{-1}$ for the conditions of $120mW$ or $3.39MW/cm^2$ with $7mm/min$. These samples where investigated using X-ray diffraction. The X-ray diffraction patterns were obtained using the micro-focus XRD beam line at the Diamond Light Source synchrotron located at the Harwell Science and Innovation Campus, Oxfordshire.

XRD measurements revealed the formation of crystals along and across the tracks confirmed the crystallisation finding crystals as large as $36\mu m$ long. From the XRD results it can also be concluded that the crystallized a-Si is strained as indicated by a shift between the reference diffraction positon and the actual diffraction position.

In chapter 3 we have demonstrated laser crystallization of a-Si films on LN substrates comparing two different deposition methods, PECVD and HWCVD. We found a similar behaviour between the two substrates with the exception on formation of periodically pearl structures (in the case of lower powers) for the PECVD sample. It was found that these pearls have a decreasing periodicity as the speed increases. The characterization showed of lower crystallisation that the best power to form continuous crystallized tracks was $40mW$ or $1.13MW/cm^2$ in both depositions methods. This was expected since the substrate and the deposited a-Si thickness were identical. Raman studies confirmed the best crystallization is again at $7mm/min$ as it was shown for a-Si/SG and a-Si/Sc-Si. Best result according to the FWHM of the Raman spectra are found for HWCVD, proving that this deposition method is the best of the two for the waveguide purpose.

In chapter 4, a differential etching method was used to remove the a-Si from laser crystallized samples to form poly-Si ridges. Samples were treated with Secco etching obtaining a etch rate of $100nm/min$. Poly-Si ridges were produced after Secco etching on a variety of substrates. Raman analysis indicated that after Secco etching all the FWHM widths improved, since the contribution of the peripheral nano crystals was removed. The best Raman width was found $2.90cm^1$ corresponding to the optimum conditions for crystallization identified in chapter 3 ($90mW$ / $2.54W/cm^{-2}$ at $7mm/min$). XRD measurements were performed again for a-Si/SG after Secco etching , revealing now larger crystals along the ridges with lengths as long as $35\mu m$. These samples were used as ridge waveguides. The transmission loss of the ridges was measured (for silicon ridges on silica glass). The results shown had an attenuation around $9.3dB/cm$ which is a very encouraging first result for this none optimized method.

We proved that this method is suitable for the fabrication of optical circuits in different substrates, finding a similar etching results with all the substrates tried. The best results at a glance are the ridges formed at a-Si/Sc-Si. These samples where fabricated at the end of this work so there are no available loss measurements, however as this technique has been proven for a-Si/SG, similar results are expected for silica on silicon substrates too.

The fifth chapter contains intermediate results found in the course of the main investigation and they result to the impact of laser irradiation to a-Si on crystalline Si substrates, the formation of waveguide in LN is a by product of a-Si crystallisation and finally crystallization of a-LN on c-Si substrates.

Results of the annealing of a-Si gratings prove to be a viable option to fabricate rewritable optical circuits, since the results found after the experiments of loss transmission through a bow grating device, showed that the transmission through the annealed region is restored after erasing the a-Si grating.

Embedded LN waveguides were fabricated with the potential to transmit multi mode and single mode light in the visible range $\lambda = 633nm$ as well for the IR $\lambda = 1523nm$. A possible explanation on the formation of this waveguides is as follows: the a-Si film absorbs the radiation from the laser source during the annealing transferring the heat to the LN substrate, this fast change of temperature induces diffusion of lithium, changing the index of refraction

underneath the irradiated track. These results confirm a new method for the fabrication of embedded waveguides of LN.

The last experiment was the laser-crystallisation of a layer of amorphous LN deposited on c-Si, using the absorption of silicon during the laser irradiation heat is transferred to the a-LN film forming LN crystals. XRD and Raman studies were performed on the irradiated tracks confirming that crystallisation has taken place. However more experiments are needed to optimize the crystallisation process.

Laser processing of amorphous silicon is a processing method for the fabrication of photonic poly-Si structure. Secco etching process used to preferentially etch was a-Si for the production of poly-Si ridges. A table summarizing all the best conditions for the best crystallization in the different substrates is presented in Table 6.1. This table could be used as starting point to characterize new composite materials with films of a-Si.

Table 6.1: Table of best crystallization conditions for all the substrates with 400nm a-Si

	20x objective with $\omega_0 \approx 1.5\mu m$			
Sample	Deposition	Speed(mm/min)	Power (mW)	Intensity (MW/cm^2)
$a-Si/G$	HWCVD	7	90	2.54
$a-Si/SOI$	HWCVD	7	110	3.11
$a-Si/LN$	PCVD	7	40	1.13
$a-Si/LN$	HWCVD	7	40	1.13
$a-LN/c-Si$	CVD	1	550	15.56

6.2 Outlook and Future work

Many results achieved during this thesis are still open to improvement and development. Some ideas for future research directions are presented below.

Future work could include continuous development of Si waveguides by laser processing of amorphous silicon on multiple different substrates. Since the deposition methods of a-Si can be achieved at low temperature other substrates could be used to fabricate silicon photonic devices as Lithium Tantalate, Periodically Poled Lithium Niobate (PPLN),Germanium, CMOS circuits,

polymers etc. Other structures as Y junctions, Mach-Zehnder interferometers, intersections, resonators, gratings, cavities, etc., could be fabricated with simplicity and implemented in more complicated optical circuits in the same planar substrate. During this work some of them have been fabricated unfortunately these devices were over etched due to their small size. This made difficult to have an uniform etching of the a-Si around them. This issue could be solved using a two etching process: first Secco etching removing most of the amorphous silicon in the surface and then a second wet etching less aggressive as TAMH to remove the leftovers of a-Si trapped between the small corners of the devices.

An observation system could be implemented in the set up to observe the process live, during the laser irradiation, then the temperature change in the a-Si surface could be calculated and studied.

More conditions like incrementing the speed and the laser intensity could be tried, this to find a faster crystallization process.

Using a different microscope objective with a tighter focusing could be implemented to fabricate smaller Si structures. Also other laser intensity distributions as top hat or doughnut shapes could be implemented since this distributions have show good results in other works [3, 4] or even interferometric exposures to form crystallized patterns in just one exposure.

Computer simulations of the heat transfer, during the laser writing , could be of help to calculate the required intensity to crystallize a-Si in different substrates. Different substrates could be deposited with a-Si and using this method transform it poly-cSi.

An implementation simultaneous heating during the laser irradiation could be use to increase the grain size of the polycrystalline waveguides as it was demonstrated in [5], where the substrate was heated to $500°C$. It was found too that heating the substrate during the annealing reduces stress on the irradiated layer.

In the case of a-Si/LN, different laser writing directions could be tried, since in this research just the y direction of the +Z LN crystal cut was tried, it had been proved that different directions could behave in different manner especially in the case of proton exchange [6]. The optical losses measurements

were not performed on the samples of a-Si/LN due to adhesion problems between a-Si and LN. Two possible solutions to this issue are: 1) placing a thin layer of silicon dioxide before depositing a-Si, in this manner we will have a sample with a similar compound as the samples of a-Si/Sc-Si; 2) avoiding the Secco etching by patterning the devices before laser annealing. A short review of this method was presented in chapter 4: it was found by Raman spectroscopy that pre patterned ridges, made by photolitography techniques, wer laser-crystallized. The combination of LN and Si has great interest since it could be used to have cross coupling light in both the underneath LN waveguide and the polycrystalline Si waveguide on the surface at the same time improving the functionality of this hybrid devices.

Finally the crystallization of a-LN indicates a promising method for the hybridization of LN and Si. More experiments could be required to identify the conditions for the production of oriented ferroelectric LN crystals with minimum damage of the substrate.

References

[1] L. Lagonigro, N. Healy, J. R. Sparks, N. F. Baril, P. J. A. Sazio, J. V. Badding, and A. C. Peacock, "Low loss silicon fibers for photonics applications," *Applied Physics Letters*, vol. 96, no. 4, p. 041105, 2010.

[2] J. Jin, Z. Yuan, L. Huang, S. Chen, W. Shi, Z. Cao, and Q. Lou, "Laser crystallization of amorphous silicon films investigated by raman spectroscopy and atomic force microscopy," *Applied Surface Science*, vol. 256, no. 11, pp. 3453 – 3458, 2010.

[3] S. Kawamura, J. Sakurai, M. Nakano, and M. Takagi, "Recrystallization of si on amorphous substrates by doughnutshaped cw ar laser beam," *Applied Physics Letters*, vol. 40, no. 5, pp. 394–395, 1982.

[4] S. J. Park, Y. M. Ku, E. H. Kim, J. Jang, K. H. Kim, and C. O. Kim, "Selective crystallization of amorphous silicon thin film by a {CW} green laser," *Journal of Non-Crystalline Solids*, vol. 352, no. 920, pp. 993 – 997, 2006. Amorphous and Nanocrystalline Semiconductors - Science and TechnologyProceedings of the 21st International Conference on Amorphous and Nanocrystalline Semiconductors - Science and Technology21st International Conference on Amorphous and Nanocrystalline Semiconductors.

[5] J. Michaud, R.Rogel, T. Mohammed-Brahim, and M. Sarret, "Cw argon laser crystallization of silicon films: Structural properties," *Journal of non-cystalline solids*, vol. 352, pp. 998–1002, apr 2006.

[6] P. Nekvindová, J. Špirková, J. Červená, M. Budnar, A. Razpet, B. Zorko, and P. Pelicon, "Annealed proton exchanged optical waveguides in lithium niobate: differences between the x-and z-cuts," *Optical Materials*, vol. 19, no. 2, pp. 245–253, 2002.

Appendix A

Publications and presentations

A.1 Papers submitted

R.Topley, **G.Martinez-Jimenez**, L.O'Faolain, N.Healy, S.Mailis, D.J.Thomson, F.Y.Gardes, A.C.Peacock, D.N.R.Payne, G.Z.Mashanovich, G.T.Reed. "Locally erasable couplers for optical device testing in silicon on insulator", *Journal of Lightwave Technology* 2014 Vol.32(12) pp.2248-2253.

G.Zisis, **G.Martinez-Jimenez**, Y.Franz, N. Healy, A.C.Peacock, H.M.H. Chong, D.Grech, S.Mailis, "Laser-induced ferroelectric domain engineering in LiNbO3 crystals using an amorphous silicon overlayer", In preparation for submitted to Journal of Optics.

A.2 Papers under preparation

G.Martinez-Jimenez, G.Zisis, Y.Franz, N. Healy, A.C.Peacock, H.M.H. Chong, S.Mailis, "Direct laser writing of poly-crystalline Si ridge waveguides", In preparation for submission to Applied Physics Letters.

A.3 Conference papers

G.Martinez-Jimenez, Yohann Franz, Antoine F. J. Runge, Matteo Ceschia, Noel Healy, SweZin Oo, Tarazona Antulio, Harold M. H. Chong, Anna C. Peacock, Sakellaris Mailis. "Laser writing of polycrystalline Si ridge waveguides", *CLEO: European Conference on Lasers and Electro-Optics.* 2017, Munich, Germany: 26 Jun 2017 CE-P.26 (Poster).

G.Martinez-Jimenez, Zisis G, Franz Y, Healy N, Grech D, Chong HM, Peacock AC, Mailis SM.," A poly-Si on LiNbO3 photonic platform". In: *CLEO: European Conference on Lasers and Electro-Optics and the European Quantum Electronics Conference.* 2015, Munich, Germany: (Oral presentation).

G.Martinez-Jimenez, G.Zisis, Y.Franz, N.Healy, A.C.Peacock, H.Chong, D.Grech, S.Mailis. "Laser crystallization of silicon on lithium niobate", *Conference on Lasers and Electro-Optics (CLEO '14)*: San Jose, CA 8-13 Jun 2014 JTh2A (Poster).

S.Mailis, **G.Martinez-Jimenez**, G.Zisis, Y.Franz, N.Healy, A.C.Peacock. "Annealing of amorphous silicon using c.w. visible lasers", *E-MRS '14 Materials Research Society Spring Meeting* Lille 26-30 May 2014 (Invited).

R.P.Topley, **G.Martinez-Jimenez**, L.O'Faolain, N.Healy, S.Mailis, D.J.Thomson, F.Y.Gardes, A.C.Peacock, D.N.R.Payne, G.Z.Mashanovich, G.T.Reed. "Temporary grating coupler structures using localised refractive index engineering", *Asia Communications and Photonics Conference* Shanghai 11-14 Nov 2014 AW3B.2 .

S.Mailis, N.Healy, **G.Martinez Jimenez**, G.Zisis, Y.Franz, D.Grech, H.Chong, A.C.Peacock, "A silicon/lithium niobate hybrid photonic material platform produced by laser processing", *European Congress and Exhibition on Advanced Materials and Processes (Euromat 2015)* Warsaw 20 - 24 Sep 2015 Keynote (Invited).

R.P.Topley, **G.Martinez-Jimenez**, L.O'Faolain, N.Healy, S.Mailis, D.J.Thomson, F.Y.Gardes, A.C.Peacock, D.N.R.Payne, G.Z.Mashanovich, G.T.Reed. "Erasable diffractive grating couplers in silicon on insulator for

wafer scale testing", *SPIE Photonics West San Francisco* 1-6 Feb 2014 8990-7 .

S.Mailis, **G.Martinez Jimenez**, G.Zisis, Y.Franz, N.Healy, D.Grech, H.M.H.Chong, A.C.Peacock, "Laser processing of amorphous silicon on lithium niobate for photonic applications", *FNM 2016: International Workshop on Functional and Nanostructured Materials* Tbilisi, Georgia 6 Sep 2016 (Invited).